Conceptual Design of a Flameless Combustor for Aircraft Engines

M. el Abbassi

Thesis Report


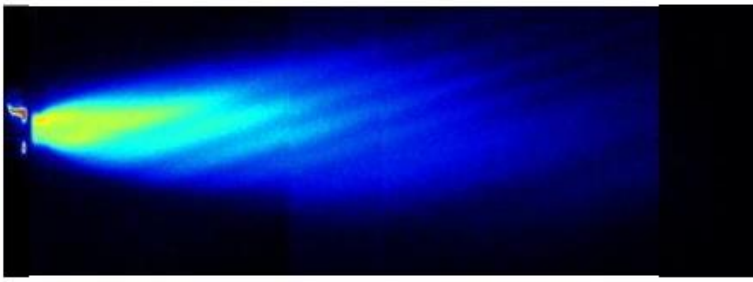

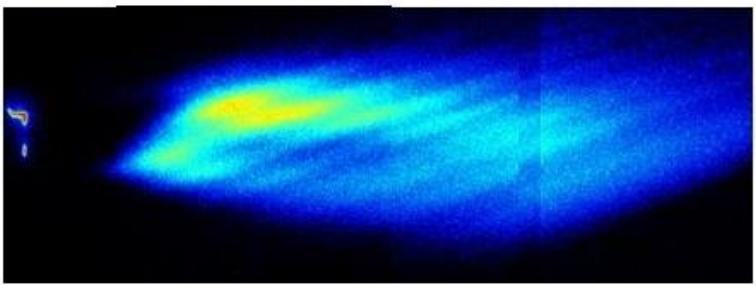

TU Delft Delft University of Technology

Challenge the future

Conceptual Design of a Flameless Combustor for Aircraft Engines

Thesis report

By

M. el Abbassi

in partial fulfilment of the requirements for the degree of

Master of Science
in Aerospace Engineering

at the Delft University of Technology,
to be defended publicly on Wednesday September 30th , 2015 at 10:00

Supervisor:	Dr. A. Gangoli Rao	TU Delft
Thesis committee:	Prof. Dr. D.J.E.M. Roekaerts	TU Delft
	Dr. D. Lahaye	TU Delft
	A.A.V. Perpignan, MSc.	TU Delft

An electronic version of this thesis is available at http://repository.tudelft.nl/.

Thesis Registration Number: 050#15#MT#FPP

TU Delft Delft University of Technology

Acknowledgements

This thesis report is written as a part of the MSc. program in Flight Performance and Propulsion at the Faculty of Aerospace Engineering of Delft University of Technology. It forms the final step in completing this study and I'm happy that I have been able to contribute in the knowledge pool of the department Propulsion and Power.

First of all, I would like to express my gratitude towards my supervisor, dr. Arvind Gangoli Rao, for his support and guidance during the project, from beginning to end. I would like to thank ir. Jan Vriend and dr. Dipanjay Dewanji for their guidance during the initial stage of the thesis and for helping me set my objectives. A special thanks goes to dr. Abhishek Bhat for his feedback during the meetings which helped me to look more critically towards my work. I would like to extend a special thanks to MSc. André Perpignan for reading through this report and providing me with valuable comments. I would also like to thank prof. dr. Dirk Roekaerts for sharing with me his knowledge about combustion, and dr. Domenico Lahaye for completing my graduation committee.

Most importantly, I would like to thank my parents for having raised me and for their unconditional love. Finally, I would like to address a special person, my friend Asma, for her continuing support, involvement and encouragements.

Delft, September 2015 M. el Abbassi

Abstract

The thesis presents a feasibility study of a proposed combustion methodology by means of two-dimensional Computational Fluid Dynamics on the application of Flameless Combustion to an aircraft engine with the objective to achieve ultra-low pollutant emissions. The geometrical design started from scratch while taking the philosophy of the proposed methodology into account, which was to allow the primary air to be directly injected at the centre of the combustor dome and the fuel to be entrained by the recirculated combustion products.

The combustor's entry conditions and global size were estimated based on a conventional turbofan engine and corrected at atmospheric pressure. The most important parameter to achieve flameless combustion was considered to be the recirculation ratio in order for it to be sustained. Therefore a cold flow simulation was carried out first with the objective to fulfil this requirement by using RANS-based turbulence models. The models were first validated by attempting to reproduce the measured flow velocities of three wind tunnel cases with similar geometry. All models under predicted maximum recirculation for the largest part by 20% - 30%, with the k-epsilon Realizable model being closest to determine maximum recirculation. This model also showed a similar linear trend in maximum recirculation ratio with respect to different channel-to-inlet area ratios, which was of high interest. Also the reattachment point was well predicted and aided in the prediction of the flow paths. Attempts were also made to reproduce the measured velocity profiles with the Large Eddy Simulation derived models. The Embedded Large Eddy Simulation model did not give better results, probably due to the mesh resolution still being too coarse and the Detached Eddy Simulation model even performed worse which made it not suitable for such flow cases.

The recirculation ratio was independent on inlet injection velocity and largely dependent on the channel-to-inlet area ratio which is limited in an aero engine. Adding a cavity to the channel increased the maximum recirculation ratio with nearly 30% and the cavity shape had little effect on its value. Within the engine's size limits the annular type combustor could achieve a maximum recirculation ratio up to a value of 1.3 in the cold flow and with a can type combustor the values where between 2 and 3. In the literature a value of at least 3 was required. With the aim of having the lowest pressure drop, the initial concept was designed with both cavity steps inclined at 50^{o} with filleted corners. This reduced the pressure drop to 1.8%.

The simulations of the reacting flow were first applied to the can combustor and were carried out with the Eddy Dissipation Concept model, using a detailed reaction mechanism. Combustion reduced the cold flow's recirculation ratio by a factor 2. By studying the results and understanding the reacting flow the combustion could be controlled by qualitative refinement of the combustors geometry and repositioning of the inlets of the fuel and secondary air. With the help of using vitiated air as oxidant, these rough alterations led to CO emissions to reduce to less than 50 ppm and NO_X to less than 2 ppm, both for cruise and take-off conditions. Also the effect of inlet parameters on the emissions such as temperature, and fuel-to-air equivalence ratio was investigated which showed familiar results.

The more realistic annular combustor did not perform as good when using the final geometry of the can combustor, which led to an increase of CO emissions by an order of

magnitude. Due to the area ratio of the annular combustor being roughly six times smaller than that of the can combustor, the velocity of the recirculated flow increased from 24 m/s to nearly 140 m/s, which led to high heat dissipation and a residence time five times as short. Further geometry improvement was more difficult making the emissions harder to control. However CO emissions were eventually reduced to below 200 ppm and NO_X below 65 ppm.

The annular combustor was also tested to simulate actual flight conditions by also pressurising the inlet air. This led to an improved reaction rate and the CO emissions were further reduced to below 100 ppm. The NO_X emissions reduced to below 20 ppm and the pressure loss was less than 3% which was below the imposed requirement of an aero engine combustor.

Nomenclature

Abbreviations

ATC	Annular type combustor	[-]
CTC	Can (or Cannular) type combustor	[-]
DES	Detached Eddy Simulation	[-]
EGR	Exhaust Gas Recirculation	[-]
ELES	Embedded Large Eddy Simulation	[-]
FC	Flameless combustion	[-]
GTE	Gas turbine engine	[-]
HPC	High pressure Compressor	[-]
pdf	Probability density function	[-]
RSM	Reynolds Stress Model	[-]
TIT	Turbine Inlet Temperature. Overall gas temperature leaving the combustor.	[K]
VM	Vortex Method	[-]

Latin characters

A	Cross-sectional area of the liner	[m^2]
a	Cross-sectional area of the air inlet	[m^2]
c_p	Specific heat capacity at constant pressure	[$Jkg^{-1}K^{-1}$]
Da	Damköhler number	[-]
E	Total energy	[J]
f	Mixture fraction	[-]
g	Variance of mixture fraction fluctuation	[-]
$\vec{g}$	Gravitational acceleration	[m s^{-2}]
H	Overall combustor radial dimension (‘liner height’)	[m]
h	Enthalpy	[J]
i	Combustor air inlet radial dimension (‘inlet height’)	[m]

J	Diffusion flux	[kg $m^{-2}s^{-1}$]
K_V	Recirculation Ratio	-
k	Turbulence kinetic energy	[$m^2 s^{-2}$]
k_{eff}	Effective thermal conductivity	[W $m^{-1}K^{-1}$]
L	Combustor cavity longitudinal dimension ('cavity length')	[m]
l	Combustor cavity longitudinal dimension ('liner length')	[m]
M_w	Molecular weight	[kg $kmol^{-1}$]
$\dot{m}$	Mass flow rate	[kg s^{-1}]
$p(..)$	Probability	[-]
R	Cavity corner radius	[m]
R_i	Chemical reaction rate of a specie	[kg s^{-1}]
T_{HG}	Hot Gas Temperature. Temperature of the combusting gas excluding the secondary flow.	[K]
t	Time	[s]
t_c	Characteristic chemical reaction time	[s]
t_t	Characteristic flow time	[s]
u	Velocity magnitude	[m s^{-1}]
U_i	Inlet velociy	[m s^{-1}]
X	Longitudinal distance from the combustor inlet	[m]
Y^+	Non-dimensional wall distance	-
Y_i	Mass fraction of a chemical specie	[-]
Z	Local mass fraction of a specific element	[-]

Greek characters

$\alpha 1$	Cavity's leading step angle	[^{o}]
$\alpha 2$	Cavity's trailing step angle	[^{o}]
χ	Scalar dissipation rate	[s^{-1}]

ε	Turbulence dissipation rate	[m^2 s^{-3}]
φ	Fuel to air Equivalence Ratio	[-]
ϕ	Scalar quantity	[-]
γ	Fine scale length fraction	[-]
μ	Dynamic viscosity	[kg $m^{-1}s^{-1}$]
ν	Stoichiometric coefficient	[-]
ρ	Density	[kg m^{-3}]
σ_R	Reaction zone thickness in mixture fraction space	[-]
τ	Stress tensor	[N m^{-2}]

Subscripts

fuel	Fuel property or inlet condition of the fuel
HG	Hot Gas
i	Inlet
OX	Oxidant
rec	Recirculated
st	Stoichiometric

Contents

1

Introduction

As environmental and health concerns due to air pollution are growing every day, future generation aircraft engines are required to be more efficient, produce less noise and drastically reduce pollutant emissions. Flameless Combustion (FC) was first developed to suppress thermal NO_X formation in industrial furnaces using preheated combustion air. This technique showed to have large potential for Gas Turbine Engines (GTE) and developments have occurred in the last decade to make FC also possible in aero engines.

Since FC has never been applied in an actual aero engine before, research is necessary in order to design a combustor that is attractive for aero engine manufacturers. During this MSc. thesis the possibilities were explored and an attempt was made to design a combustion chamber that could generate appropriate conditions for FC to take place, with the focus lying on the application on aero engines (It will be noticed that the words GTE and aero engines will often mix in this report. While 'GTE' applies in general sense, including e.g. industrial GTEs and aircraft engines, when talking about 'aero engines' only aircraft engines are considered). The design will be preliminary and focused on investigating the flow-chemistry interaction of FC by means of Computation Fluid Dynamics (CFD) in order to gain more fundamental knowledge and establish a road map for further research.

A small introduction will be given in this chapter about gas turbine combustion followed by more detailed background information about the FC technology and will end with the research objective of this thesis.

In chapter 2 the theory of CFD modelling will be highlighted with a discussion about some of the available turbulence and combustion models. With this knowledge, the first attempt in designing the concept using non-reacting flow will come to light in chapter 3 with the validation of the turbulence model. Chapter 4 will discuss the results of the reacting flow simulations and also further modifications of the geometry which led to the final preliminary concept. The conclusions and recommendations are found in chapters 5 and 6, respectively.

1.1 Research Background

This section contains a review of the background knowledge used in order to better understand the topic and to formulate a suitable research objective. Some important combustion terms and combustor basics shall be defined and discussed. Also the basic

concepts of turbulent flames will be presented and finally FC will be described along with its application on aero engine combustors.

1.1.1 Combustion terminology

1.1.1.1 Stoichiometric reaction

Stoichiometric reaction is a unique reaction in which the exact amount oxygen is provided to the fuel to fully oxidise. If it is assumed that air consists of 21% oxygen and 79% nitrogen, the equation for a stoichiometric reaction of an air-methane mixture on a mole basis is

$$CH_4 + 2(O_2 + 3.76N_2) \rightarrow CO_2 + 2H_2O + 7.52N_2 \quad (1.1)$$

1.1.1.2 Equivalence ratio

One of the most important parameters used to characterize combustion is the equivalence ratio which is the fuel-to-air ratio normalized by the stoichiometric fuel-to-air ratio

$$\phi = \frac{(fuel/air)_{actual}}{(fuel/air)_{stoich}} \quad (1.2)$$

So that ϕ=1 is defined as stoichiometric combustion. If ϕ <1, there is an excess of air and the combustion is called lean and if ϕ >1 it is considered (fuel-)rich.

1.1.1.3 Adiabatic Flame temperature

Another important combustion parameter is the flame temperature. The flame temperature is determined by the energy balance between the reactants and the products at equilibrium. Theoretically, the highest flame temperatures would be produced at ϕ = 1, because all of the fuel and oxygen would be consumed. In practice however, the effects of species dissociation and heat capacity shift the peak temperature to slightly above stoichiometric (ϕ ≈1.05). If the combustion process takes place adiabatically and no work is done, nor does the kinetic or potential energy change, then the flame temperature is referred to as the adiabatic flame temperature.

1.1.2 Generic GTE combustor design basics

The combustor of a GTE is placed between the compressor and turbine. Its purpose is to add energy to the working gas flow in the form of heat by means of chemical reactions. Since the beginning of the usage of gas turbines in aircraft, the overall engine efficiency has increased from 15% to about 50% nowadays. The primary reason for that is the increased bypass ratio as the fan became larger and the core smaller, but also due to the increase in compression ratio and Turbine Inlet Temperature (TIT). The TIT is the temperature of the flow that leaves the combustor and is the most critical parameter of the engine due to the limitations of the turbine blade material that is continuously subjected to the hot gas flow. Since the flame temperature is much higher (more than 2000 K) than the turbine can handle, large amount

of excess air is provided in the combustion flow to cool the combustion gases. Normally the stoichiometric fuel-to-air ratio is about 1:15 (depending on the fuel), but in GTEs a typical overall fuel-to-air ratio is at least 1:40 ($\varphi < 0.4$).

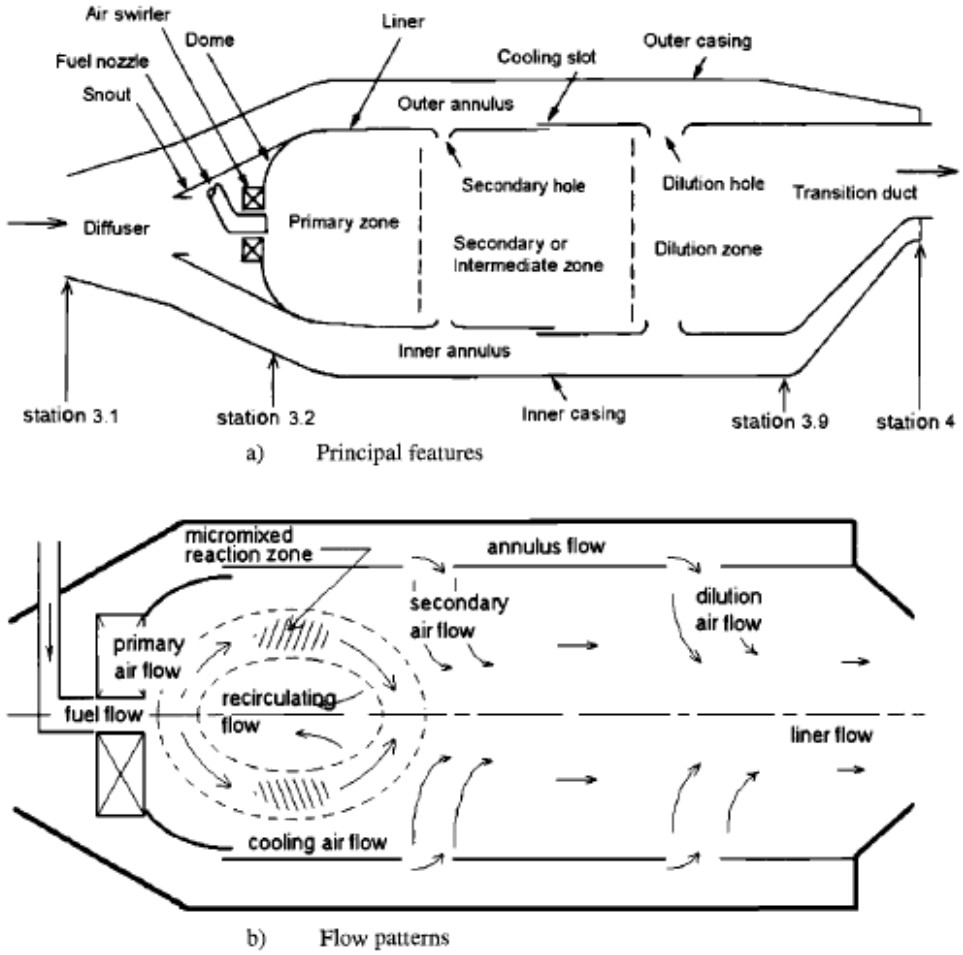

Figure 1.1 Main features(a) and flow patterns(b) of a generic GTE combustor [1].

Figure 1.1 shows a schematic of a traditional combustor and its flow patterns. Compressed air leaves the compressor at high velocity (above 100 m/s), which is lowered by the diffuser to some extent but still not enough to keep the flame stable if injected directly in the combustor dome. The air is first split in two parts. A minor part enters the combustor liner at the beginning through air swirlers and mixes with the atomized fuel prior to ignition. The swirling flow creates a recirculation zone with hot combustion products, to which at some point the flow almost stagnates and the conditions for a stable flame is met so that the flame will 'anchor' itself to that point. The remaining and major part of the air stream goes around the dome in the annulus and enters the dome later on through the liner both for further oxidation and cooling purposes, so that the TIT does not exceed the turbine limit. The liner casing surrounds the entire combustor.

The combustor also comes in different shapes. The can-type is characterized by the rotor being surrounded by multiple self-contained cylindrical 'cans', all having their own casing,

annulus, liner and fuel injectors. The second type is the can-annular (or 'cannular') combustor where all cylindrical liners share one common annulus and are contained inside a large continuous and ring(or annular) shaped casing around the rotor. The last type is the annular combustor where both the liner and casing are ring-shaped with no individual parts left except for the multiple fuel injectors. Due to the removal of the separate combustion zones, the annular combustor is most commonly used in aero engines because of its lighter structural weight, more compact size and more uniform outlet temperature. The different combustor types are shown in figure 1.2.

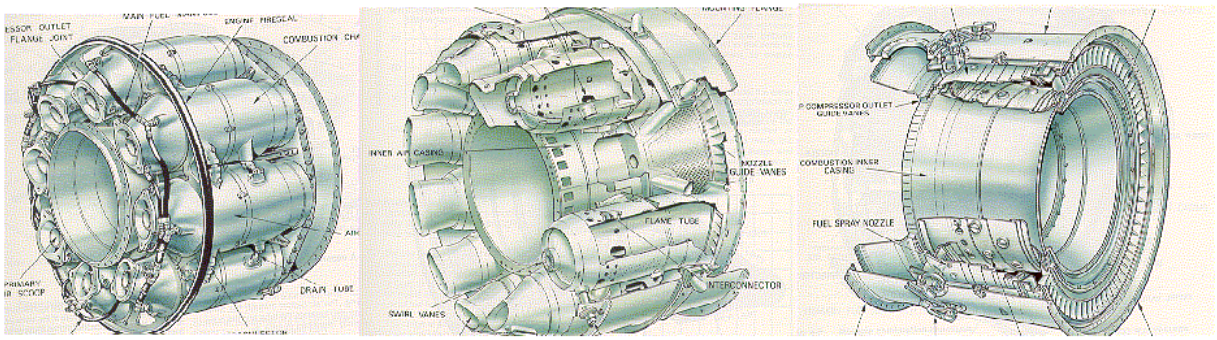

Figure 1.2 Three different types of combustors: (from left to right) can, can-annular and annular[2].

1.1.3 Turbulent diffusion flame characteristics

Most aero engine combustors can be classified as diffusion flame (or non-premixed) combustors. Although in some engines different variants of lean-premixed combustion are applied, the phenomenology of this combustion type is out of the scope of the thesis. In a diffusion flame the air and fuel enter the combustion domain separately and the reaction takes place in a very thin region called the reaction zone, where the oxidant and fuel meet at near-stoichiometric conditions (see figure 1.3). The sharp and high temperature increase in the flame front give the flame its colour. Diffusion flames in GTE combustors are always turbulent, which is beneficial because:

- it allows for better mixing between the reactants
- it causes the flame front to wrinkle, making the reaction zone more compact which requires less volume for combustion as compared to a laminar flame.

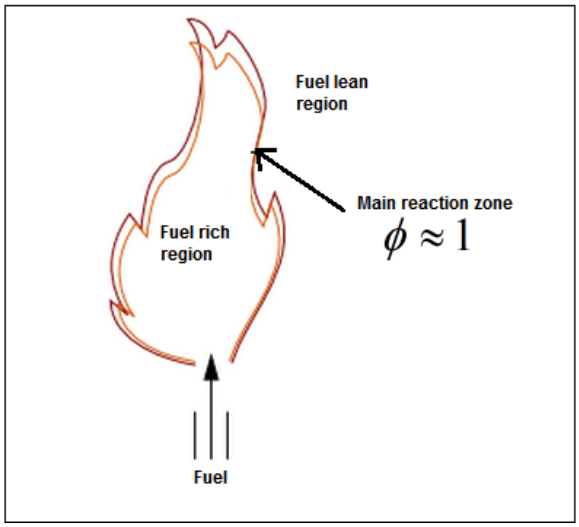

Figure 1.3 Example of a diffusion flame, where fuel is injected into the atmosphere.

One of the parameters used to classify turbulent flames is the Damköhler number (Da) which is the ratio between the fuel/air mixing time and the chemical reaction time. Specifically, Da is defined as the ratio between the characteristic flow time t_t and characteristic chemical reaction time t_c. The Da can be used to distinguish FC from the other combustion regimes (as will be explained in section 1.1.5).

$$Da = \frac{\tau_t}{\tau_c} \tag{1.3}$$

In turbulent flow, t_t can be represented by the Kolmogorov time scale t_K , which is the time scale of the smallest possible turbulent 'eddy', on which the turbulent kinetic energy dissipates into fluid internal energy and the kinematic viscosity effects are large [3]. Higher turbulent mixing rates lead to smaller Kolmogorov eddies, hence smaller turbulent time scales. When $t_c > t_K$, the smallest eddies will spread the reaction zone, resulting in a distributed reaction zone. If $t_c < t_K$, then the smallest eddy will not be able to spread the reaction zone, and we have a flamelet regime.
Chemical reaction rates in a typical diffusion flame are fast with respect to fluid mixing rates and Da is much greater than one. When Da << 1, the distributed reaction zone resembles a Well-Stirred Reactor, which is an idealized reactor where the reactants and combustion products are perfectly mixed and therefore no temperature or species gradients remain in the reaction zone, which is assumed to have a finite volume.

Figure 1.4 shows a schematic diagram of the non-premixed flame regimes in terms of the Damköhler number and the normalised mixture fraction fluctuation in the reaction zone (vertical axis). The mixture fraction, an important scalar quantity in combustion modelling, is defined as the local elemental mass fraction originating from the fuel inlet. This is further discussed in section 2.3.2.1. Its fluctuation increases with increasing turbulence.
As explained by Roekaerts et. al [4], $\sqrt{g_{st}}$ is the standard deviation of the stoichiometric mixture fraction fluctuations inside the reaction zone. If $\sqrt{g_{st}}$ is larger than the reaction zone thickness (in mixture fraction space), $\sigma_{R,}$ than local extinctions take place and the connected reaction zone is separated into so called flamelets. $\tilde{\chi}_{st}$ is a measure of heat

dissipation of the reaction zone and if it exceeds the critical heat dissipation χ_q , no reaction takes place. χ_q increases with Da because less radicals get dispersed by the turbulent flow from the reaction zone (also called radical pool). The regime of distributed reaction zones, where also FC lies, does not suffer from heat dissipation and is therefore the most stable form of diffusion combustion.

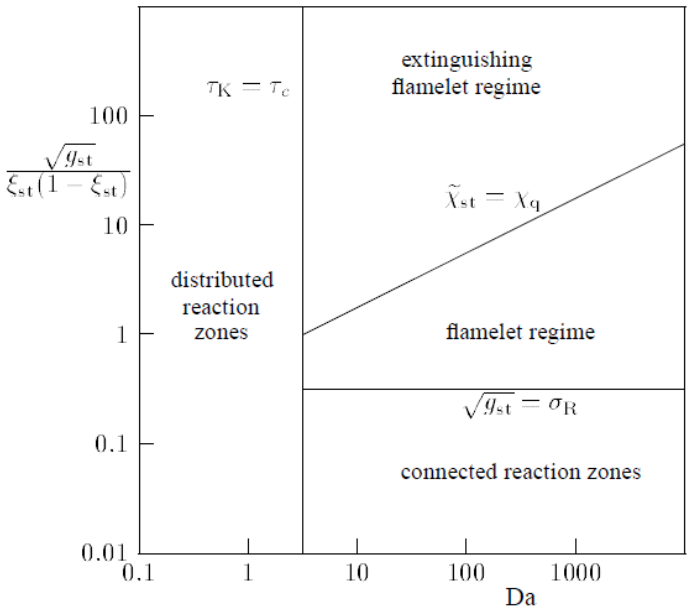

Figure 1.4 A schematic diagram of the non-premixed flame regimes in terms of the Damköhler number and the normalised mixture fraction fluctuation in the reaction zone [4].

1.1.4 Pollutant Emissions by Aero Engines

Much effort has been put in reducing aero engine emissions in the last four decades by improving both the engines cycle efficiency and combustor design. From all emissions NO_X has proven to be most difficult to suppress, mainly due to the opposite effect in its formation by the increasing combustor temperature as compared to the other products. Table 2.1 shows the four major pollutants being emitted by a conventional aircraft. It is noteworthy that the amount of NO_X emissions greatly exceeds that of the other pollutants (nearly 86% in total flight). Most of the NO_X is emitted during the cruise phase at the lower border of the stratosphere, making aircrafts the only anthropogenic pollutant source at that height and partially (though very little) play part in the breakdown of the protective ozone layer in the stratosphere.

Table 1.1 Emission percentages per flight phase of a medium haul liner traveling 500 nm [5].

constituent	takeoff and landing	climb, cruise, and descent	total flight
CO	5.4	7.0	12.4
NO_x	20.6	65.3	85.9
UHC	0.6	1.0	1.6
soot	-	0.1	0.1
total	26.6% (77.4% NO_x)	73.4% (89.0% NO_x)	100.0% (85.9% NO_x)

1.1.4.1 *CO, UHC and NO_X formation*

This section will briefly present some of the important pollutants formation and reaction mechanisms.

Carbon monoxide is formed during the breakdown of the hydrocarbon fuel when the fuel molecules are attacked by the O and OH radicals. In GTEs it arises due to several reasons [6]:

- At very low power conditions where the reaction rate is insufficient for CO to oxidise to CO2 due to low flame temperature. Also, low fuel mass flow leads to poor atomization leading to fuel rich packages.
- At very high temperatures due to dissociation of CO_2. Providing excess air at the secondary zone usually enables CO to oxidise back to CO_2.
- By inadequate mixing of fuel and oxygen, which aggravates with increasing φ, yielding both reaction-poor and excess-fuel regions.
- When further reactions to complete oxidation are killed (quenching). This happens in regions that are cooled excessively by the cooling flow. Especially when CO is entrained by the cooling jets near the combustor wall.

The oxidation of CO may occur in two ways:

$$CO + O_2 \rightarrow CO_2 + O \quad (1.4)$$

$$CO + OH \rightarrow CO_2 + H \quad (1.5)$$

of which reaction (1.4) is very slow. The oxidation mainly happens via reaction (1.5) on the condition that H_2O or H_2 are present to form the OH radical.

UHC is a gas consisting of unreacted fuel and its dissociated sub species with lower molecular weight due to incomplete combustion (C_XH_Y). The factors influencing UHC formation is the same as for CO. Primarily due to poor atomization, quenching and low reaction rates.

NO and NO_2 are formed either at high temperatures where N_2 reacts with different radicals, or as a combustion product of nitrogen-bound fuel. NO is far more important than NO_2 in combustion processes because NO_2 quickly reacts with O or H radicals to form NO, unless this reaction is frozen by the cooling flow. NO in aero engines is produced by the following

three different mechanisms: thermal NO (or Zeldovich mechanism), NO via the N_2O intermediate, and prompt NO.

Thermal NO is normally the dominant NO_X route and forms when N_2, O_2 and H_2O dissociate and react. This is a relatively slow reaction and requires high combustion temperatures for it to occur. Thus the formation is largely controlled by flame temperature (exponentially) and it increases with increasing residence time. At combustion temperatures above 1800 K thermal NO formation becomes significantly high. The equations below show the chemical reactions producing thermal NO during the combustion process.

$$O_2 \leftrightarrow 2O \tag{1.6}$$

$$N_2 + O \leftrightarrow NO + N \tag{1.7}$$

$$N + O_2 \leftrightarrow NO + O \tag{1.8}$$

$$N + OH \leftrightarrow NO + H \tag{1.9}$$

Reaction (1.7) proceeds at a much greater rate than the others and often is considered as the only reaction forming thermal NO. Although the reaction rate increases with more O_2, lowering φ helps reduce NO formation due to cooling of the hot gases.

NO may also be formed **via the N_2O intermediate** as follows

$$O + N_2 + M \leftrightarrow N_2O + M \tag{1.10}$$

$$H + N_2O \leftrightarrow NO + NH \tag{1.11}$$

$$O + N_2O \leftrightarrow 2NO \tag{1.12}$$

Where M is a third body and therefore elevated pressure has a favourable effect on reaction (1.10). This mechanism plays a major role in NO production under very lean conditions and low temperatures. Also when thermal NO is suppressed such as in FC, NO via N_2O may be the dominant route, as shown by Tobacco et. al [7].

Under fuel-rich conditions N_2 may also react with hydrocarbon fuel radicals such as C, CH and CH_2 to form **prompt NO** through multiple steps. In the literature, different causes of prompt NO formation are stated. In some works it is stated that the formation starts at temperatures higher than thermal NO formation which makes it also a function of temperature. In other works it is stated that lower combustor inlet temperatures increases prompt NO, but this happens at idle thrust setting where the overall NO_X emissions are very low. The formation of prompt NO is small as compared to thermal NO and is only of interest when a very low amount of thermal NO is formed.

1.1.4.2 Emission trade-off

Engineers are faced with a challenge when designing an aero engine combustor since raising the flame temperature is restricted due to consequent NO_X emissions. If the reaction rates are too low then formation of CO and UHC will increase (see figure 1.5). For conventional combustors a compromise has to be made and the operating conditions should be limited within the narrow 'low emissions window'. Typical minimum emissions occur between gas temperatures of 1600 and 1730 K. To escape this narrow temperature range requires innovative combustor designs.

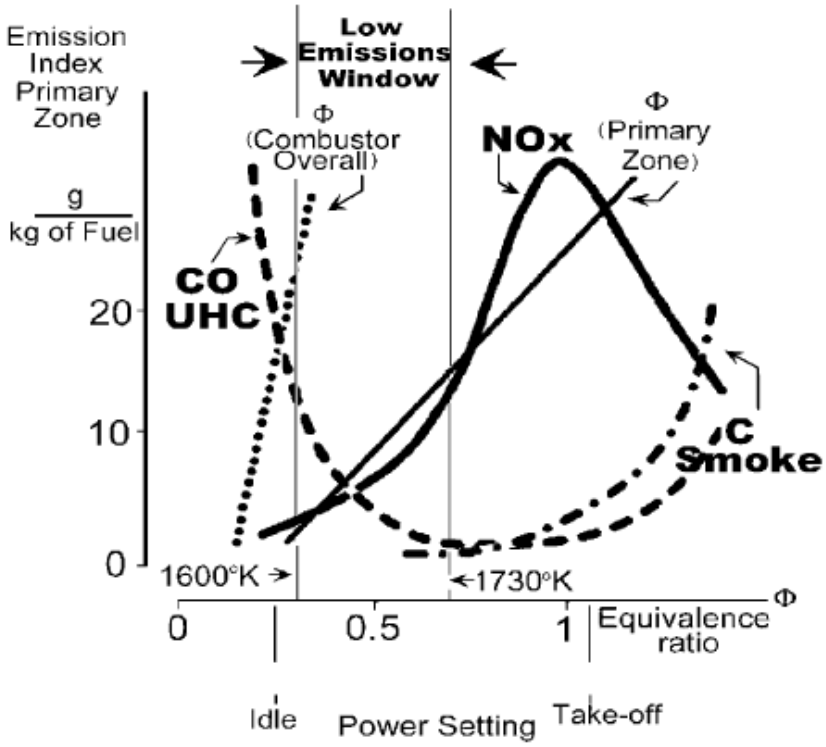

Figure 1.5 Compromises involved between emitted species and the ''low-emission window'' [8].

1.1.5 Flameless Combustion: The Concept

Flameless combustion is a relatively young combustion technology developed since the beginning of the 90's when one of the primary objectives was to reduce thermal NO drastically. FC is often described as a combustion regime with a flame that is not audible nor visible (hence the name 'flameless') due to its relatively low flame temperature and temperature fluctuations. The chemical reaction is very diffusive and spreads out through the whole combustion chamber, smoothening the temperature distribution and potentially eliminating hot spots which are the main sources of thermal NO production.

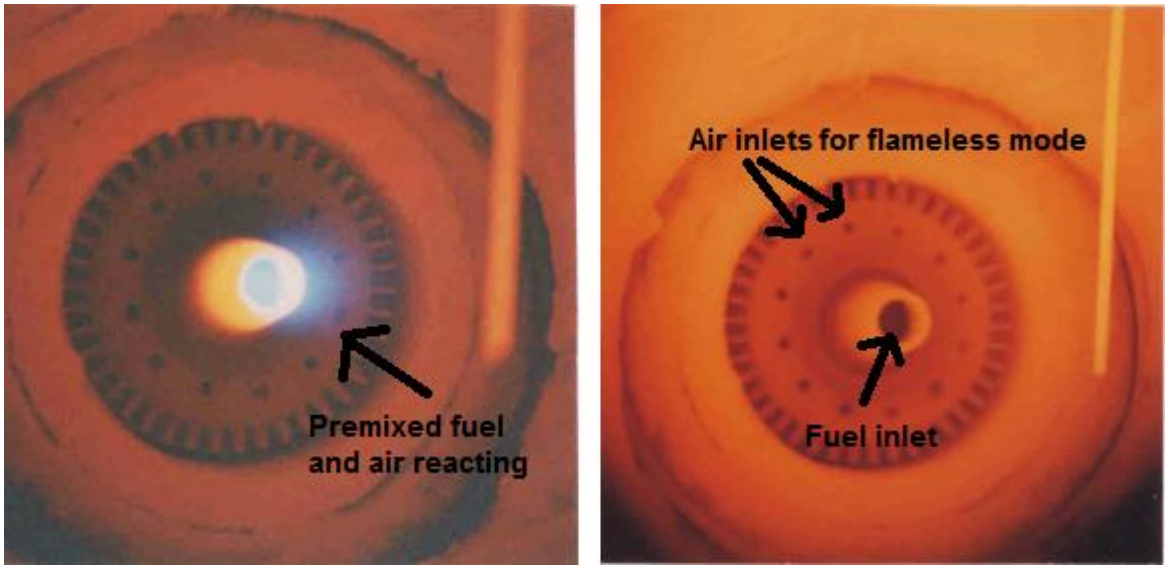

Figure 1.6 FLOX® burner with normal combustion (left) and flameless combustion (right). Notice that the flame is invisible in the right picture.

Its characteristics has been given many names in the literature, e.g. Flameless Oxidation (FLOX)[9], High Temperature Air Combustion (HiTAC)[10], Mild Combustion (MILD)[11] and Low NOx Injection (LNI)[12]. The initial investigations under these alternative names have been mostly applied to industrial furnaces but since the early 2000's, much attention has also been given on its application to GTEs.

Like most other low NO_X combustion technologies, FC also reduces thermal NO formation due to the reduced flame temperature. The requirements that need to be fulfilled in order for FC to occur are stated slightly different in some investigations, e.g. MILD combustion, but generally it comes to the following two conditions:

- The temperature of the reactants prior to reaction has to be above the auto-ignition temperature.
- The reactants have to be diluted by mixing the exhaust (or other inert) gases with the incoming air flow, in order to reduce the oxidant concentration.

The initial concern that comes across with the first requirement is that raising the temperature of the oxidant would lead to an increase of the flame temperature at near stoichiometric reaction in the flamelets (assuming a diffusion flame) which will only increase the formation of thermal NO exponentially, as can be seen in figure 1.7.

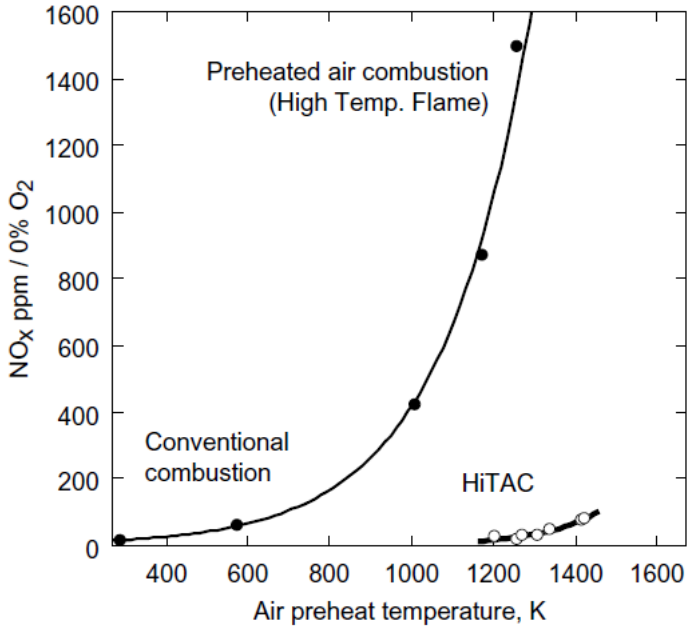

Figure 1.7 Effect of preheat temperature on NO_X formation [10].

However, it is the combination with the second requirement that makes FC work. When looking at a typical diffusion (or non-premixed) flame, the key is to reduce the oxygen concentration by means of dilution with inert gases (such as combustion products) so that the reduced oxygen fraction causes the reactants to react at a lower rate. Therefore the thin reaction zone of a diffusion flame thickens, increasing its volume in order to burn the same amount of fuel as in normal combustion. This results in the same total heat release as with a diffusion flame, but with lower peak temperature and moderate temperature rise (see figure 1.8), decreasing thermal NO formation.

The reduced reaction rate due to dilution may be especially problematic under high Re flows which may cause dispersion of the radicals in the reaction zone and also more heat dissipation of the flame. This would lead to unstable combustion and even flame extinction. In order to stabilise the flame, the reduced reaction rates of the reactants need to be increased to a satisfactory level, which is certainly the case if the temperature is above auto-ignition temperature.

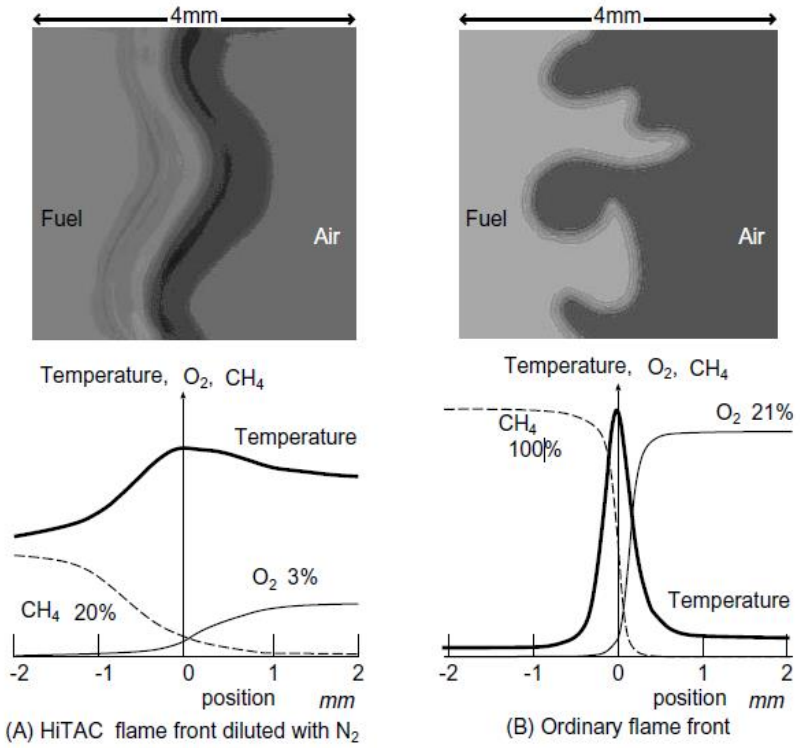

Figure 1.8 Thickness of the reaction zone (centred at 0) and temperature rise [10]

The two requirements for FC are usually achieved by allowing some of the gas products to recirculate and mix with the reactants. The recirculation ration (K_V) is a very important parameter in FC. The most implemented definition of K_V was given by Wünning [9] as follows

$$K_V = \frac{\dot{m}_{rec}}{\dot{m}_{fuel} + \dot{m}_i} \tag{1.13}$$

Where $\dot{m}_{fuel}$, $\dot{m}_i$ and $\dot{m}_{rec}$ are respectively the mass flows of the fuel, the inflowing air and the upstream flowing recirculated gas products that mixes with the fuel and air prior to ignition. The recirculating hot gas products both dilute and heat up the reactants above auto-ignition temperature. In order to reach a stable FC regime, K_V must be higher than 3 according to Wünning. Figure 1.9 shows a schematic comparison between a conventional industrial furnace burner and FC where exhaust gases recirculate.

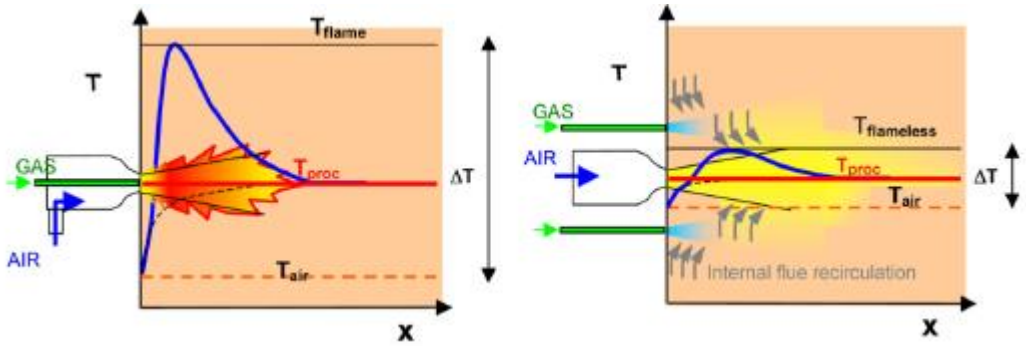

Figure 1.9 regular furnace combustion (left) and FC (right) [13]

In FC the reaction rates are slow and comparable with the flow mixing rate due to the enhanced turbulence so that Da ≈ 1, approaching a well stirred reactor. This value is crucial in order to create this combustion regime. This combination of preheating, dilution and high turbulent mixing of the reactants produce very stable reaction zones expanding through the whole furnace, leading to almost uniform temperature profile. Due to the low temperature fluctuations as shown in figure 1.10, also very low thermos-acoustic oscillations are achieved.

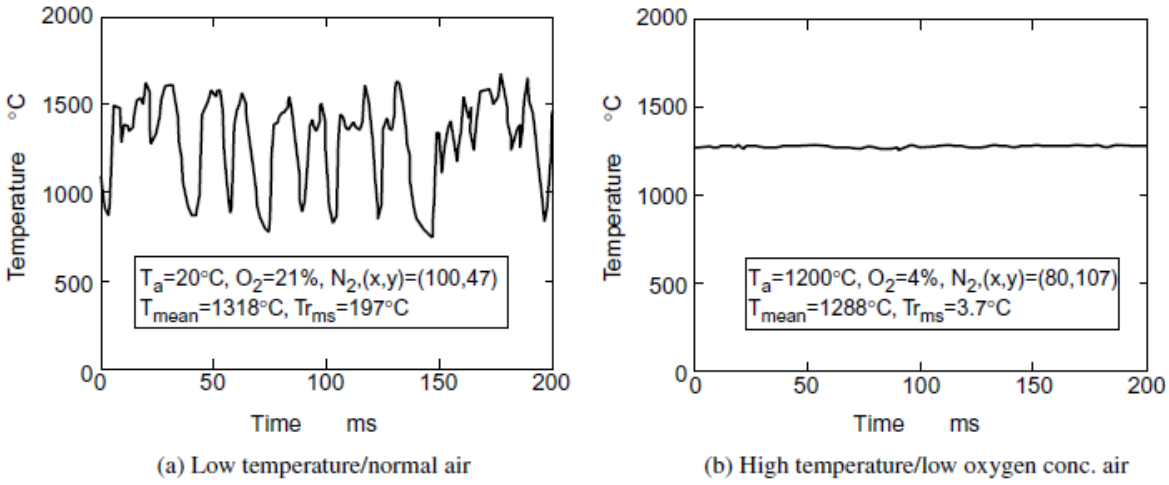

(a) Low temperature/normal air

(b) High temperature/low oxygen conc. air

Figure 1.10 Temperature fluctuations as a function of time in (a) normal combustion and (b) flameless combustion [10]

As already metioned at the introduction of this chapter, the adiabatic flame temperature is much lower and hot spots are spread out, minimizing thermal NO to form. However, there is a limit to the amount of NO_X that can be reduced. In the region where temperature dependency is low, other NO_X formation routes will be dominant. Based from the initial FC studies this implied that reducing the chamber temperature would reduce NO_X only as low as 10 ppm [10]. However in later studies it was shown that FC can produce NO_X concentrations even lower than 10 ppm.

Tobacco et al. [7] conducted a theoretical and numerical investigation on the chemical kinetics in FC and discussed and found out that the NO_x abatement in FC is not only due to the well-known thermal effect but also, to some extent, due to the involvement of combustion products in the reaction zone. Especially water steam plays an important role in weakening all NO_x kinetic paths by consuming O radicals from the radical pool in the so called water removal reactions:

$$O + H_2O \rightarrow H + HO_2 \quad (1.14)$$

$$O + H_2O \rightarrow 2OH \quad (1.15)$$

The second advantage of the combustion products H_2O and CO_2 is that they help reduce the flame temperature due to their relatively high heat capacity.

Another problem that might appear with lower flame temperature is that CO emissions will increase as discussed in section 1.1.4.2. However, it was proved by FC that the low emissions window does not really apply to this combustion mode and that CO emissions still reduced at lower temperatures. Two reasons may explain this. The first is that the presence of a uniform temperature profile and absence of cooling flow (in order to make recirculation possible) prevent sudden temperature drops that would prevent CO oxidation. Another reason that might be a cause is that the high concentration of steam in the gas products that mixes with the reactants promotes the reaction that is dominant at lower temperatures, according to reaction 1.5.

Another practical advantage of FC is that reactions typically occur at a further distance from the burner (reducing its thermal stress) as compared with conventional combustors that use bluff bodies or aerodynamic stagnation points near or in the burner for flame holding.

Figure 1.11 shows a schematic representation of the non-premixed combustion regimes in terms of O_2 concentration, reactants temperature and K_V [14]. In a GTE there is always some amount of recirculation due to swirl stabilization. Normal non-premixed combustion is possible over the whole range of chamber temperature but only for recirculation rates up to 30% [9], which increases a little at higher temperatures. For higher recirculation rates, the flame will become unstable (lifted flames) and blow out may occur even for temperatures above self-ignition. If the furnace temperature and K_V are sufficiently high, the reactions become steady and reaching the FC regime. However, to the FC regime the furnace must be heated up first and this can be especially challenging for GTEs. As can be seen in the figure, a wide range of stable combustion is currently unused in GTEs.

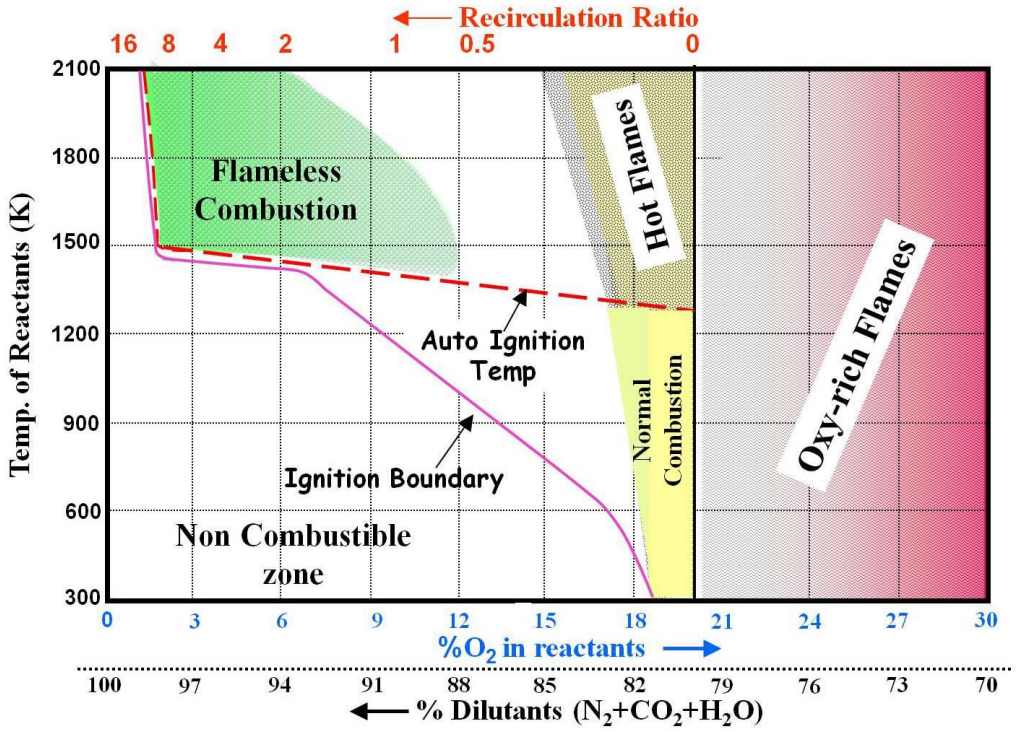

Figure 1.11 schematic representation of the non-premixed combustion regimes in terms of O_2 concentration, reactants temperature and KV [14]

1.1.6 Application to Gas Turbine Engines

As lean instabilities become an increasing problem for higher pressure ratio engines, FC is a very attractive candidate for application in aero engines mainly because stable combustion and low pollutant emissions can be achieved with practically no weight and complexity addition to the engine. These are two very important cost-related limitations. However, the fluid-chemical interaction inside the combustion chamber should be able to cope with the wide range of operation conditions without losing its stability. The challenges of applying FC in GTEs were discussed in several studies [15][16][17].

GTEs differ from industrial furnaces by being smaller, adiabatic and operating at elevated pressure [18]. Higher pressure reduces the chemical reaction timescale, which may increase the Damköhler number. GTEs also operate at very fuel-lean conditions in order to reduce the specific fuel consumption and to cool the hot gas temperature to a level that the combustor liner and turbine blades can withstand. Instead of using heat exchangers, the inlet air is preheated by and only dependant on the compressor. As a consequence of the much lower equivalence ratio in a GTE as compared to a furnace, a large portion of O_2 remains unconsumed after combustion which makes it difficult to lower the O_2 concentration with Exhaust Gas Recirculation (EGR) alone.

Table 1.2 shows the compressor discharge temperature and equivalence ratio for the most operation conditions of a typical aero engine with a compression ratio of 32:1, at sea level. It is clear that the inlet conditions at any operation mode are not suitable for FC. Exhaust

recirculation with a K_V of at least 3 can overcome this issue for most operation modes (figure 1.12). In idle mode however, even with K_V far beyond 3, the O_2 concentration and pre-combustion temperature barely meet the requirements. Although much higher compression ratios are achieved in current aero engines. In order for the reactants to auto-ignite, a temperature of at least 800 K and sufficient residence time is required [17]. Otherwise, stability is in danger.

Table 1.2 Typical Aero engine operation conditions with a 32:1 compression ratio compressor[17].

Parameters/Engine Conditions	Takeoff	Climb	Approach	Idle
Discharge T (°K)	822	786	639	511
Equivalence Ratio	0.496	0.460	0.343	0.250

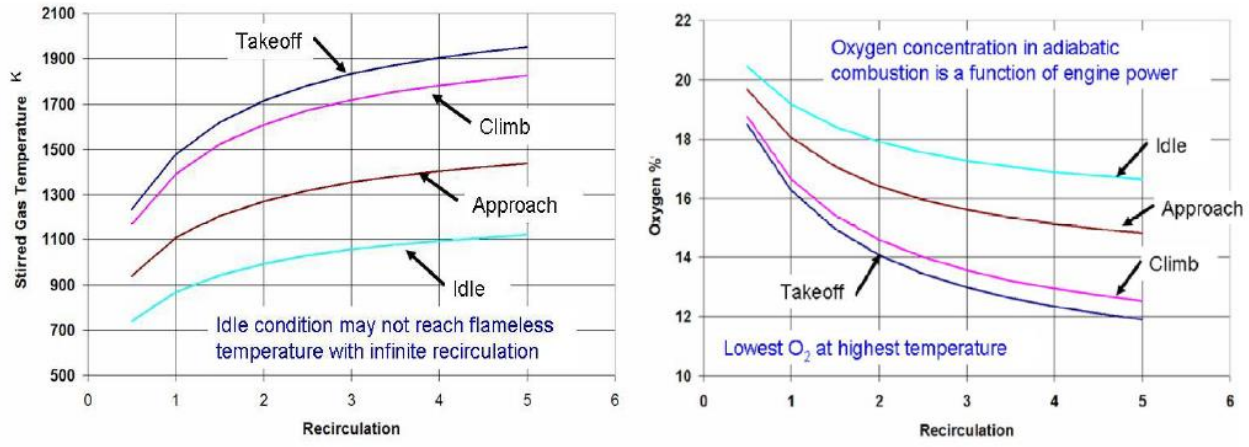

Figure 1.12 Aero engine combustor performance in terms of exhaust gas recirculation, mixed reactant temperature and reactant oxygen concentration with a 32:1 Compressor. [17]

Guillou et. al [16] also mention two other important limitations of FC to apply on GTEs. The first is that the thermal NO reduction effect is challenged by the requirement of sufficiently high Turbine Inlet Temperature (TIT). Although the combustion efficiency of FC is higher than in conventional combustion, the cycle efficiency, which is related to fuel specific consumption, is dependent on the TIT. Lowering the temperature rise inside the combustor too much will have an adverse effect on the fuel economy. Secondly, creating sufficient EGR requires a combustor volume much larger than conventional combustors. This practical limitation is especially important for aero engines as other engine components may have to be redesigned.

Since the early 2000's there were several projects involved in designing an aero engine combustor with FC technology while taking the mentioned challenges into consideration, such as the FLOX burner developed at DLR in Germany and the FLOXCOM burner at Technion

in Israel. Also the University of Cincinatti worked on a FC chamber for aero engines. The mentioned projects showed promising results in terms of emissions and their combustors are patented [15][16][19][20].

An additional study was carried out at Technion where a different FC chamber methodology was proposed that could tackle all the major difficulties of applying FC to a GTE and aero engine. The methodology will be adopted in this thesis. The schematic of the combustor is shown in figure 1.13. In here, the major part of the gas enters the combustor dome (or liner) through the centre where it entrains the hot mixture of fuel and gas products that have already partially reacted and combustion continues. Downstream of the combustion zone, the secondary air enters the liner and mixes with the primary flow to reduce the temperature to the level appropriate for the turbine to handle.

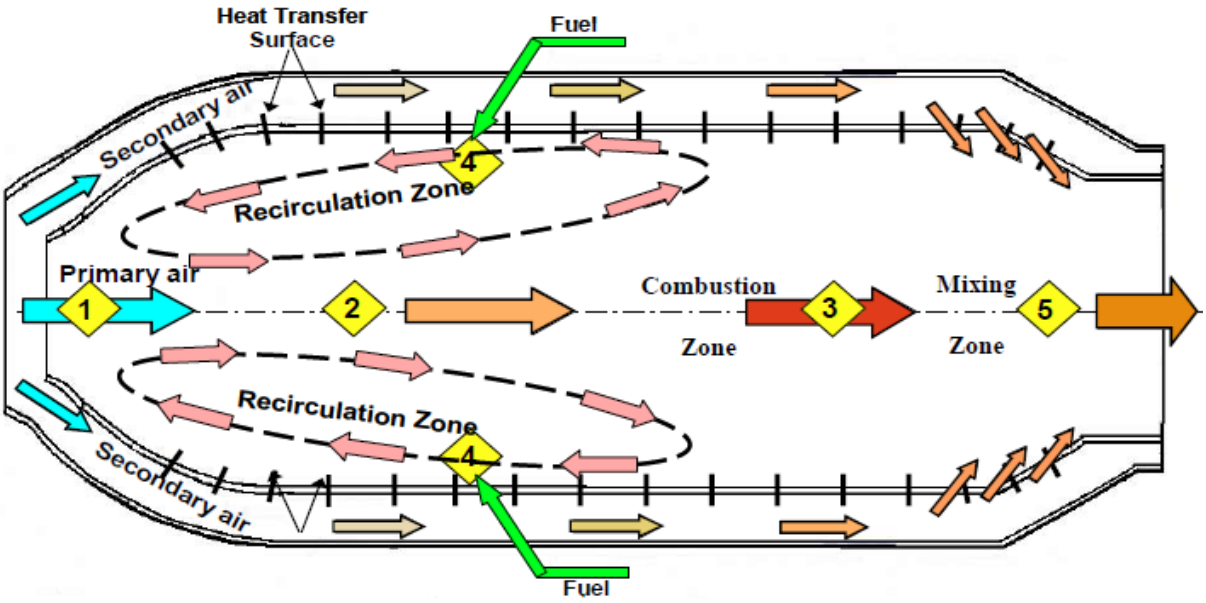

Figure 1.13 Schematic of a Gas Turbine Combustor Operating on the Newly Proposed Cycle [14]

The key feature in this methodology is that the secondary air extracts heat from the primary zone by means of conduction and convection in order to reduce the maximum temperature. This heating of the secondary air also allows less excess air to enter the primary zone and for φ to increase. EGR alone was believed to be insufficient in decreasing O_2 concentration due to the low φ in gas turbine combustors. A thermodynamic and chemical kinetic analysis was carried out and it confirmed the favourable effect of heat extraction in reducing both NO_X and CO emissions ($[NO_X] < 50$ ppm and $[CO] < 1$ ppm). An important result was that both NO_X and CO behaved similar in relation to temperature as a consequence of EGR and heat extraction, hence eliminating the narrow low emissions window (discussed in section1.1.4.2) that obstructed engineers in designing low-NO_X combustion chambers.
However, the promising results had to be verified by CFD analysis as a next step.

1.2 Thesis Objective

The objective of this thesis was to design a flameless combustion combustor for the aero engine, based on the proposed design methodology in order to create clean and more quiet engines for the future. Previous studies have shown promising results in applying FC to aero engines, however they have also left unanswered fundamental questions. What was the underlying reason for their choice in the configuration and geometry? Have the engine size restrictions been taken into account or do the combustors require a whole new engine design? Can the combustors perform just as good with real aero engine conditions, such as elevated pressure and high excess air? Can the design be fit in an aero engine without compromising pressure loss and complexity? These questions triggered the need to do research about creating an optimal flameless combustor design and led to the following research question:

Q1 *'Is it possible to create a flameless combustion chamber suitable for aero engines that is able to generate the conditions for flameless combustion to occur without compromising pressure loss and structural complexity?'*

The proposed methodology was particularly interesting due to its simplistic design: a cylindrical shape (or an 'annular shaped duct') with the main air flow entering the combustor in the middle. This was a good starting point towards the final design. Therefore in order to investigate its viability for an aero engine (thus answering the research question) the following sub questions had to be answered.

Q1.1 *-How can the combustor be shaped to get sufficient recirculation and acceptable pressure loss?*

Question 1.1 could be potentially answered by conducting cold flow simulations on different 2D and 3D geometries. The following questions had to be kept in mind when changing the geometry.

Q1.1.1 -*What is the relation between inlet velocity and recirculation ratio?*

Q1.1.2 -*What geometrical parameters can be used to enhance recirculation?*

Q1.2 *-How does recirculation ratio affect NOx/CO emissions?*

Question 1.2 was related to combustion, which meant that reacting flow simulations had to be made to find the answer. During this step, the following questions popped up which would give a good physical understanding when they were answered.

Q1.2.1 *How will combustion change the recirculation zone and recirculation ratio as compared to non-reactive flow?*

Q1.2.2 *How can the geometry parameters be modified to minimize emissions.*

It was important that the pressure loss should be within operational limits and that NO_X emissions should be very low without negatively affecting CO emissions.

2

Computational Fluid Dynamics

CFD was used as a tool to gain a preliminary understanding of the combustor design, its related flow behaviour and reactions. However, in order to make a CFD calculation as accurate as possible, a proper turbulence model and combustion model had to be selected that were suitable for modelling FC. Thus a basic understanding of the models was required. The variety of models discussed shall be limited to the ones that are implemented in ANSYS Fluent, which was the simulation software that was used for this thesis work due to its respected performance in modelling turbulent combustion and because it was an available resource at the TU Delft.

2.1 Governing equations

The basic equations for a combustion process follow from fluid conservation laws with additional equations describing chemical reactions. The coupling between convection, diffusion and chemistry makes combustion one of the most complex flow phenomena to analyse. In order to model combustion accurately, the model should be capable in solving the conservation (or transport) equations for fluid flow, heat transfer and combustion chemistry. The first equation follows from the conservation of mass

$$\frac{d\rho}{dt} + \nabla \cdot (\rho \vec{u}) = 0 \tag{2.1}$$

where ρ is the fluid density and $\vec{u}$ the fluid velocity vector (may also be denoted as u_i). Equation 2.1 is also called the continuity equation. The second equation describes the conservation of momentum

$$\frac{d(\rho \vec{u})}{dt} + \nabla \cdot (\rho \vec{u}\vec{u}) = -\nabla p + \nabla \cdot \tau + \rho \vec{g} \tag{2.2}$$

where $\rho \vec{g}$ is the gravitational force and τ is the stress tensor given by

$$\tau = \mu\left[(\nabla\vec{u} + \nabla\vec{u}^T) - \frac{2}{3}\nabla\cdot\vec{u}I\right] \tag{2.3}$$

in which μ is the dynamic viscosity and I is the unit tensor.
Equations 2.1 and 2.2 in combination with 2.3 are also known as the Navier-Stokes equations. Since heat transfer (which applies for combustion) and compressibility in the flow cannot be neglected, a third equation that defines the conservation of energy also needed to be solved.

$$\frac{d(\rho E)}{dt} + \nabla\cdot(\rho E\vec{u})) = \nabla\cdot\left(k_{eff}\nabla T - (p\vec{u}) - \sum_j h_j\vec{J}_j + (\tau_{eff}\cdot\vec{u})\right) + S_h \tag{2.4}$$

Where k_{eff} is the convective conductivity, $\vec{J}_j$ the diffusion flux of species j and S_h a heat source due to chemical reaction. E is the total energy per unit mass which is the sum of internal energy e and kinetic energy $\frac{1}{2}\vec{u}^2$.
The last transport equation needed to be solved is the conservation of species

$$\frac{d(\rho Y_i)}{dt} + \nabla\cdot(\rho\vec{u}Y_i) = -\nabla\cdot\vec{J}_i + R_i \tag{2.5}$$

Where Y_i is the local mass fraction of each specie and R_i is a chemical source which defines the net production of each specie due to chemical reaction. Equations 2.1 to 2.5 follow from the conservations laws which in general can be applied to every scalar quantity ϕ and is of the following form

$$\frac{d(\rho\phi_k)}{dt} + \nabla\cdot(\rho u_i\phi_k) = \nabla\cdot(\Gamma_k\phi_k) + S_{\phi_k} \tag{2.6}$$

Where Γ_k is a diffusion flux and S_{ϕ_k} a source term. In case the flow may be assumed incompressible, the terms containing the time rate of change of density in all transport equations are equal to zero.

2.2 Modelling Flameless Combustion

The numerical code Fluent and many other codes are able to model turbulent reacting flows by solving equations 2.1 to 2.5. There are different numerical methods to predict the flow behaviour. The equations could be either resolved as with Direct Numerical Simulation (DNS), or approximated with models as with e.g. the Reynolds-averaged Navier-Stokes (RANS), or both. The flow in flameless combustion is turbulent. Turbulent flows are highly unsteady, three dimensional and consist of a wide range of length and time scales called ‘eddies’. Due to this wide range, solving the equations directly with DNS (the most accurate

method) requires extreme computational cost which becomes prohibitive for large Reynolds numbers. So far, most attempts in predicting the behaviour of FC numerically were RANS based methods, which will now be studied more into depth.

Every scalar quantity can be decomposed into the time-averaged value (or ensemble averaged in case of unsteady flow) and a fluctuating component about that value

$$\phi(x_i,t) = \bar{\phi}(x_i) + \phi'(x_i,t) \tag{2.7}$$

Where $\bar{\phi}$ and ϕ' are the time-averaged and fluctuating components respectively. In the case of the momentum equation, the fluid velocity is decomposed and can be written as

$$\vec{u}(x_i,t) = \bar{\vec{u}}(x_i) + \vec{u}'(x_i,t) \tag{2.8}$$

In the RANS method the flow velocity component in the Continuity and Navier-Stokes equations (eq. 2.1 and 2.2) is substituted by equation 2.8 and a time-average is applied to the equations . This is called 'Reynolds' averaging and leads to the following equations for compressible flow (note that the Nabla symbol can also be written as $\frac{\partial}{\partial x_i}$):

$$\frac{d\rho}{dt} + \frac{\partial}{\partial x_i} \cdot (\rho \bar{u}_i) = 0 \tag{2.9}$$

And

$$\frac{d(\rho \bar{u}_i)}{dt} + \frac{\partial}{\partial x_j}(\rho \bar{u}_i \bar{u}_j + \rho \overline{u_i' u_j'}) = -\frac{\partial p}{\partial x_i} + \frac{\partial}{\partial x_i}\tau + \rho \vec{g} \tag{2.10}$$

What can be noticed is that the adapted momentum equation (2.10) has an additional term $\rho \overline{u_i' u_j'}$ which is the *Reynolds stress*. Analogously, if the Reynolds averaging is applied to the general transport equation of a particular scalar(2.6), this will also lead to an additional term $\rho \overline{u_i'} \overline{\phi_k'}$ called the *turbulent scalar flux*.
These additional Reynolds stresses lead to the problem that there are more variables than equations. In order to close equation2.10, the Reynolds stresses has to be approximated and therefore modelling is required with the help of turbulence models. Since the equations are not solved exactly and the fact that the unsteadiness of the mean flow is neglected, the RANS method is less accurate than DNS which is the major disadvantage. However the computational cost is much less compared to DNS, which makes it highly practical in the engineering industry.

A compromise between the two schemes is Large Eddy Simulation (LES). In the LES method only large turbulence scales are resolved (like DNS), whereas the effect of the smallest and most expensive scales are modelled (see figure 2.1). Although it can overcome some

disadvantages of RANS methods and it was shown to better predict flameless combustion in recent years, the computational cost is still very high for reacting flow modelling.

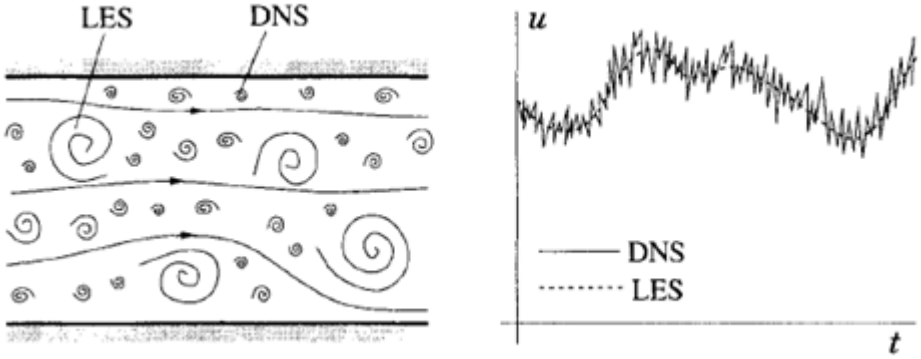

Figure 2.1 Schematic representation of turbulent motion (left) and the time dependence of a velocity component at a point(right). [21]

2.3 RANS based models

In order to model FC with RANS calculations, the right turbulence and combustion models had to be chosen that were most suitable in predicting the combustion characteristics.

2.3.1 Turbulence models

A common method to approximate the Reynolds stresses is to apply the Boussinesq hypothesis which is based on the assumption that in turbulent flow, the relation between the Reynolds stess and viscosity is similar to that of the stress tensor in laminar flow but with increased (turbulent) viscosity. Many turbulence models employ the Boussinesq hypothesis. The relation is of the following form (for compressible flow):

$$-\rho\overline{u_i'u_j'} = \mu_t\left(\frac{\partial u_i}{\partial x_j}+\frac{\partial u_j}{\partial x_i}\right)-\frac{2}{3}\left(\rho k+\mu_t\frac{\partial u_k}{\partial x_k}\right)\delta_{ij} \tag{2.11}$$

where μ_t is the turbulent viscosity and k the turbulent kinetic energy represented by (for 3D flow):

$$k=\left(\frac{1}{2}\overline{u_x'u_x'}+\frac{1}{2}\overline{u_y'u_y'}+\frac{1}{2}\overline{u_z'u_z'}\right) \tag{2.12}$$

The most widely used turbulence models to simulate gas turbine combustion are of the k-ε variant and have been applied to almost all FC models so far. The k-ε turbulence models solve two additional transport equations, one for the turbulent kinetic energy k and the other for its dissipation rate ε. While the transport equation for k is derived mathematically exact, constants are added to the transport equation for ε that are determined via practical

reasoning. This makes the two transport equations semi-empirical. With *k* and *ε*, the turbulent viscosity can be determined by the following relation:

$$\mu_t = \rho C_\mu \frac{k^2}{\varepsilon} \tag{2.13}$$

Where C_μ is a dimensionless constant or a function, depending on the model that is applied. Knowing *k* and *ε* yields μ_t, and combined with Boussinesq hypothesis give the Reynolds stress.

Previous attempts in modelling flameless combustion have been carried out mostly with the Standard *k-ε* variant as the turbulence model. Despite of its weaknesses such as inaccurate prediction of the spreading rate of axisymmetric jets (but accurate for planar jets), which is thought of being caused by the modelled transport equation for the dissipation rate *ε*, the model showed satisfactory results [22]. The Realizable *k-ε* model that was proposed by Shih et al. [23] overcomes these weaknesses by deriving a new ε equation based on the dynamic equation of the mean-square vorticity fluctuation. Also, unlike the Standard *k-ε*, the C_μ in equation 2.13 is no longer a constant but a function of the mean strain and rotation rates, the angular velocity of the system rotation, and the turbulence fields *k* and *ε*. This gives the Realizable *k-ε* superior performance over all the other *k-ε* models in predicting flow features containing strong streamline curvature, vortices, rotation and separation [24]. Strong streamline curvatures and rotation are a characteristic of flameless combustion which makes the Realizable *k-ε* the best candidate in modelling flameless combustion [7].

In the work of Vaz [25], different turbulence models were applied in the modelling of flameless combustion and were compared with experimental data. It was found out that the Realizable *k-ε* model matched the experimental data best. Christo and Dally [26] however concluded that out of the three *k-ε* models, the Standard *k-ε* model with modified constant of the dissipation equation provided the best agreement with their experimental results. However their 'jet in hot and diluted coflow' (JHC) burner model seemed an unsuitable design for aero engine combustor, and also no direct exhaust recirculation was observed, nor was it discussed by the authors. Nevertheless, the Standard *k-ε* model with modified dissipation constant may also be considered as a candidate model.

2.3.2 Combustion models

It would be advantageous to model the energy equation and the conservation of species in the same way as the turbulence models that are applied to the velocity flow field. Unfortunately when applying Reynolds averaging, the mean source term is of a different nature compared with the Reynolds stress and strongly nonlinear [4]. This requires different methods to close the energy and species conservation equations, which can be achieved with combustion models.

The combustion models discussed in this chapter are based on RANS and can be distinguished in two classes: conserved scalar based models and volumetric reaction based models. A selection of models that are often used for gas turbine combustion will be further described in more detail and also assessed for their applicability in FC.

2.3.2.1 Conserved scalar based models

A common method in non-premixed combustion is to reduce the thermochemistry of the reacting fluid into one single parameter called mixture fraction, f, which is the normalised local element mass fraction originating from the fuel stream. The main advantage of mixture fraction modelling is that, under assumption of chemical equilibrium and adiabatic flow, there exists a unique relation between the mixture fraction and thermochemical scalars, such as mass fraction of the species, temperature and density (for non-adiabatic flows, the thermochemical scalars are also a function of enthalpy of the flow). This makes f based models very efficient in terms of computational cost. However the molecular diffusivity of all species have to be considered the same. This assumption is acceptable for turbulent flows due to the much stronger influence of convection over molecular diffusion. f is defined as:

$$f = \frac{Z_i - Z_{i,OX}}{Z_{i,\,fuel} - Z_{i,OX}} \tag{2.14}$$

Here, Z_i is the local element mass fraction, the subscript fuel stands for the value in the fuel stream and the subscript *OX* stands for the value in the oxidiser stream. In the fuel inlet the value of f is 1 and in the oxidizer inlet it is 0. The mixture fraction is a conserved scalar, since the number of elements are conserved in chemical reactions. That means that the mean scalar transport equation (from equation 2.6) no longer includes a mean source term. The second reason why this way of modelling is computationally efficient is that chemistry is decoupled from the turbulent flow field by first calculating all chemical reactions for the whole domain of f, afterwards storing the thermochemical scalars in a table, and finally retrieving the scalars from the table after solving f at every point in the flow field. When applying mixture fraction modelling in RANS based simulations, two additional transport equations are solved in FLUENT as closure model, both for the mean mixture fraction $\overline{f}$ and for the variance $\overline{f'^2}$, where $f' = f - \overline{f}$. So in the end for non-adiabatic flow, the mean thermochemical scalar $\overline{\phi}$ (describing mass fraction, density and temperature) is a function of $\overline{f}$, $\overline{f'^2}$ and enthalpy h.

A combustion model that follows the principle of mixture fraction modelling is the mixture fraction Probability Density Function (f-pdf) model. This model is developed for non-premixed combustion and is based on chemical equilibrium (mixed is burnt). In here, the mean thermochemical properties are calculated and tabulated with the following function:

$$\bar{\phi}_i = \int_0^1 p(f)\phi_i(f)df \tag{2.15}$$

where $p(f)$ is the probability density function (between zero and unity) describing the temporal fluctuations of f in the turbulent flow. In this model, the pdf $p(f)$ is an assumed function of $\bar{f}$ and $\overline{f'^2}$, called β-function pdf. The main weakness of the f-pdf model is its infinite chemistry rate assumption, hence is not able to realistically predict slow reaction rates such as thermal NO formation. However, the accuracy can increase when slow reaction product concentrations are determined after post-processing. In the works of Vaz and Christo et. al [25][26], the model was found to be inadequate for modelling flameless combustion.

Another type of scalar based combustion model is the Steady Laminar Flamelet Model (SLFM), which can be considered as an extension of the f-pdf model. In the SLFM, a turbulent diffusion flame is modelled as an ensemble of discrete, steady laminar flames, also known as flamelets. Each of which is assumed to have the same structure as laminar flames in a simple configuration (such as the counter flow diffusion flame) and are concentrated just around the stoichiometric surfaces of the reacting mixture. This reacting mixture is assumed to be a thin layer that is smaller than the Kolmogorov turbulence scale. As already mentioned in chapter 1, turbulent flows can stretch the flamelets and because this is taken into account, the chemical time scale increases towards the turbulent flow time scale so that chemical non-equilibrium can also be predicted. The parameter that describes aerodynamic strain is the scalar dissipation rate χ, and can be considered as a measure of non-equilibrium. When χ increases, the non-equilibrium chemistry increases and when χ relaxes to zero, the chemistry tends to equilibrium which will bring us back to the situation of the f-pdf model. The mean thermochemical scalar is calculated in the same way as in the f-pdf model, except that it is not only a function of the mixture fraction, but also of the scalar dissipation rate

$$\bar{\phi}_i = \iint p(f,\chi)\phi_i(f,\chi)dfd\chi \tag{2.16}$$

where the turbulent mean scalar dissipation rate is modelled as,

$$\bar{\chi} = C_\chi \frac{\bar{\varepsilon}}{\bar{k}} \overline{f'^2} \tag{2.17}$$

In here, C_χ is a constant with default value of 2.[24] Before the transport equations are solved, the integration of equation 2.15 is pre-processed and stored in a look-up table, which is the same approach as with the f-pdf model except for an additional dimension represented by $\bar{\chi}$. The table also accounts for the number of flamelets in different strain fields by importing them from 'flamelet libraries' and embedding them in the turbulence

field. In the flamelet libraries different strained flame calculations were made and stored for a range of mixture fractions.

The SLFM assumes that the chemistry responds immediately to the aerodynamic strain, which limits the SLFM to model combustion with fast chemistry only and will not be suitable for predicting slow chemical reactions like NOx formation or low temperature CO oxidation. Hence, post-processing to incorporate the slow reactions is required.

The Unsteady Laminar Flamelet Model, particularly the Eulerian Unsteady Laminar Flamelet Model (EULFM) that was developed by Barths et al. [27], is one of such models used for post-processing the SLFM for which the equations involved will not be further elaborated in this thesis.
The principle however is the following. Pollutants form when they pass the flame front of the diffusion flame. The chemical time scale for NO_X formation is longer than that of the steady diffusion flame front that is simulated for the very fast main combustion reactions. That is why unsteady flamelets are needed to capture the slow reaction rate. Since the NO-concentrations are very low, they do not influence the temperature field and the mass fractions of the main species, hence simulation can be initially done with the SLFM (required in FLUENT).
The key operation of the EULFM is that the scalar dissipation rates of the fluid particles (represented by flamelets) in the steady flow field are modified depending on the path the fluid particles travel. Different particles cover statistically different flow paths, hence also different modification. The concentration of particles in each flow path is solved by means of an Eulerian unsteady passive scalar transport equation. Together with the transport equation of flamelet species that is a function of χ (now changing for every sub region/flow path), more accurate NO_X formation can be predicted. In the work of Coelho and Peters [28], the EULFM performed reasonably well in predicting NOx for the MILD combustion burner.

2.3.2.2 Volumetric reaction based models

Combustion models that are based on volumetric reaction basically approximate the highly non-linear mean reaction source term that results after applying Reynolds averaging on the equation of species mass fraction conservation (equation 2.5). The fundamental principle of 'Eddy' models, as will be discussed below, is the fact that the kinetic energy of the main flow is transferred to the largest eddy scales and dissipates by transferring the kinetic energy to smaller eddies, and into heat to a little extend.
The Eddy Dissipation Model (EDM) by Magnussen & Hjertager [29] goes by the idea that the overall rate of reaction is controlled by turbulent-mixing (eddy dissipation) and that the effect of the computationally expensive chemical kinetics on the reaction rate can be neglected. The reaction source term is determined in FLUENT from the smallest of the two reaction rates,

$$R_{i,r} = \nu'_{i,r} M_{w,i} A \rho \frac{\varepsilon}{k} \min_{reac} \left(\frac{Y_{reac}}{\nu'_{reac,r} M_{w,reac}} \right) \tag{2.18}$$

$$R_{i,r} = \nu'_{i,r} M_{w,i} A B \rho \frac{\varepsilon}{k} \left(\frac{\sum_P Y_P}{\sum_j^N \nu''_{j,r} M_{w,j}} \right) \tag{2.19}$$

Where $M_{w,i}$ is the molecular weight of species i, *reac* is a particular reactant, P is a particular product, $\nu'_{i,r}$ and $\nu''_{j,r}$ are the stoichiometric coefficient in reaction r for the reactant *i* and product *j* respectively, B and A are empirical constants. The problem with EDM that rises when modelling FC is that the chemical reactions rates are governed by the large eddy mixing time scale $\frac{\varepsilon}{k}$ and that reaction initiates as soon as turbulence occurs. This induces a complication that the reaction will start too soon and e.g. ignition delay being under predicted.

To help overcome this problem a finite-rate chemical kinetic source term should be added, which is done in the finite-rate/Eddy Dissipation Model (FR-EDM). In the FR-EDM, an additional finite-rate Arrhenius reaction source is calculated, which acts as a 'switch' since *before* ignition it is usually smaller than the eddy dissipation reaction rates (equation 2.18 and 2.19) and therefore the ignition can be delayed. After ignition, the eddy dissipation reaction rates take over since they are then generally smaller than the Arrhenius reaction rate. The advantage of the Arrhenius reaction source is that it incorporates the differing reaction rates for every reaction in the mechanism. The weakness however is that it ignores the effect turbulent fluctuation and therefore will be a problem to predict chemical reaction accurately in turbulent flows when fluctuations are high. The solution may be acceptable if the turbulent fluctuations are low and the chemistry is relatively slow.

Although the EDM's are computationally cheap and account for finite-rate chemical reactions, the main limitation however is that all chemistry mechanisms have the same turbulent rate of reaction when the eddy dissipation reaction rates control the model. This may lead to unrealistic prediction of multi-step chemistry where also free radicals are involved. In order to simulate flameless combustion successfully, detailed chemistry schemes are necessary to model auto-ignition accurately because auto-ignition is preceded by dilution and turbulent mixing of the reactants with the hot exhaust gases until the temperature is high enough.

The Eddy Dissipation Concept (EDC) developed by Magnussen [2] is an extension of the EDM that is able to handle detailed chemical reaction mechanisms in turbulent flows. It is a promising model for flameless combustion, but computationally costly. The notion of the EDC is that the very small eddy scales (in which the Kolmogorov scale is the smallest) are responsible for the dissipation of kinetic energy into heat. Reaction is assumed to occur in these turbulent scales, which are called fine scales, and cover a small fraction of the total

volume were the reactants are mixed homogeneously like in a well stirred reactor. The turbulence–chemistry interaction is handled using turbulent kinetic energy and it's dissipation rate to determine the size of the fine scales in which reactions occur and the corresponding chemical residence time governed by the Arrhenius rates, over which time integration is performed. The model solves the conservation equations for the mean species (equation 2.5) by modelling the source term R_i as

$$R_i = \frac{\rho(\gamma^*)^2}{\tau^*\left[1-(\gamma^*)^3\right]}(Y_i^* - Y_i) \tag{2.20}$$

Where Y_i^* is the fine-scale species mass fraction, γ^* the length fraction of the fine scales and τ^* the time that the fine scales are assumed to react. The latter two are defined as follows:

$$\gamma^* = C_\gamma \left(\frac{\nu\varepsilon}{k^2}\right)^{1/4} \tag{2.21}$$

and

$$\tau^* = C_\tau \left(\frac{\nu}{\varepsilon}\right)^{1/2} \tag{2.22}$$

Where ν is the kinematic viscosity. C_γ and C_τ are the volume fraction constants and time scale constants of the fine scales, respectively. EDC has shown satisfactory results in modelling FC when coupled with detailed reactions and showed to able to capture its volumetric feature and reduced flame temperature [7], [30]. It was also recommended by Vaz [25] to try EDC detailed reaction mechanism as the other models discussed here were not able to reproduce the data.

The downside of solving the reaction rates for all chemical reactions is that it requires longer run-time. Therefore chemical reactions have to be simplified by means of reducing the intermediate chemical reaction steps.

2.3.3 Summary of the combustion models

The extensive discussion of the combustion models are summarised in table 2.1.

Table 2.1. Summary of the combustion models

Models	Type	Advantages	Drawbacks
f **-pdf**	conserved scalar	-computationally cheap -covers all chemical reactions	-predicts only chemical equilibrium (infinite chemical reaction rate)
SLFM	conserved scalar	-covers also non-equilibrium (intermediate) chemical reactions -computationally efficient	-Only fast chemical reactions predicted.
EULFM	Post-processor (conserved scalar)	-Covers statistically also slower chemical reactions for the SLFM.	
EDM	Volumetric reaction	-computationally cheap	-effect of chemical kinetics on reaction rates ignored. -Small single-step mechanism
FR-EDM	Volumetric reaction	-computationally cheap -involves some effect of chemical kinetics on reaction rates.	-Unable to predict detailed (intermediate) chemical reactions.
EDC	Volumetric reaction	-Finite-rate chemistry -Can cover all chemical reactions	-Computationally costly -Chemical reactions need to be simplified to reduce computational cost

3

Cold Flow Simulation

Compared to a furnace or even an industrial GTE the core part of an aero engine is very compact where a relatively large mass of air flows through a relatively small space. In order to design a FC chamber, the right conditions had to be set in this limited space. Ultimately, enough recirculation needed to be generated to dilute the air and reduce its oxygen concentration. This chapter will go through the steps that led to the initial concept before it was tested with combustion.

Throughout the thesis, the design philosophy was not to come up with an accurately optimized geometry but to gain a qualitative understanding on the behaviour of the flow (and combustion later on) when certain geometry alterations were made. Finding different positive effects and merge them into one whole combustor shape was the guiding principle to achieve sufficient recirculation and acceptable pressure loss. Rather than retrofitting the traditional aero engine combustor, this design started completely from scratch, having only followed the proposed methodology described in section 1.1.6. The focus of the design lied only on the combustion dome and therefore the heat transfer between de primary and secondary flow in the dome and annulus respectively was out of the scope of this thesis.

Section 3.1 will describe how the design parameters were defined and a clarification will be given on the mesh generation and simulation set-up. In order to gain trust in the outcome of the simulations, the turbulence models were compared with experiments that were conducted on similar geometries. This will be discussed in section 3.2. The design steps that led to the first concept will be described in section 3.3.

3.1 Methodology

3.1.1 Combustor liner and inlet size estimation

As a starting point, the gas entry conditions and global size of the combustor were loosely adopted from a conventional turbofan engine, the General Electric CF6-80C. This type of aero engine powers a wide variety of civil aircrafts such as the Airbus A300, The Boeing 747-400 and the McDonnell Douglas MD-11.

The cross-section of this engine is shown in figure 3.1. Notice that the combustor is of the annular type. Since the fan inlet diameter is known (2.67 m), the diameter of the shroud of the combustor liner is estimated to be around 0.9 m. To leave some room for the rotor, annulus, and auxiliaries the hub diameter of the combustor liner should be at least 0.3 m. This leaves a distance between the hub and shroud of the liner which is referred to as 'liner height' of maximum 0.3 m and was the first design limit.

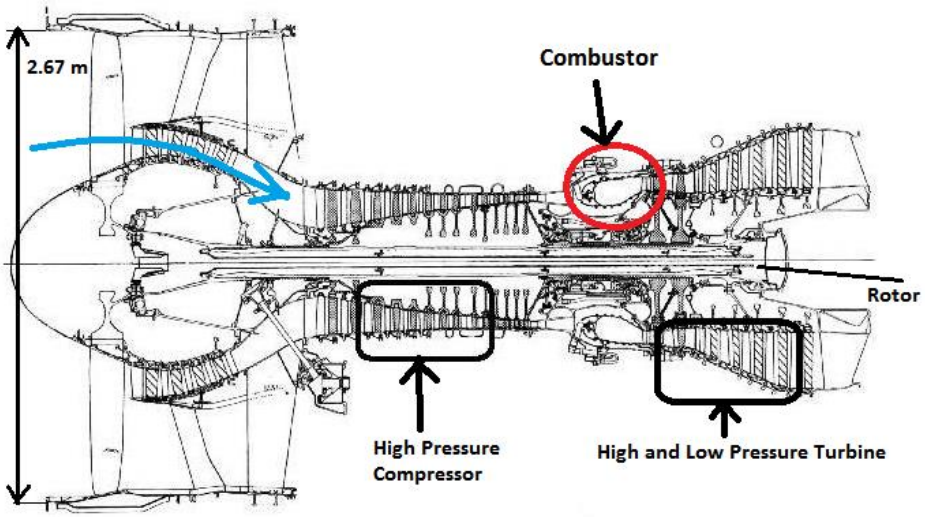

Figure 3.1 Cross section of the General Electric CF6-80C2 engine [31].

Table 3.1 shows the flow properties of the reference engine upstream of the combustor. Between the combustor and compressor there is also a diffuser which has the purpose to slow down the airflow before being injected in the combustor to prevent (in combination with a swirler) flame blow-off. Typically, the flow speed may vary from 50 m/s to nearly 200 m/s. The FC chamber however did not require a diffuser as the combustion process is normally considered very stable even with high air inlet velocities. However the inlet temperature had to be considerably higher than 822 K to keep stability when only low recirculation could be achieved. This problem will be discussed in chapter 4. Removing the diffuser will leave a design space for the combustor in the longitudinal direction (or 'liner length') of approximately 0.6 m.

Table 3.1 Design point flow properties between the HPC and Combustor of the GE CF6-80C2 at take-off [32].

Mass flow rate	130 kg/s
Total temperature	822 K
Total Pressure	29.44 bar
Density	13 kg/m^3

An initial design point injection velocity was chosen to be around 100 m/s as this was the velocity estimated at the compressor outlet [32] and a diffuser was claimed not to be required for the FC chamber. To achieve an air inlet size for this velocity, it was assumed that the air inlet was also of annular shape and placed exactly between the hub and shroud of the liner (at radii of 0.15m and 0.45m from the engines rotation axis respectively). This led to an inlet size in radial direction (or 'inlet thickness' in case of an annular combustor) of 0.053m. Rounding off the inlet size down to 0.05m would slightly increase the inlet velocity but this could be compensated when part of the air served as secondary flow.

3.1.2 Design variables

With the combustor size limitations defined, the next step was to find out how to design the combustor within that space to enable FC.

3.1.2.1 Geometry definitions: Can vs. Annular

Both the Annular Type Combustor (ATC) and Can Type Combustor (CTC) have been studied. Although they differ in shape, the geometry of the cross section is one of things they have in common. Figure 3.2 shows a simulation example with description of a confined jet in a straight channel, the starting point of the design process. *H* is the global liner dimension in radial direction. In case of an ATC it is the distance between the liner hub and shroud while for a CTC it is the liner diameter. *i* is the radial inlet dimension which is the 'thickness' of the annular jet in the ATC and the inlet diameter in the CTC. Looking at the cross-section only, *H* and *i* are respectively called liner height and inlet size for short. In section 3.3.2 a cavity will be added and more geometry features will be appointed.

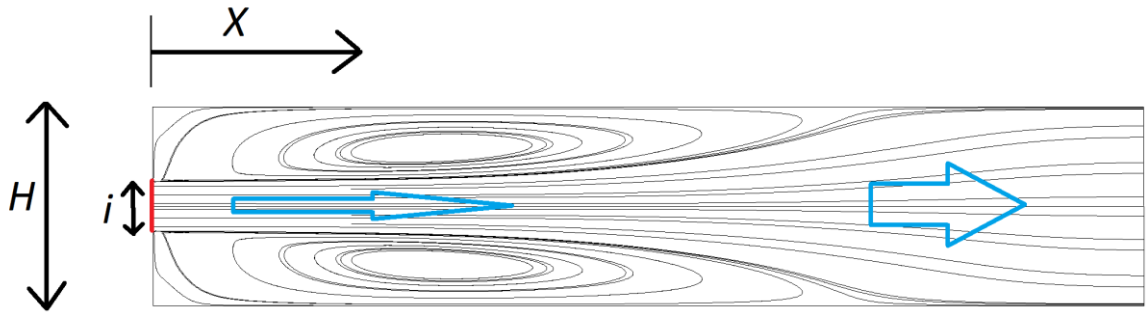

Figure 3.2 Streamline pattern of a confined 2D planar jet in a straight channel.

3.1.2.2 Recirculation Ratio

As mentioned above figure 3.2 shows the start of the design process. A confined jet by its own nature causes recirculation zones. When the jet passes through them it starts to lose momentum leading to a pressure rise and eventually it reattaches to the surrounding walls. The part of the vortex that flows back (negative X-direction) towards the inlet is called the recirculated flow. This mass flow rate was extracted from the simulations and by using the definition in section 1.1.5, K_V was found. The calculation tool that was made to determine K_V from the extracted data is provided in Appendix A.

There was an interest in seeing how the recirculation zones, K_V in particular, would react with the changing geometry. For the case of the confined jet the geometry variables were the inlet and liner height. Based on the literature it was expected that the circulation of the vortices would change proportionally with the injection speed and therefore K_V would not be influenced by this quantity. For the sake of certainty simulations have been conducted and confirmed this for velocities in the range of 50-200 m/s.

3.1.3 Mesh and Discretization Schemes

The integration volumes have all been generated with Gambit® 2.4.6. The use of a 2D mesh enabled to generate very fine grids varying from 60,000 to 250,000 cells, depending on the geometry size and shape. Although for cold flow simulations these amounts were excessive (well beyond grid independence), the benefit came when combustion models were added in the more complex geometries with detailed reaction mechanisms that led to relatively quick convergence with low residual errors.
The meshes were in general for the largest part structured but due to the grid refinement at the walls, unstructured meshing was unavoidable at convex corners (an example given in figure 3.3). More convex corners led to more unstructured meshing. Quadrilateral cells were mainly employed except for sharp corners at the wall where cells at the boundary layers were connected with triangular cells. This ensured that high quality cells were generated with skewness's, growth factors and aspect ratios (except near walls) being well below the maxima.
The grid has been refined at the wall such that the non-dimensional wall distances Y^+ of the adjacent cells were below 2.

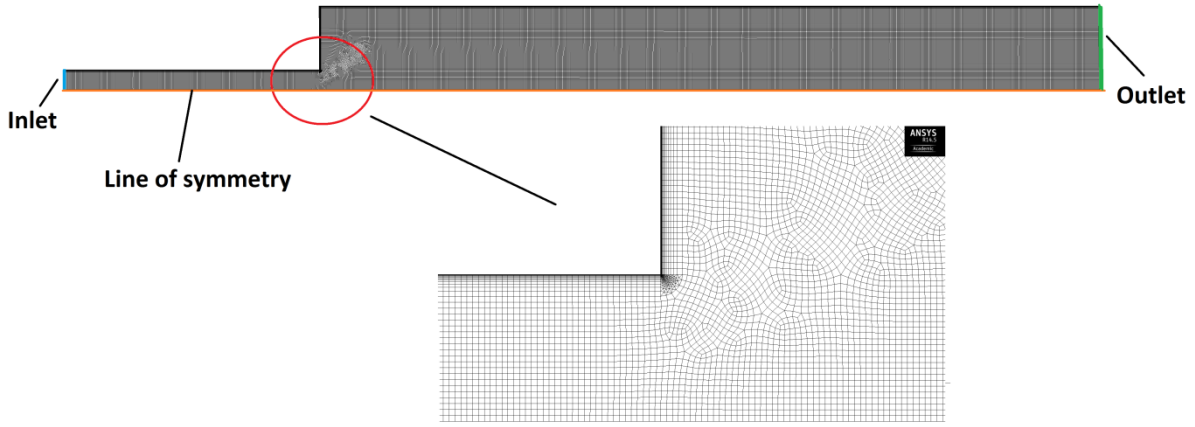

Figure 3.3 Mesh details of a confined jet case

The Fluent software follows the finite volume discretization approach. The second-order upwind scheme was used to solve the equations for momentum, turbulence parameters, energy, radiation and species. The pressure was interpolated using the PREssure STaggerring Option (PRESTO), which is similar to the staggered grid schemes, and was recommended in the Fluent Guide [24] instead of the 2nd order upwind scheme for problems involving high-speed rotating flows and flows in strongly curved domains. Although the PRESTO and 2nd order upwind scheme showed no difference in the cold simulations, the PRESTO scheme showed superior convergence in the combustion modelling where the flows were more energetic. The pressure and velocity fields were coupled with the SIMPLE algorithm.

3.1.4 2D vs 3D

Looking at figure 3.3, the symmetry line applied both for the ATC and CTC although for the CTC it is a symmetry axis. Benefitting from the axis symmetry of a GTE combustor the geometrical design has been limited to the longitudinal cross section only. This saved an enormous amount of runtime as it enabled do simulations in 2D.

However, one important simplification with 2D is that the air inlet of the ATC would also be annular (or even planar) shaped instead of divided into multiple circular jets, making the flow less complex and the combustion process easier to understand. For the CTC the circular jet remained circular in a 2D axisymmetric simulation, although the fuel inlet at the circumference of the liner was annular.

Secondly, to model the ATC with Fluent in 2D the axis-symmetry line had be placed outside the combustor, which required the full longitudinal cross-section to be meshed and hence doubled the amount of runtime. Due to lack of time the modelling of the ATC geometry was simplified even further in a 2D planar space, resembling a 'straight' combustor with a planar air inlet jet (radial cross-sections shown in figure 3.4 for clarification). In essence, the ATC did not differ much from the straight combustor except that the cross-sectional area of the outer half of the annular combustor was larger than in a straight channel with respect to the inlet area. And for cross-sectional area of the inner half of the ATC it was smaller. The difference in area led to vortices of different strengths in the outer and inner half of the ATC, which in theory should offset each other. Indeed, it was shown in the simulations that the total K_V was the same for both the ATC and straight combustor.

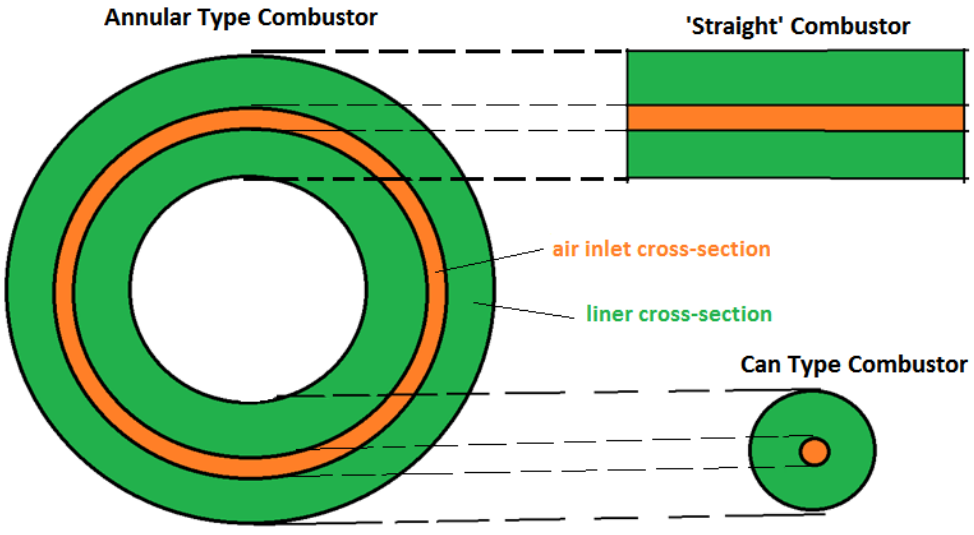

Figure 3.4 radial cross-sections of different combustors, with the air entering through the area highlighted in orange, in the direction normal to this page.

3.2 Validation of the turbulence models

To test the performance of the k-ε Realizable model, it was used in the simulation of an experimental model from Ruck and Makiola [33]. Their model is shown in figure 3.5. This channel flow with a backward-facing step shows a similar flow structure to that of the confined planar jet (basis for the design of the ATC), except that the flow entered the larger channel adjacent to the wall instead from the centre, thus only one recirculation zone was formed. Nevertheless, the flow types were similar. The simulation results were compared with the measurements by comparing the velocity profiles and recirculation ratio's at different positions in x-direction. Since only velocity profiles were provided to put as inlet boundary condition, the turbulence length scale and intensity were estimated using the given Reynolds number and empirical formulas for channel flows and jets. Also other turbulence models were used in the simulations. Three wind tunnel cases were compared where the only parameters that changed were the step height, channel height and inlet velocity profile at location x/H=-2.
Also attempts were made to reproduce the measured velocity profiles with LES modelling.

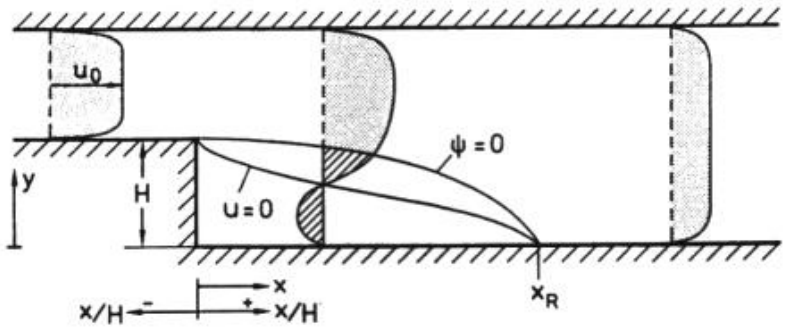

Figure 3.5 Schematic of the model of which experiments were conducted by Ruck and Makiola [33].

3.2.1 Results from RANS based simulations.

The measured velocity profiles were normalised by the reference velocity which was the maximum velocity at position x/H=-2 (inlet for the simulation model). The modelled velocity profiles with different turbulence models are shown in figure 3.6 for the case y15 [33] which had a channel-to-inlet height (or area) ratio of 3.27.

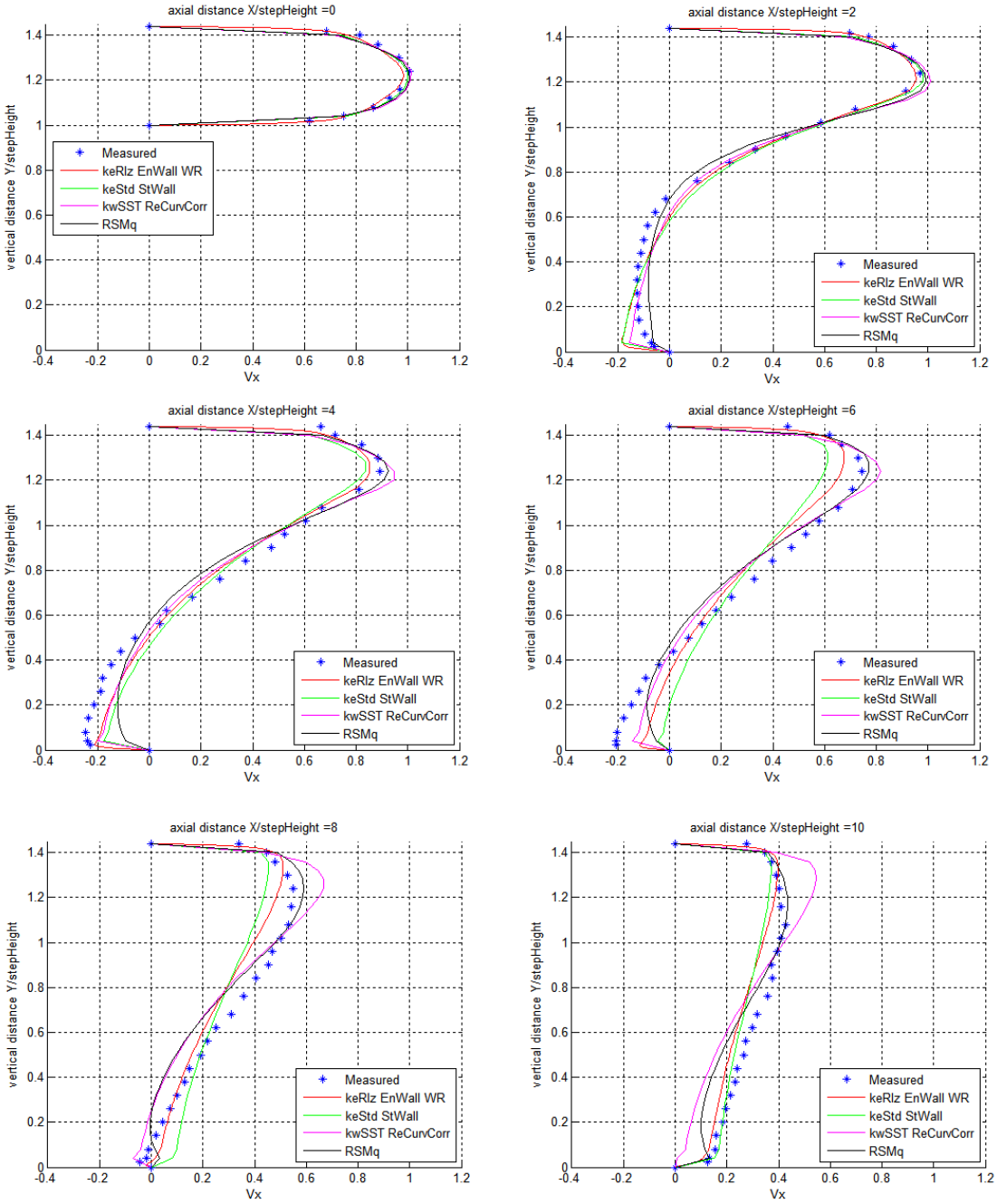

Figure 3.6 normalised x-velocity profiles of case y15 [33] at increasing (normalised) longitudinal positions, x/H. Re=15,000 ; measured reattachment length (normalised)=8.38 xr/H; step height=25mm; channel height=36.025mm; reference velocity 19.14m/s.

Most models showed reasonable agreement with the experiment. All models seemed to under predict the recirculated flow for the largest part. This is also the case for the velocities around the shear layer. After location x/H=2 the jet stream (upper half) was under predicted by the k-ε models while the k-ω SST model over predicted it. The Reynolds Stress Model (RSM) captured it best. Surprisingly RSM performed worst at the lower half of the channel.

Looking at position X/H=8, the k-ε Realizable model and RSM showed good agreement with the reattachment point. The k-ω SST model over predicted the reattachment point (see location x/H=10) and the k-ε Standard model under predicted it. In terms of consistency, the k-epsilon Realizable performed best overall.

Figure 3.7 shows the recirculation progress along the channel. It is interesting to see that all turbulence models under predicted K_V. This was mainly due to their lack of understanding of the shear layer were the Reynolds Stresses play a major role. The RANS models seemed to under predict the shear stress, as was mentioned often in the literature. Although under predicted by 30%, the k-epsilon Realizable was closest in determining maximum K_V.

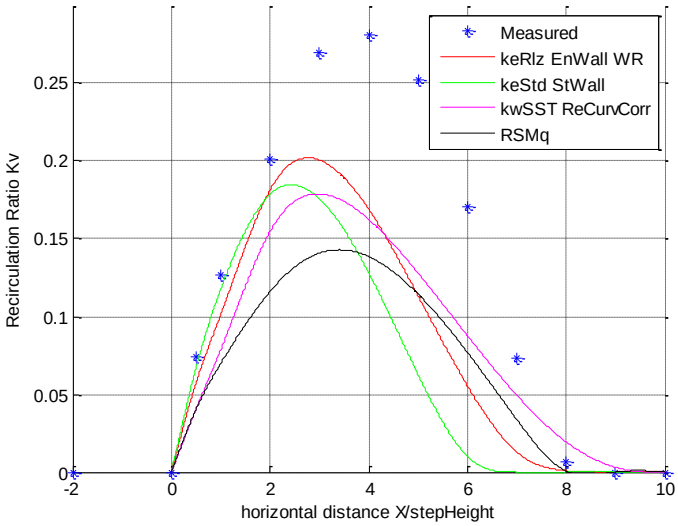

Figure 3.7 Progress of the Recirculation Ratio for case y15 along the longitudinal distance in the channel.

The k-ε Realizable model was also used to compare with other two experimental test cases m15 and o15 with relatively smaller channel-to-inlet area ratios of 1.48 and 2, respectively. The model performed remarkably better at these two cases (figure 3.8), showing an under prediction of K_V-max of approximately 20% for both. Looking at the trend of K_V-max for different channel-to-inlet area ratio in figure 3.9, the model followed the trend of the cases m15 and o15 almost perfectly and seemed linear when following the model. However case y15 was off trend. This suggested that either the relation of K_V with the channel-to-inlet area was non-linear or measurement errors might have been significant for case y15.

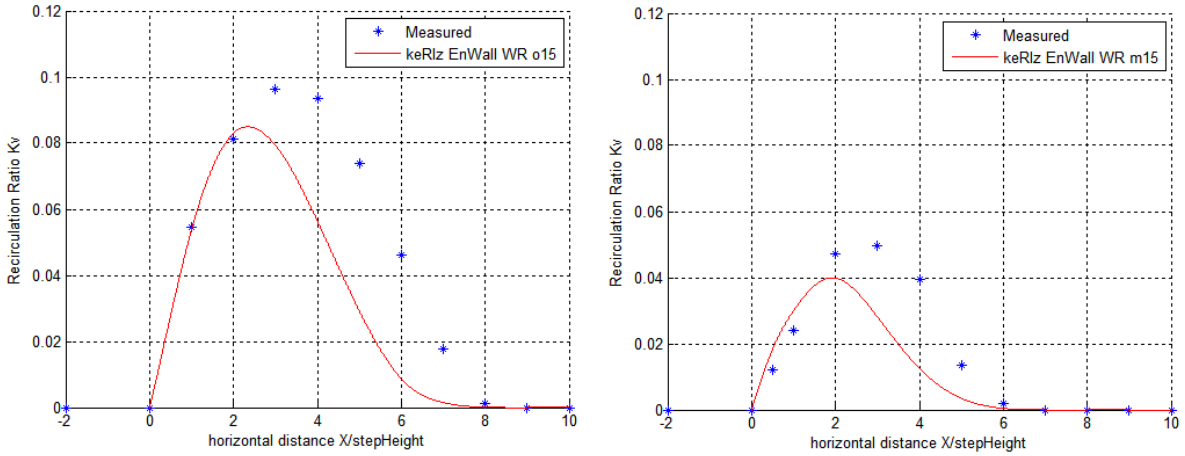

Figure 3.8 Progress of the Recirculation Ratio along the longitudinal distance in the channel for cases o15 (left) and m15 (right).

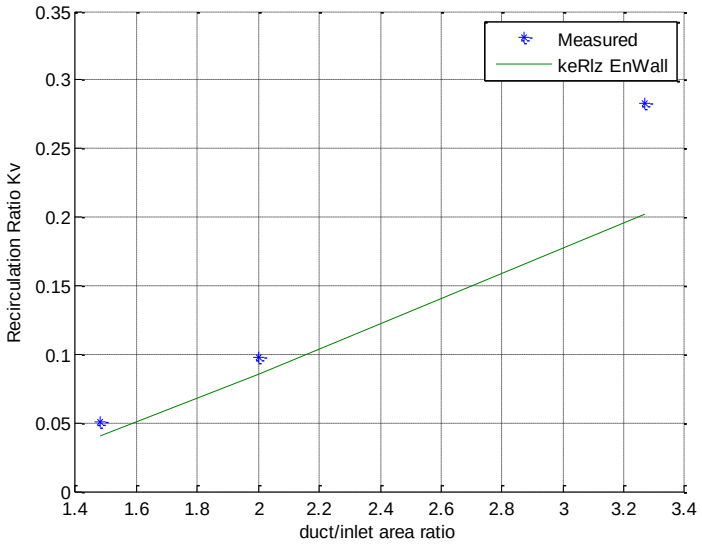

Figure 3.9 K_V trend for different duct/inlet area ratios. Measured K_V points were from the cases (left to right): m15, o15 and y15.

3.2.2 Large Eddy Simulation based models

3.2.2.1 Theoretical description

In the hope of gaining better results, simulations were also carried out with two variants of the LES model: the Detached Eddy Simulation model (DES) and the Embedded LES model (ELES). The problem arose when the model had to be generated in 3D. While the channel of the experiment only had a height of 36 mm, the width was 500 mm. This was deliberately done to minimize the effect of the sidewalls so that the flow would be almost completely 2D at mid-span. The much larger width would require an enormous amount of cells for a 3D model, especially with LES standards. The width was therefore cut to 50 mm (so that it

would stay larger than the largest 'eddy') and the periodic feature was applied to the side walls.

The grid cell resolutions were roughly three million for both the DES and ELES that did not require as many cells as LES, but this was still a bare minimum. E.g. the pure LES model requires about 10^3 as many cells as RANS-based models for wall bounded flows at high Reynolds numbers, which is around 60 million in this case.

The **DES model** is a hybrid RANS/LES model developed as a bridge to the industry where many high Re flow applications could be simulated with reasonable amount of CPU cost. The DES model switches between RANS mode and LES mode. The RANS mode is activated close to the wall boundaries whereas the LES mode covers the regions where large turbulent scales dominate. Due to this switch, the DES model is suitable in flows with high instability where large turbulent eddies are easily detected. For weakly unstable flows such as this experiment the DES may not switch to LES mode where it is required. One way to overcome this weakness was to refine the cells to the level applicable for the pure LES model, but that was the reason why the LES mode was avoided in the first place.
If the boundary layer would be larger than the cells adjacent to the wall, the DES limiter could activate the LES mode which is unsuitable to resolve typical RANS based high-aspect-ratio cells. The *delayed* option was activated (DDES) to ensure that entire boundary layer was covered by the RANS mode only. The k-ε Realizable model was chosen for the RANS mode.

The **ELES model** is not really a model but combines the RANS and LES models in such a way that rather than using a switch the mesh is separated in different zones by the user who can define in each zone whether the RANS or LES model should be activated. Between the zones should come interfaces where the outflow of the upstream zone is set as an inlet boundary for the downstream zone. This way the RANS and LES zones are clearly distinguished and ensures that the LES is activated where the user expects it should. This makes the model most suitable for weakly unstable flows.
Because the ELES mesh contains RANS zones, the user is enabled to coarsen the mesh in the RANS zones and refine the LES zones while maintaining roughly the same amount of cells in the complete mesh.
The LES zones may still contain boundary layers, which requires that the cells at the wall should not only be refined normal to the wall but also in parallel direction. This is one of the reasons why LES is nearly prohibitive for wall bounded flows. To overcome this limitation, the algebraic Wall Modelled LES model (WMLES) was chosen as a subgrid-scale model due to its ability to activate the RANS model in the inner layer of the boundary layer so that the wall adjacent cells my remain at their high aspect-ratio shape. The k-ε Realizable model had shown in Figure 3.10 to predict the boundary layer reasonably well. The WMLES model covered the outer layer of the boundary with a modified subgrid-scale formulation proposed by Shur et. al [34].

3.2.2.2 *Set-up*

For the DES model, the cells at the periodic plane were generated in a similar fashion as in figure 3.11. This 2D plane was copied along to span with the same global interval as in the 2D plane, by using the Cooper scheme, so that hexahedral cells were globally cube-shaped (except near the walls).

The mesh for the ELES model is shown in figure 3.12. Three zones were generated where the LES zone covers the entire recirculation zone from the point of detachment. The subsequent RANS zone starts at a distance of one step height behind the reattachment point. The LES zone was globally refined while the RANS zones were globally coarsened such that the total amount of cells were almost the same as for the DES case.

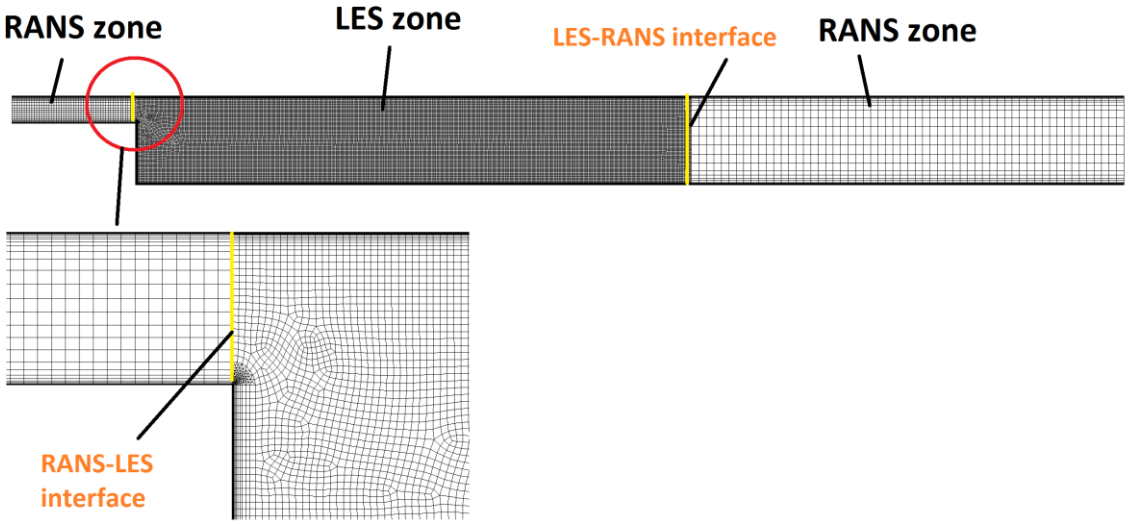

Figure 3.13 Side view of the mesh prepared for the ELES model

The spatial discretization schemes were the same as for the RANS models except that (eventually) the pressure was also interpolated with the 2nd order upwind scheme after it was discovered that the PRESTO scheme had the tendency to delay turbulent instability. Also artificial flow fluctuations were applied at the inlet boundary, or at the RANS-LES interface in case of ELES, using the Vortex Method in case of delayed instability was observed after the flow separation point.

The Bounded 2nd Order Implicit scheme was used for the time discretisation with a time-step size of 1x10^{-4} s and 25 iterations per time step. The calculations were first run with the RANS model until full convergence was obtained which was then set as a starting point for the transient calculations. The simulations continued several mean flow residence times until the velocities at certain points had marginally stabilized in the domain (an example is shown in figure 3.14). After this the data was gathered for time statistics after each time step, again for a period of several mean flow residence times.

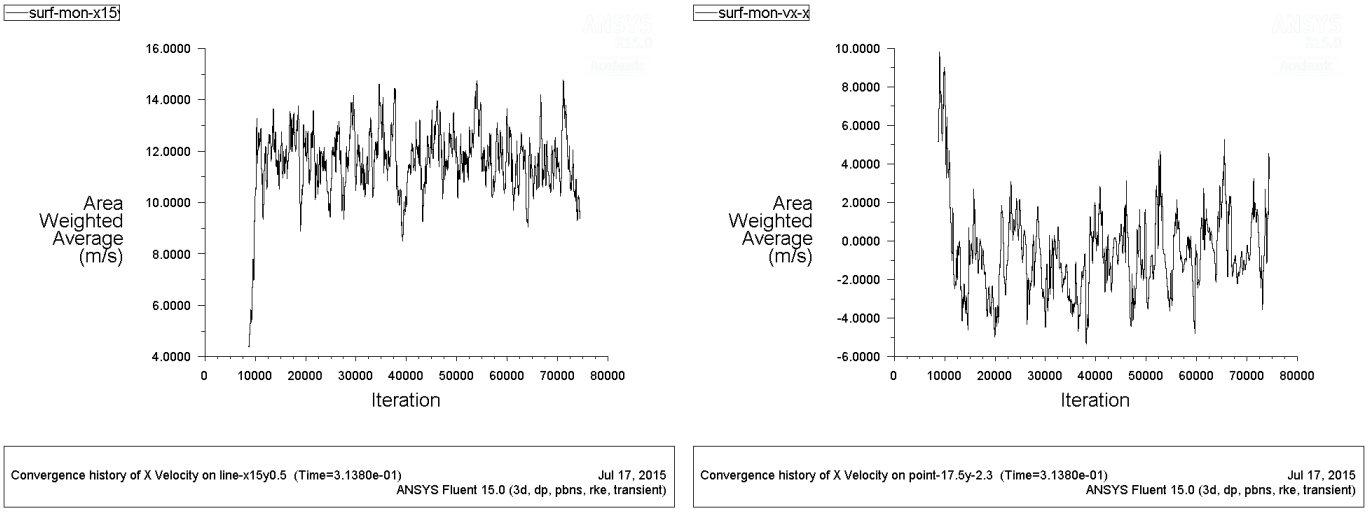

Figure 3.14 Two of several convergence history plots of the X velocity at two different points in the domain.

3.2.2.3 Results

Before starting to look at the results of the LES based models, it is worth to mention that the RANS model did not show any difference in the velocity profiles between the 2D and 3D grid. This was expected from symmetrical geometries where the 3D models are '2D shaped' and the inlet velocity is directed along the 2D plane which was explained in section 3.1.4. With 2D shaped geometries it is referred to any 3D body that can be made from a 2D plane either by translation in the direction normal to the plane or by a full rotation around the symmetry axis.

The mean x-velocity contour plots of the LES based models are shown in figure 3.15. It can easily be seen that the contour plot of the RANS simulation was closest to that of ELES with VM applied. The DES models clearly under predicted the reattachment distance. The models where the VM was not applied showed a nearly stagnated region at the upstream part of the wake. These observations are more clear when looking at the instantaneous x-velocity contour plots in figure 3.16. When VM was not applied, even for the ELES model the instabilities were not immediately detected, showing the weakness of the turbulent instability. This might be also due to the poor amount of cells for LES standards. Since the exchange of momentum started after the transition point this explained why the wake was stationary at the upstream part. Basically it behaved like a laminar separation bubble.
The DES model, even with VM applied still had a difficulty to detect instability although it did it better than without VM. Only the ELES model with VM could detect it from the separation point.
It is also noticeable that with the DES model the jet did not 'penetrate' far enough before significantly losing its momentum to the recirculation zone. The model had a difficult time in capturing the physics of these type of flows. This was also clear from the velocity profiles in Figure 3.17, though the DES model with VM performed surprisingly well at x/H distances 2 and 4. Looking at the K_V plots (figure 3.19), the DES model without VM seemed to predict the maximum K_V best though of course the plot did not represent the models performance as was seen in the velocity profiles.

The velocity plots of the ELES model with VM (figure 3.18) were comparable with the RANS model, however the shear layer was slightly better predicted. Without the VM, the ELES model showed good agreement only after x/H = 6.

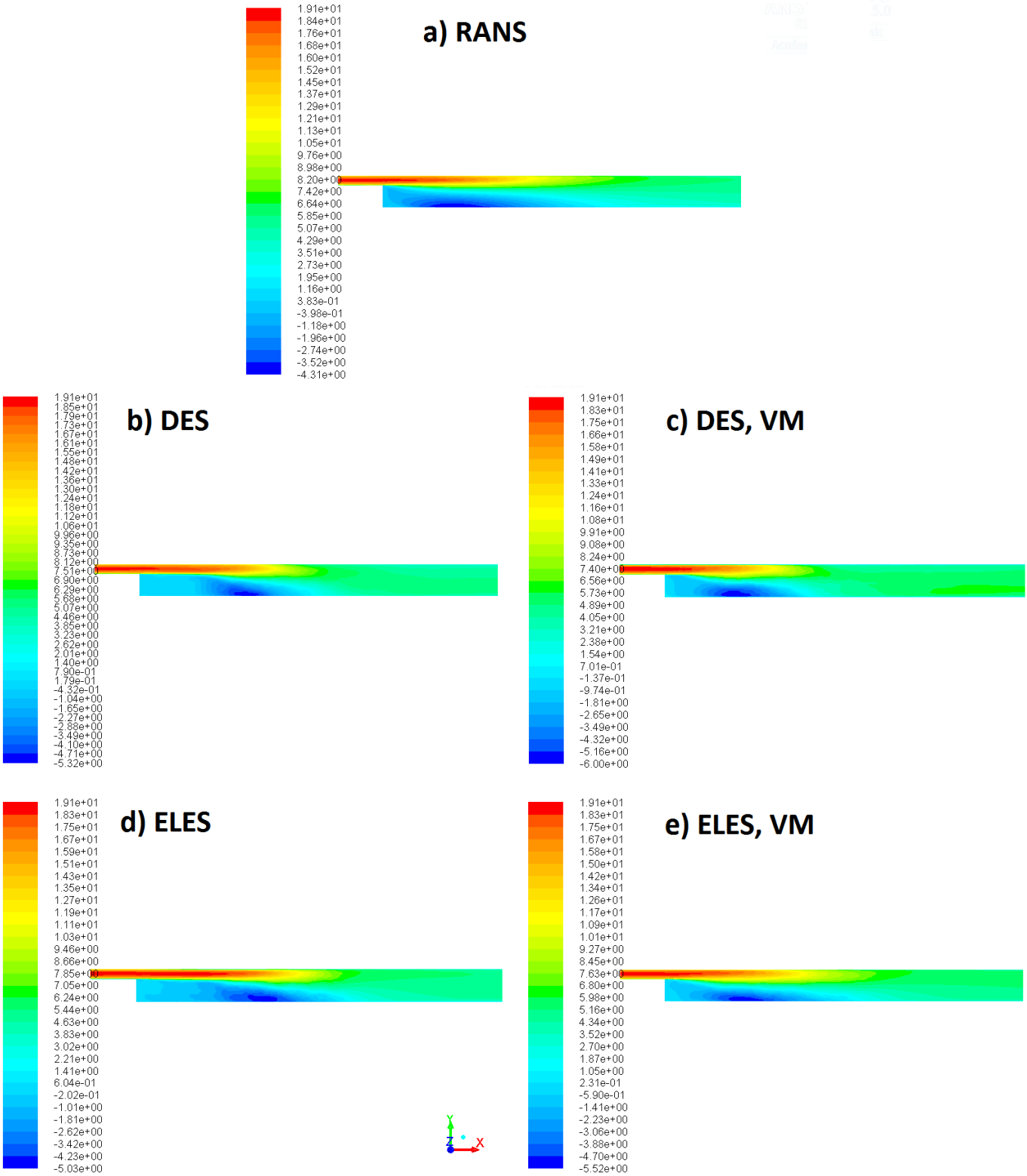

Figure 3.15 Contour plots of the mean X-velocity in m/s. VM is added to the models when the flow fluctuations were applied at the inlet using the Vortex Method.

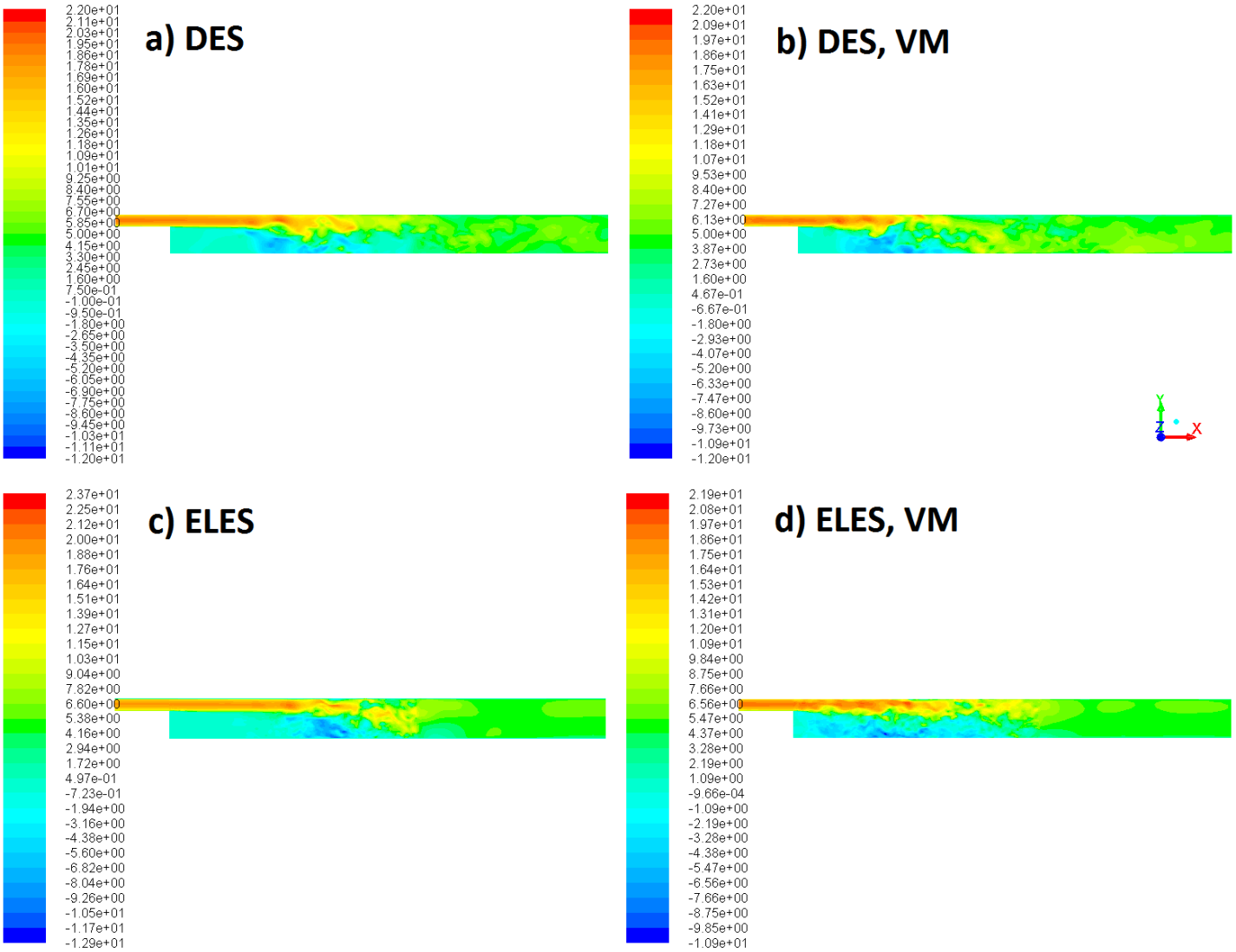

Figure 3.16 Contour plots of the instantaneous X-velocity in m/s. VM is added to the models when the flow fluctuations were applied at the inlet using the Vortex Method.

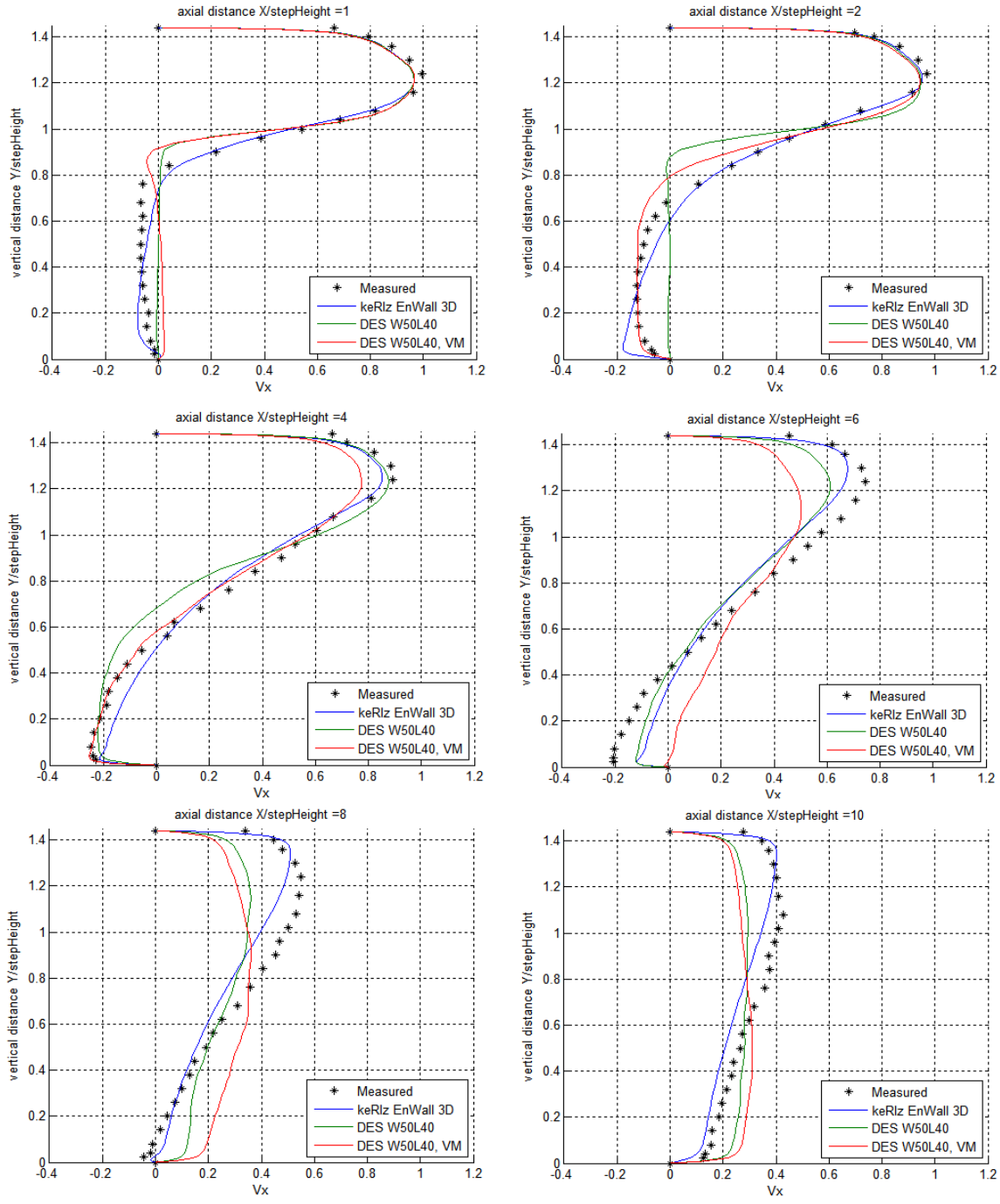

Figure 3.17 normalised x-velocity profiles of case y15 at increasing (normalised) x-positions, x/H. Re=15,000 ; measured reattachment length (normalised)=8.38 x_r/H; step height=25mm; channel height=36.025mm; reference velocity 19.14m/s. Modelled with RANS and DES.

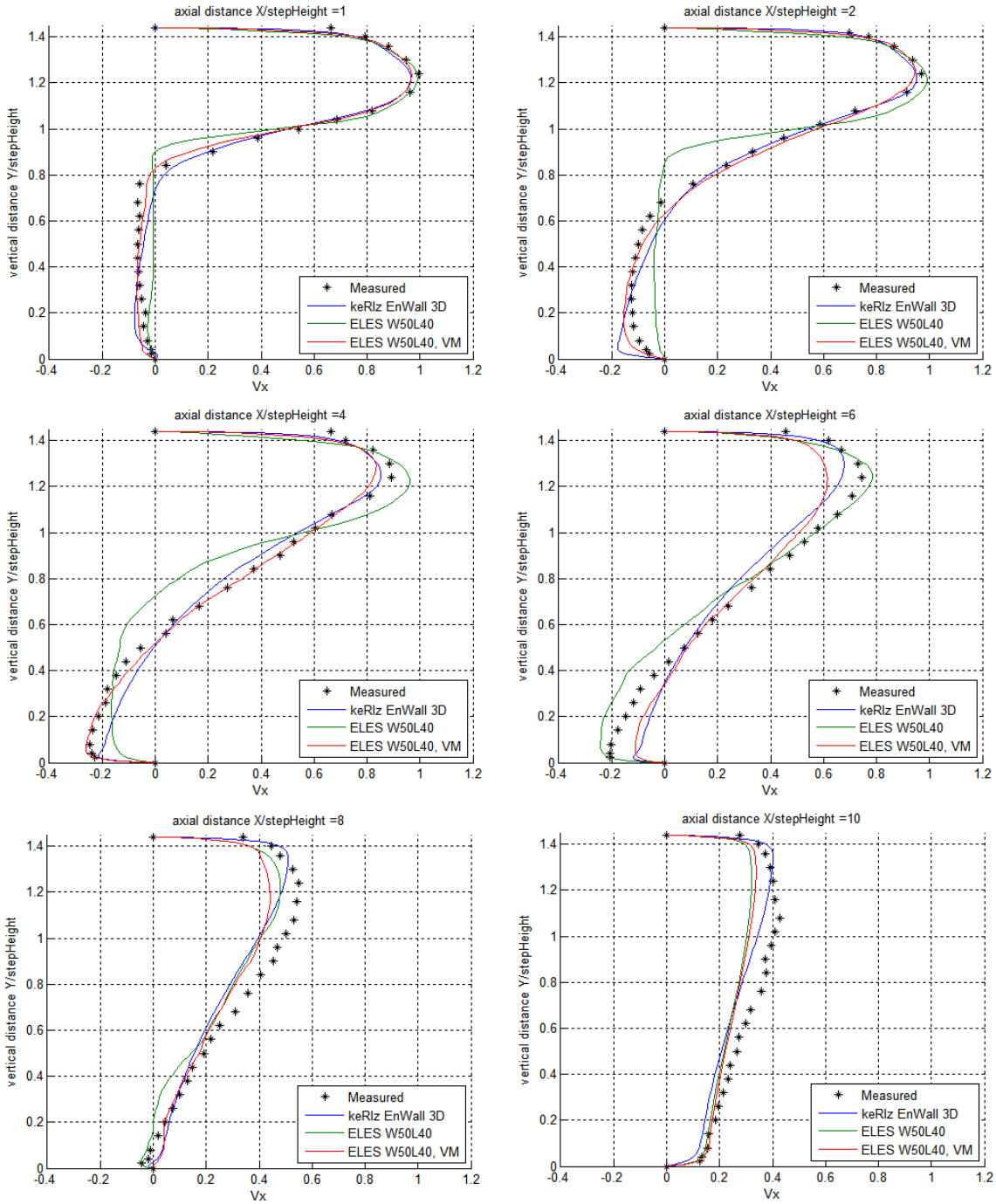

Figure 3.18 normalised x-velocity profiles of case y15 at increasing (normalised) x-positions, x/H. Re=15,000 ; measured reattachment length (normalised)=8.38 x_r/H; step height=25mm; channel height=36.025mm; reference velocity 19.14m/s. Modelled with RANS and ELES.

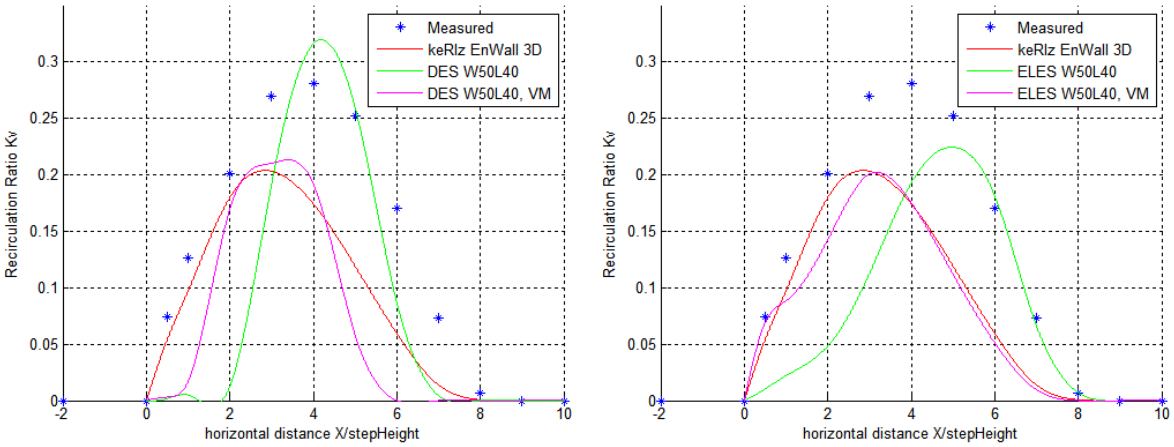

Figure 3.19 Progress of the Recirculation Ratio for case y15 along the longitudinal distance in the channel.

3.2.3 Final comment

The validation of the RANS models gave a some confidence to proceed with the design of the combustor. The LES-based models were not able to give better predictions. They have shown to be very stiff in the sense that the mesh geometry and boundary conditions should exactly match the experimental model and require very fine cell resolution. Even with an 8-core workstation having 8 GB of RAM in each core, it took about 2 weeks for each DES/ELES simulation to get a time averaged solution. A 2D RANS simulation only needed about a minute to converge on the 8-core workstation and to make things fair it needed 3 hours using the 3D LES mesh of which the grid size was already excessive for RANS models.

In practice however the ELES model is well known to predict flows over backward facing steps accurately. This suggested that either the grid resolution of three million should be increased, leading to longer runtime, or the periodic feature at the side walls were not suitable and the full geometry should be used. It became clear that it was unfeasible for a MSc. thesis to use the LES model as a tool to design a new concept. Especially when combustion models had to be added with detailed chemistry later on. It would however be more suitable to use it as a verification tool for the final design before validating it with experiments.

The recirculation ratio was an important parameter for FC and was under predicted by 20-30% with the RANS model. However, it did show a similar trend when the geometry varied, which was of high interest. Also the reattachment point was well predicted and aided in the prediction of the flow paths. To know how important the value of K_V was could only be found out when combustion was also modelled, which is a topic on chapter 4.

3.3 The initial concept

This section will guide the reader through the design decisions made based on the simulation results to obtain the first concept. First the effect of changing jet size and liner

height on the recirculation zone was analysed. Afterwards a cavity was added with the notion to 'trap' the vortex in hope of increasing the recirculation.

3.3.1 Confined jet in a straight channel

A selection of practical combinations of inlet size and liner height were modelled with a constant inlet velocity of 100 m/s. At the inlet boundary also an initial guess of 10% of the inlet size was given for the turbulent length scale and 5% for the turbulent intensity.

As was noticed with the validation model in section 3.2.1 the recirculation zone was highly influenced by the change in either the inlet size or liner height. These two geometrical changes were better defined as a ratio of cross-sectional areas of the liner (A) to the inlet (a). A clear proportional relation was obtained between the area ratio and K_V (figure 3.20) though it was expected that this relation would reach a limit as the jet cannot exchange its momentum with the recirculation zone infinitely. But for the relatively small aero engine combustor that point was irrelevant.

The trends of both the validation model with one recirculation zone and the planar confined jet model with two recirculation zones were almost the same ($K_V \propto 0.09\ A/a = 0.09\ H/i$), indicating that the position of the planer jet in the channel does not influence the total recirculation. For a cylindrical channel with a circular jet however the physics were different and the increment of K_V was less steep ($K_V \propto 0.04\ A/a = (H/i)^2$). But when comparing a planar model with a axisymmetric one with the same i and H the recirculation ratio is much larger (3.21b). This is because the area ratio in a cylinder is quadratic to H/i.

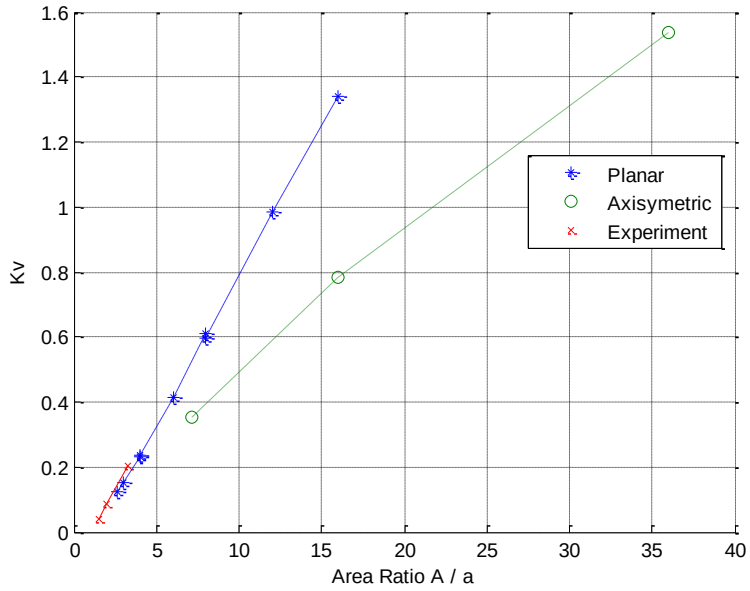

Figure 3.20 Relation between the recirculation ratio and the cross-sectional area ratio of the liner to inlet.

Figure 3.21a shows that when either *i* or *H* is kept constant and the other changed than the distance of the reattachment point increased further downstream with increased ratio.

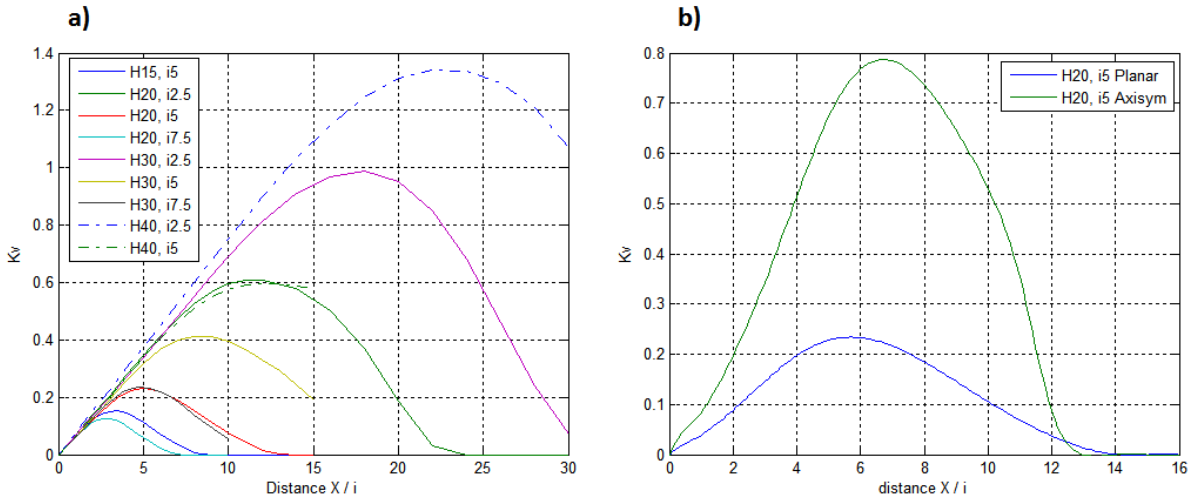

Figure 3.21 Progress of the recirculation ratio along the normalised X-distance. a) Comparison of only planar models with different inlet sizes and liner heights and b) comparison of a planar and a axisymmetric model with the same inlet size and liner height.

Since the liner height was limited to 0.3m and the inlet to 0.05m (in order to keep the inlet velocity at 100 m/s approximately) a recirculation ratio of only 0.4 could be achieved for the planar model, representing the ATC. If the inlet size was reduced to half its size, K_V would increase to 1, but this would also double inlet velocity. Nevertheless, K_V would still be much lower than required in the literature (minimum of 2-3). In case of a CTC, represented by the axisymmetric model, the recirculation ratio was already at 1.6 with the same *i* and *H* and therefore close to the minimum required K_V.

3.3.2 Cavity flows

This section will give a progression towards the concept. Introducing cavities in the combustor required a designation of new geometry variables that are shown in figure 3.22. It is recommended to refer back to this figure when the designations are unclear.

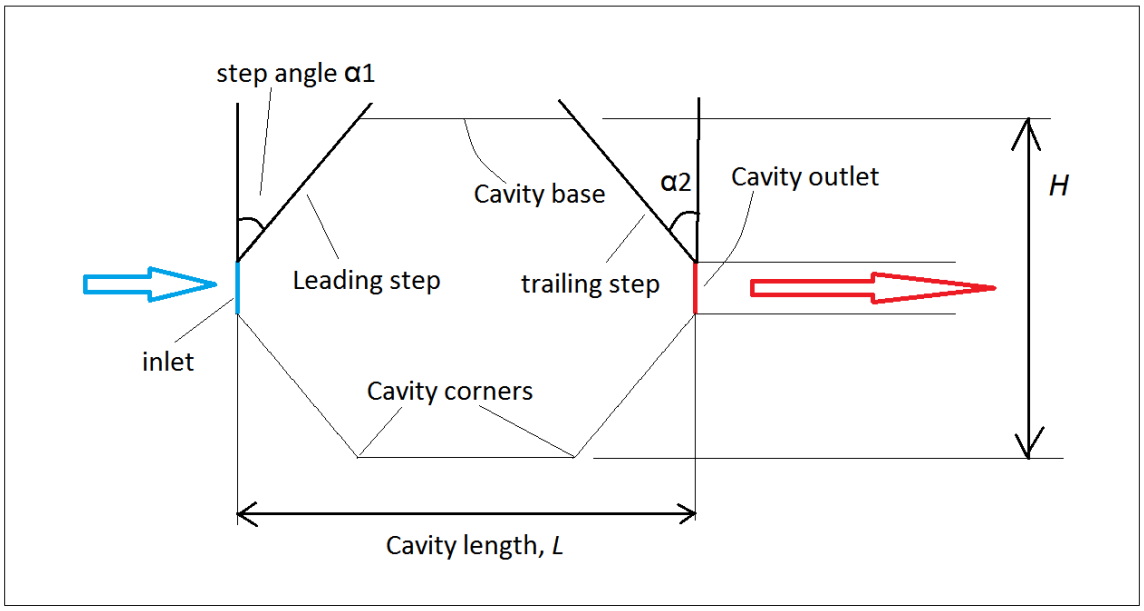

Figure 3.22 Geometry definitions of a combustor with cavity.

3.3.2.1 *Effect of cavity length and cavity outlet size*

Before the cavity was refined, its length *L* was determined. A standard rectangular cavity was added to the channel starting from *L*=0.5m, with the same outlet size (*o*) as the inlet. This increased K_V in nearly 30% (figure 3.23). At 0.3m length K_V decreased again. It was chosen to go for 0.4m instead of 0.5m with the argument that the increased residence time would enhance NO_X formation. Nevertheless, this was just a guess of how the emissions would be affected, and at this stage nothing was certain.

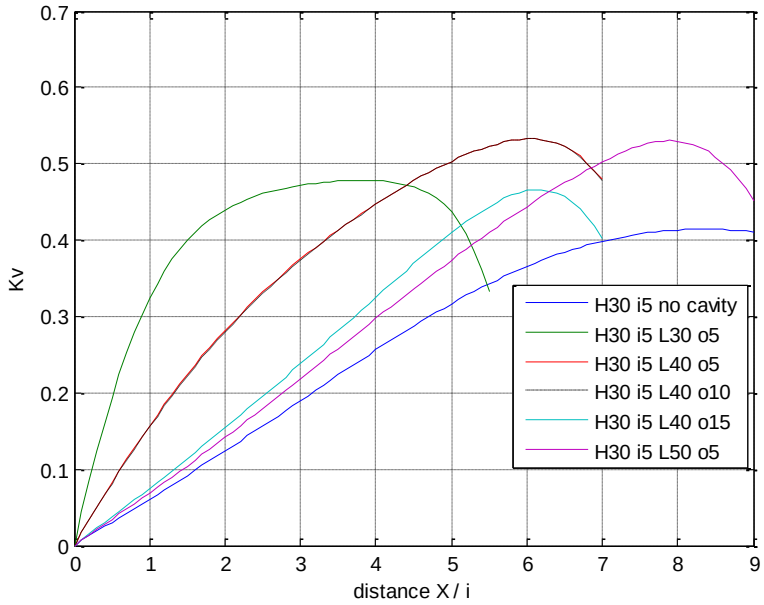

Figure 3.23 K_V progression with rectangular cavities varying in length *L* and outlet size *o* (indicated in cm).

It can be noticed in figure 3.23 that when the outlet size increased to o = 0.1m the K_V-progression stayed exactly the same as with o = 0.05m but when expanded even further to o=0.15m, K_V reduced. The streamlines showed that the vortex remained 'trapped' up to o= 0.1m (Figure 3.24). The blockage by the trailing step caused the vortex to accelerate downstream which led to the increase of K_V. At further outlet expansion the jet stream detached from the outlet corner and the vortex expanded, which led to a slight loss in its vortex strength.

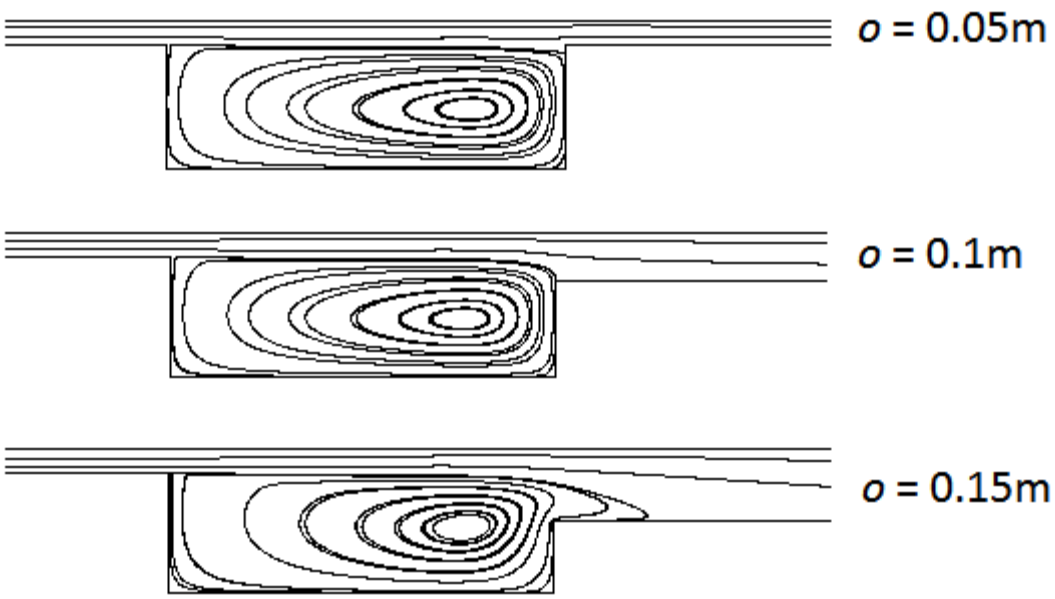

Figure 3.24 Streamline pattern at changing outlet size o. L=0.4m, i =0.05m and H=0.3m.

3.3.2.2 *Refining the cavity shape*

The increased K_V due to the rectangular cavity came with a price. Additional pressure losses occurred due to the secondary vortices at the cavity corners and the possible flow separation at the sharp cavity outlet corner.

Pressure loss is of primary importance in a GTE as it impacts on the engines performance negatively. However some amount of pressure loss in the combustor is necessary because the turbine cooling air coming from the compressor will also suffer from a pressure drop in its path to the turbine. In order for the cooling air to flow outside and around the turbine vane, it needs to overcome the combustor outlet pressure [1]. Unless pumps are installed for the cooling air, a pressure loss of around 3-4% is required in the combustor. As combustion will inheritably experience a pressure drop it is therefore important to minimize it already with the cold flow design.

There were several ways in modifying the cavity's geometry:

- Rounding of the cavity corners with radius *R* to remove the secondary vortices.
- Inclining the cavity steps to reduce the corner 'sharpness' at the cavity outlet in order to lower the risk of flow separation and to put the cavity better in line with the elliptical recirculation zone.
- A combination of both.

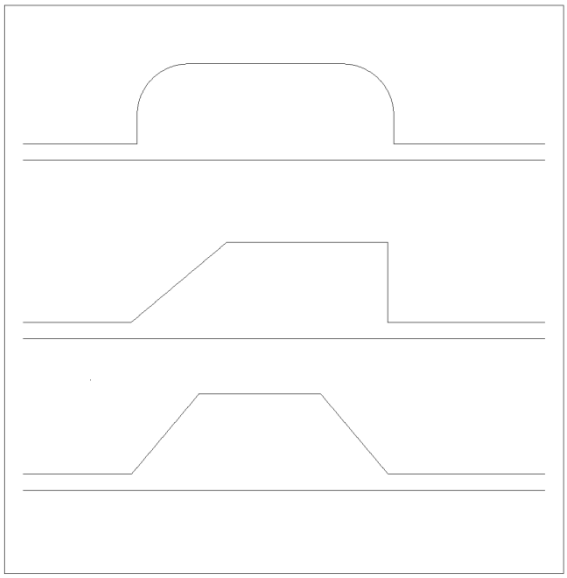

Figure 3.25 Cavity modifications

The results are shown in Figure 3.26. The removal of the secondary vortices with the rounded off corners has led to a slight increase in $K_{V\text{-max}}$. Once the vortices were removed, $K_{V\text{-max}}$ was practically insensitive to the corner radii (figure 3.26 a). The momentum of the recirculated flow however increased more significantly upstream with increased radii making it less prone to separation, hence increased stability. The inclining of the leading step had almost a negligible effect on $K_{V\text{-max}}$ but an increase in trailing step angle clearly reduced it and shifted the vortex core upstream. Also the structure of the vortex was relieved by the inclined trailing step changing the vortex back to its more natural elliptical shape which may have caused the reduction of $K_{V\text{-}max}$ (see figure 3.27).

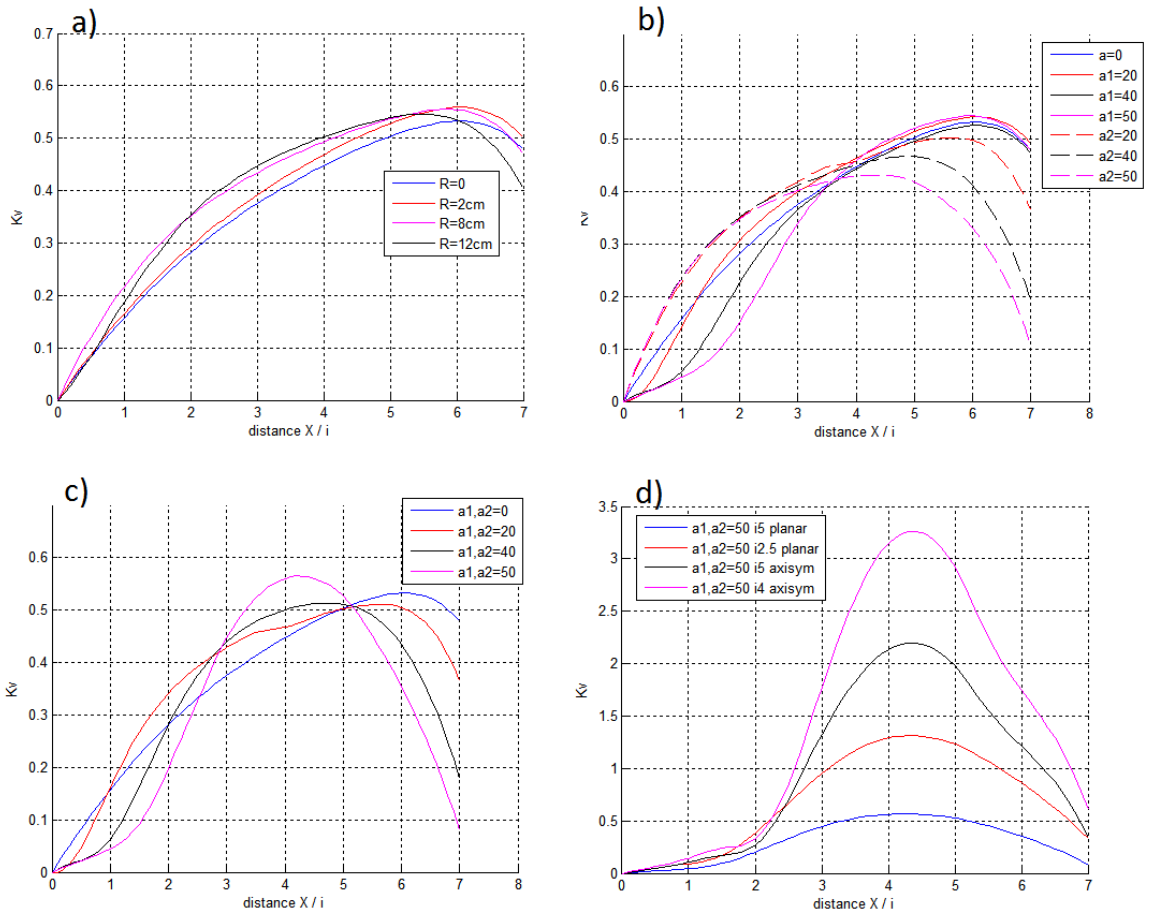

Figure 3.26 K_V progression along the cavity with varying step angles and corner radii.

The inclining of both steps together had a less clear effect on $K_{V\text{-}max}$. It first reduced with increased step angles by relieving the vortex and shifting it towards the centre of the cavity and suddenly increased again at angles of 50^o . From the streamline patterns can be seen that at 50^o the vortex was getting a more circular. When the step angles increased further to 58^o , so that the steps met each other forming a triangular cavity, it led to a drop of K_V to the level as if there was no cavity at all. This made sense since this shape was closer to a normal channel flow with backward facing step than a cavity (Figure 3.27). The streamline patterns show that the circulation depended on the vortex structure.

The concluding remark however is that the geometry modifications of the cavity had a negligible effect on $K_{V\text{-}max}$ and that the main source of influence remained the liner to inlet area ratio (figure 3.26 d). Though the 30% increase of $K_{V\text{-}max}$ with the cavity alone also deserved credit and was taken into the design, but only if inclining the trailing step alone was avoided. For the ATC $K_{V\text{-}max}$ could reach a value of 1.3 in the cold flow but with a CTC it has already passed the minimum value of 2, and even 3 when reducing the inlet area by half.

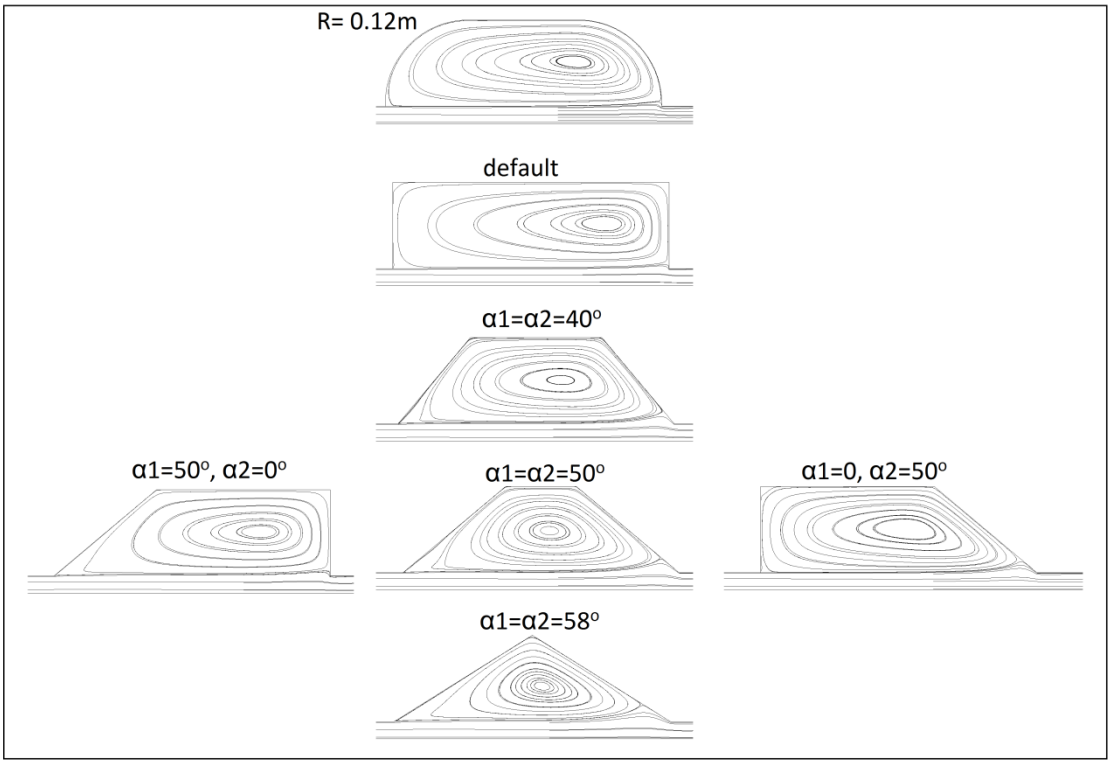

Figure 3.27 Streamline patterns of the planar cavity flow with geometry modifications.

The decision of which geometry would make the concept was based on the minimum pressure loss. Figure 3.28 shows that when the secondary vortices were removed with rounded off corners the pressure drop reduced with 0.2% regardless of the radius of the corners. However when the sharpness of the cavity outlet corner was reduced by increasing the step angles (hence reduced flow separation) the pressure dropped proportionally.
Combining both features has led to a concept with both cavity steps inclined at 50° and fillets at the cavity corners with R=0.02m. This reduced the pressure drop to about 1.8%.

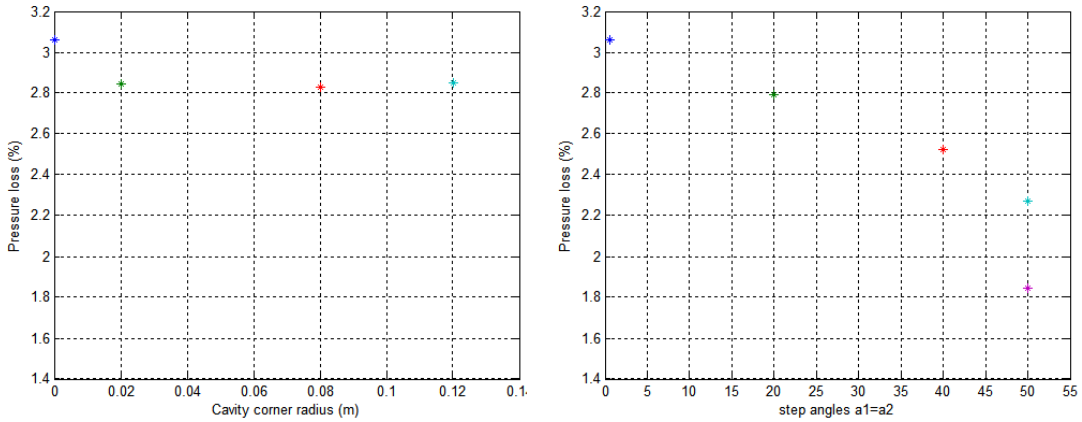

Figure 3.28 Pressure losses of different cavity geometries with *L*=0.4m, *i*=0.05m and *H*=0.3m.

4

Reacting Flow Simulation

After the basic combustor geometry was generated with the cold flow simulations it was time to apply combustion to it and study the behaviour of the reacting flow at conditions similar to that of an aircraft at the flight stages Take-Off and Cruise. This required first to set the right boundary conditions and to decide which models to use.

The simulations and design improvements were conducted in an iterative approach. The result of each simulation was studied and used for the refining of the combustor, e.g. by changing its geometry and repositioning the fuel inlet. The design alterations were carried out roughly and were based on educated guesses and understandings from the results. This continued until pollutant formation was minimized. Also the effect of inlet parameters such as temperature, and fuel-to-air equivalence ratio was investigated.

4.1 Methodology

4.1.1 Boundary conditions

Achieving the appropriate conditions for a FC chamber as was given in the literature is challenging for an aero engine. Nearly all modern aircrafts make use of an ATC which was shown in the previous to chapter to achieve a recirculation ratio up to ±1.3, though it should not be forgotten that it was under predicted by the models. The other challenge is to achieve inlet temperatures above auto-ignition. Though 822 K (table 3.1) exceeds the auto-ignition temperature of methane with stagnant and undiluted air, it would be much more difficult to react with diluted air at high velocities. Higher temperatures might be necessary but that would require much higher compression ratios. To achieve an inlet temperature of 1000 K would it would require a compression ratio of at least 80:1, which is double the compression of the current state-of-the-art. Another way would be to use the heat of the turbine outlet to increase the combustor inlet temperature with a heat exchanger, but would come with the penalty of added weight, complexity and significant pressure losses.

A more promising solution is to reheat the hot exhaust of a previous combustor, creating an environment much more suitable for FC. Such a type of combustion system is called sequential combustion and was applied to the commercially successful industrial GTE, the Alstom GT26. The second combustor was not designed for FC, though it is able to achieve NO_X emissions of 15 vppm at 15% O2 dry [35]. This architecture was never installed in aero engines.
The AHEAD project, which is a collaboration of the faculty of Aerospace Engineering at TU Delft and other institutions, has developed an engine concept that does make use of sequential combustion called a dual hybrid combustion system (see figure 4.1). In this engine the second combustor, designed for FC, reheats the hot and oxygen poor (vitiated) gas coming from the liquid H_2 combustor after energy is extracted by the high pressure turbine. The configuration is different from the one designed in this thesis but the scenario was also used as a boundary condition.

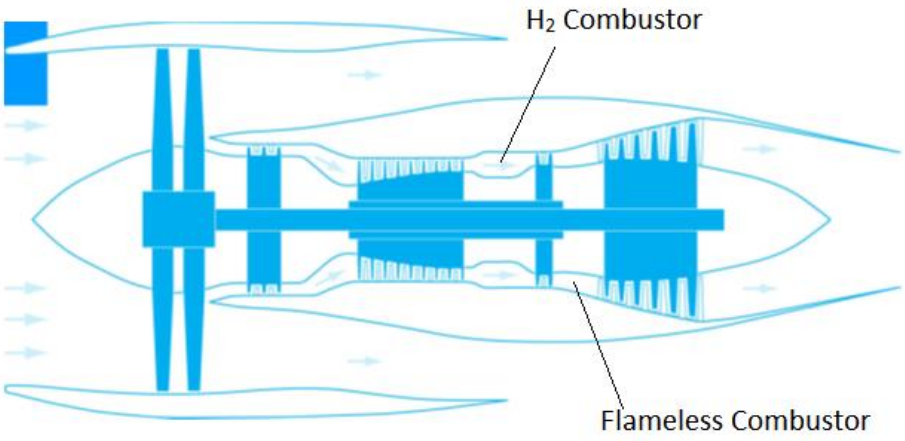

Figure 4.1 Schematic of the hybrid engine developed by AHEAD [36].

Lastly, aero engines operate at very high pressures which may vary quickly depending on the operating condition. To remove this influence and isolate only on the equivalence ratio and temperature, the pressure was kept constant at atmospheric conditions. As this is a completely new design, the atmospheric pressure condition was also chosen because of validation purposes allowing to use the simulated data to compare with experiments. However this required a correction of the mass flow rate to atmospheric pressure so that the air inlet velocity remained the same as with elevated pressures.

4.1.2 Combustion modelling set-up and convergence

As the calculations were limited to steady-state and the geometry simplified to 2D, more CPU power was reserved for the combustion model Eddy Dissipation Concept with detailed chemistry, which was encouraged from the discussion in section 2. The chosen fuel was methane because its reaction mechanism is relatively well understood and the amount of reactions is smaller than that of its larger relatives. However, the full GRI 3.0 mechanism still

led to very long runtimes (approx. 2 days for each case) which was not feasible to use it for refining and testing the combustor in the remaining months. Instead the reduced GRI mechanism named drm19 was used which was developed to closely reproduce the main combustion characteristics predicted by the full mechanism but with the smallest (still detailed) set of reactions [37]. The full mechanism was still used as a verification tool nevertheless. The drm19 mechanism contained 19 species and 84 reactions but did not include NO_X reactions.

Since the formation rate of NO_X is (much) slower than the fuel oxidation rate, the majority of NO_X is formed after complete combustion, negligibly altering the flow fields, and can often be decoupled from the main combustion reaction mechanism.
The Fluent built-in post-processor was enabled to predict NO_X formation and consumption ('reburning'), by using the local fractions of OH, O and fuel radicals that were calculated by the EDC model. The specie's formation paths that were selected for prediction were thermal NO, prompt NO and NO via the N_2O intermediate. Especially the intermediate N_2O was important to add as this caused 25-50% of the total NO formation in the simulations. Temperature and composition fluctuations due to turbulence were incorporated by modelling the turbulence-chemistry interaction using the β-pdf approach, where the temperature variance is calculated with the Transported algorithm.

Though the liner walls were chosen to be adiabatic, radiative heat transfer was also included in the simulations by enabling the Discrete Ordinates radiation model.

Due to the high grid resolution and high quality cells (± 70,000 cells) no convergence related problems were encountered. The largest residuals errors were usually in the order of 1e-4 to 1e-3 (example shown in figure 4.2). In the majority of the cases, the most stiff equations were the species equations of certain fuel intermediates such as C_2H_5 and CH_3O. Also velocities at two random points, the outlet temperature and outlet CO concentration were used as convergence criteria. Using the 8-core x 8 GB RAM workstation, the average runtime for the EDC model with drm19 mechanism to reach full convergence was approximately 6 hours while the NO_X postprocessor took nearly 12 hours to converge. Sometimes when high inlet velocities and counter-flow was observed near the inlet, the secondary upwind scheme of the pressure interpolation led to difficulties in convergence. This issue was settled when using the PRESTO scheme instead. The simulations were also tested for grid independence, shown in table 4.1. Although the results were all in the same order of magnitude, it was chosen to go for the level of 69,763 instead 24,702 cells which deviated too much in temperature.

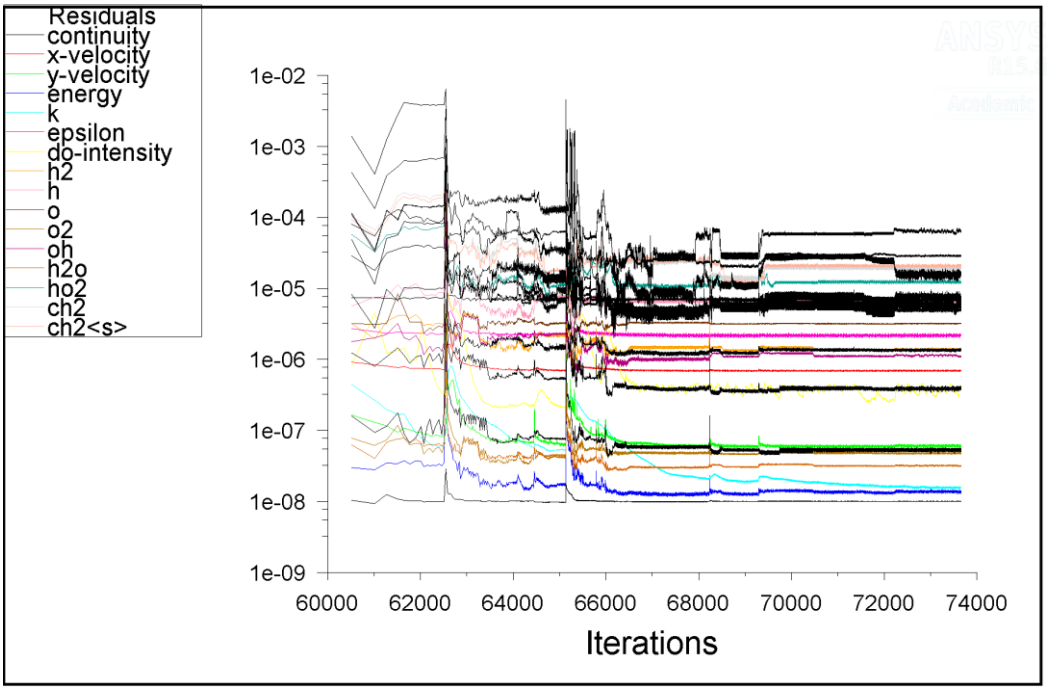

Figure 4.2 An example history plot of the scaled residuals

Table 4.1 Some output values with increasing grid size.

Case	*Cells*	T_i	T_{HG}	*CO [ppm]*	NO_X *[ppm]*
13a	24,702	1000	1721	2362	23
13a	69,763	1000	1697	2335	26
13a	130,697	1000	1687	2334	27
13a	258,548	1000	1694	2319	18.5

4.2 Can(nular) Type Combustor

Though still found in older aircrafts, CTCs are hardly used in modern aero engines. But due to its ability of achieving high K_V it was the first candidate to test the geometry. The initial reference condition was adopted from the CF5-80C2 engine. The highest Turbine Inlet Temperatures (TIT) are achieved at take-off. Most modern engines are able to reach temperatures of about 1600 K and to achieve that an overall equivalence ratio of about 0.3 is required with an inlet temperature of 1000K. However, part of the gas will flow around the liner and is not part in the combustion process. This would lead to average temperatures higher than 1600 K inside the liner. By partitioning the primary and secondary air in respectively 80% and 20% would lead to an average Hot Gas Temperature (T_{HG}) of ±1750 K which is a fair limit to avoid excessive thermal NO formation. Also the inlet velocity would reduce due to partitioning, which is beneficial. Using these estimations and a correction of the mass flow rate for the pressure, the following inlet conditions were obtained of one CTC for the first three cases (table 4.2). The mass flow rate was also reduced in such a way that the inlet speed in the CTC would be the same as the reference combustor which was an ATC. Once corrected, it remained fixed for all CTC cases. The vitiated air was assumed to be the gas product from hydrogen combustion at an equivalence ratio of 0.3. The calculated properties of this gas is summarized in table 4.3.

Table 4.2 Inlet boundary conditions for the first cases of one CTC with the initial concept.

Case	***$\dot{m}$ [kg/s]***	***Equivalence ratio***	***$\dot{m}_f$ [kg/s]***	***p[bar]***	***T_i [K]***	***U_i [m/s]****	***Inlet air state***
Reference	130	0.3	2.33	29.44	800	84.9	Dry
11	***0.0736***	0.3	0.0016	***1.01325***	800	84.9	Dry
12	0.0736	0.3	0.0016	1.01325	***1000***	106.2	Dry
13	0.0736	0.54	0.0016	1.01325	1000	112.3	***Vitiated***

*U_i is the result of the other inlet boundary inputs. The bold printed parameters are what caused the difference with the previous case.

Table 4.3 Simplified gas properties of the exhaust of H_2 combustion at equivalence ratio of 0.3, compared with air. Including species molar fraction, gas constant and stoichiometric ratio.

Gas	***C_{O2}***	***C_{N2}***	***C_{CO2}***	***C_{H2O}***	***Specific gas constant [J/kg/K]***	***Stoichiometric ratio***
Air	0.21	0.79	0	0	287	17.39
H_2 combustion exhaust	0.1366	0.7464	0	0.117	303.6	25.06

4.2.1 First results

For the first three cases (11-13) the fuel was injected in the middle of the cavity base of the initial concept, at an angle of 45^o which was almost aligned with the flow. In figure 4.3 it can be seen that when combustion occurred the cavity flow structure remained the same to a large extent. The main difference was that due to the expansion the flow accelerated after the cavity. Also the circulation of the cavity vortex increased. However the heat of combustion in the cavity led to a drastic decrease in density, thereby reducing the recirculation ratio nearly to half and barely exceeding the value 1 as shown in figure 4.4. The dimple seen in the graph of the reacting case showed the disturbance caused by the fuel stream.

Some of the important values predicted at the outlet are provided in table 4.4. The pressure drop increased by less than a half percent to a maximum of 2.4% compared with the cold model in all three cases. Also extremely low UHCs were emitted. The increase of inlet temperature led to very high NO_X emissions in case 12. Most of it did not form at the hottest region but in the flame region. By using diluted air the maximum temperature was the lowest of the cases, with the least intense flame (figure 4.5) and the NO_X emission dropped dramatically. These were common features of FC, however the OH contour plot did not show the diffusive nature of FC.

The most remarkable observation are the extremely high CO emissions in all cases. The reason can be explained by looking at figure 4.6. The oxygen was nearly completely

consumed in the cavity, explaining why the reaction zone was formed as such. The lack of oxygen left a very fuel-rich mixture in the cavity with unburned fuel radicals that did not react until they were entrained by the primary air flow and leaving the combustor at very high speed. The fuel-rich combustion caused large CO formation in the cavity and mainly continued oxidising at the fuel-lean side of the flame and after leaving the cavity. CO showed here to highly depend on temperature and concentrations of OH and O_2.

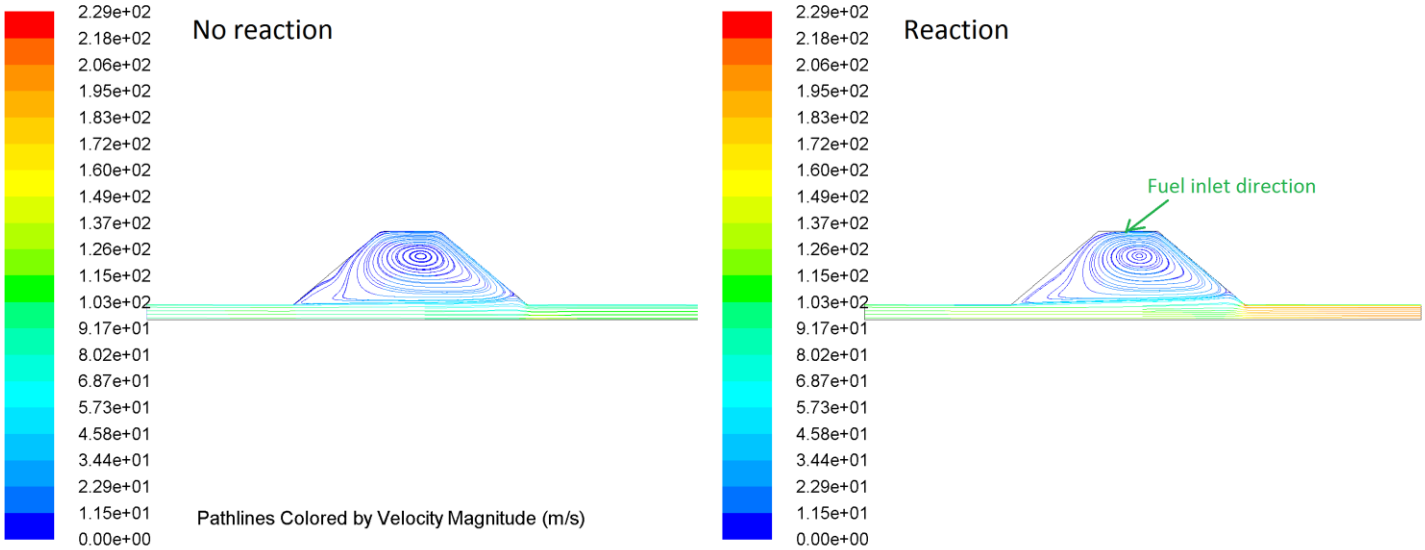

Figure 4.3 Streamline patterns colored by velocity for case 11 with and without reaction.

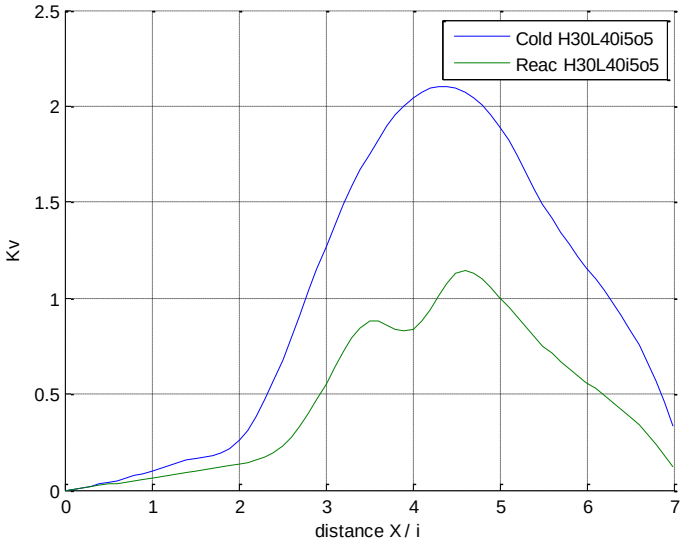

Figure 4.4 K_V progress for case 11 with and without reaction.

Table 4.4 Some of the important quantities predicted at the outlet.

Case	*T_i [K]*	*T_{HG} [K]*	*TIT [K]*	*T_{max} [K]*	*CO [ppm]*	*NO_X [ppm]*	*UHC [ppm]*	*dp/p*
11	800	1591	1432.8	2305	2767	104	1.073	0.020
12	1000	1744	1595.2	2448	1985	774	0.023	0.023
13	1000	1697	1557.6	2084	2335	26	0.002	0.024

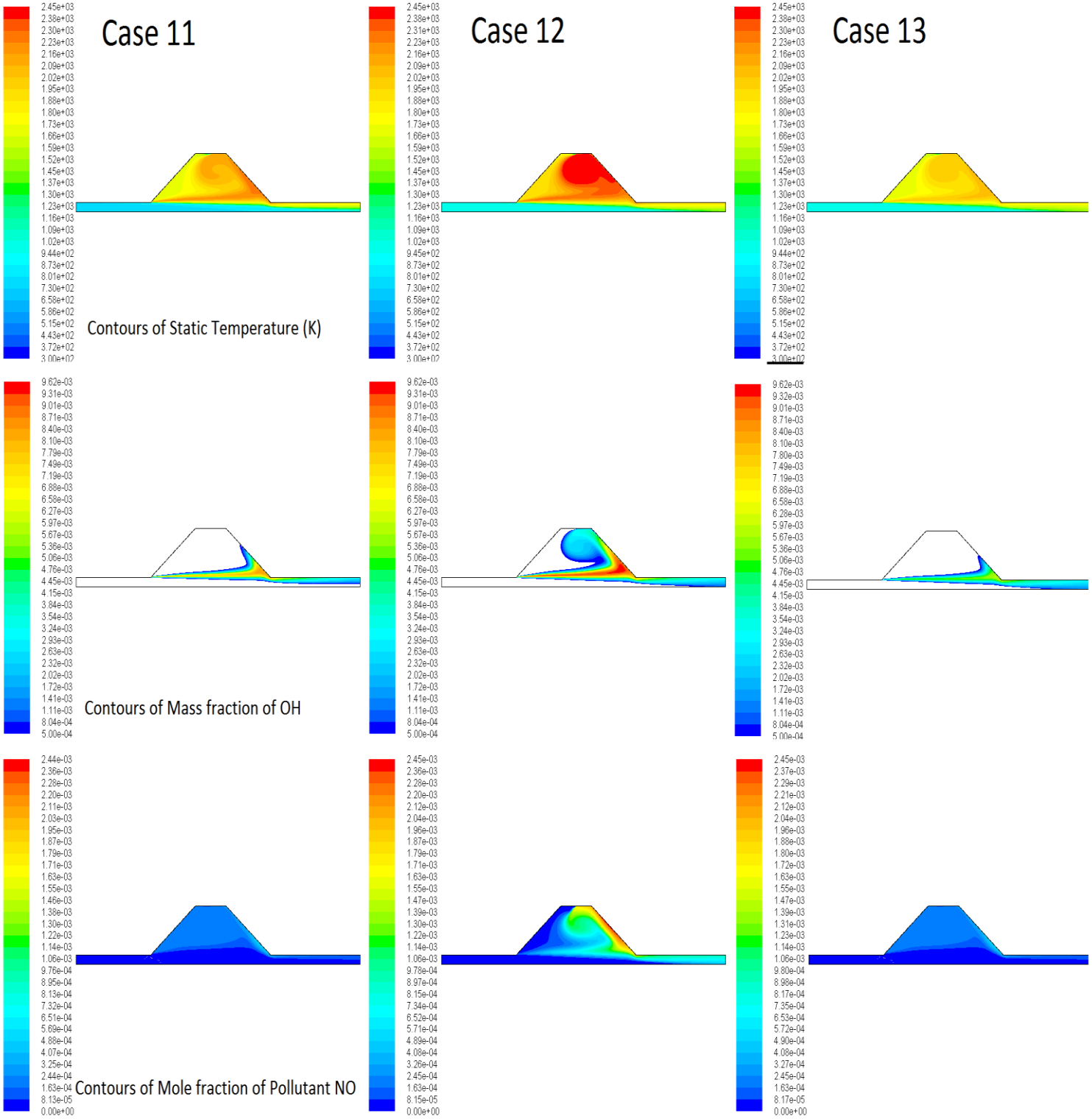

Figure 4.5 Contour plots of temperature(top), OH mass fraction (centre) and NO_X molar fraction (bottom) for the cases 11, 12 and 13 (geometry is off scale).

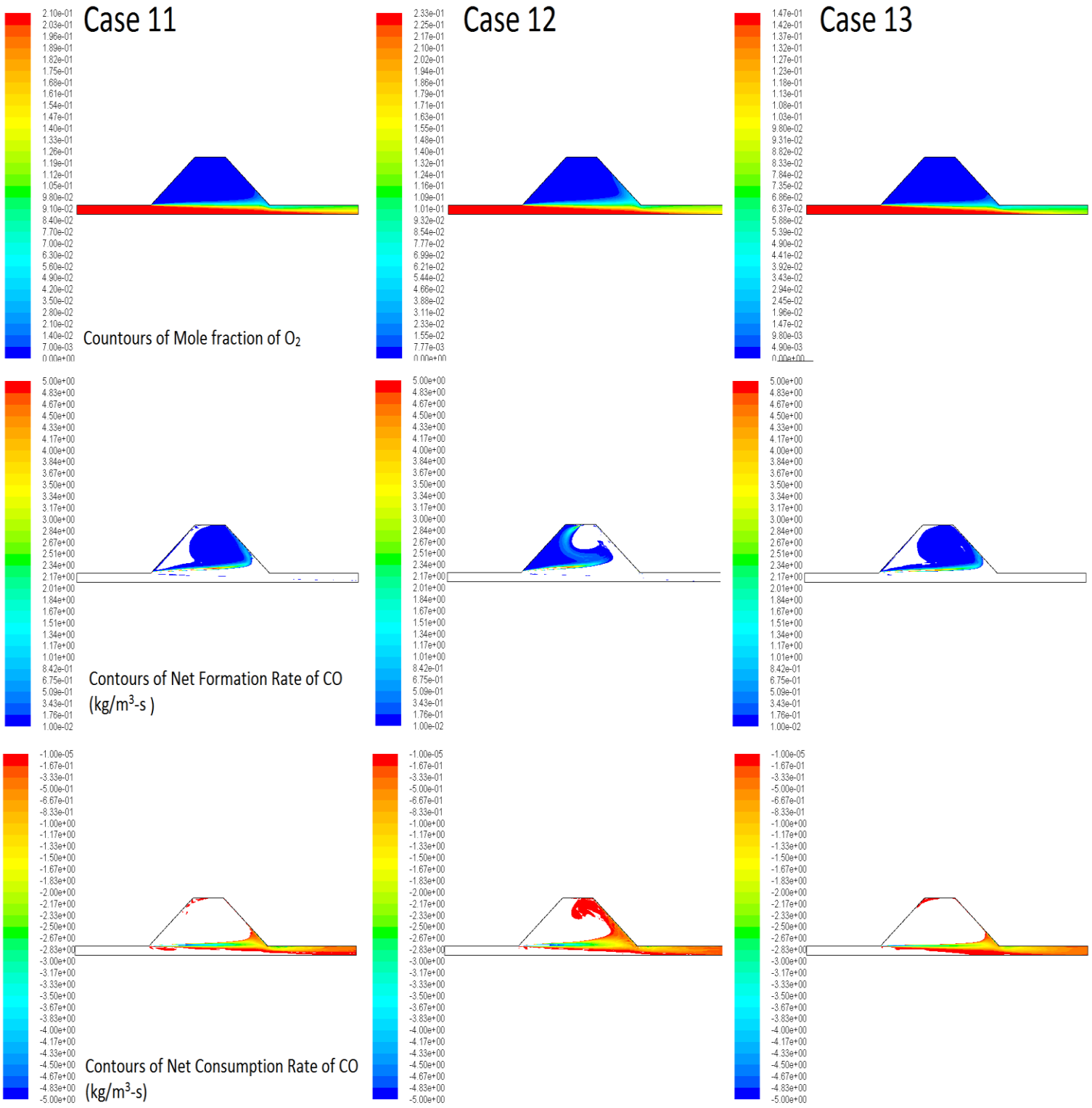

Figure 4.6 Contour plots of O_2 mole fraction(top), CO formation rate (centre) and CO consumption rate (bottom) for the cases 11, 12 and 13 (geometry is off scale).

4.2.2 Design modifications

Based from the observations in the previous section, the concept was modified several times in order to adapt to the shortcomings, especially to the high CO emissions. The effect of each geometry modification was first isolated and eventually all the modifications which were favourable (or showed reasonable compromises) were combined.
The history of the design alterations, including results are summarised in Appendix B. The guideline was first to inject the secondary air in the cavity, of which its original purpose was to extract heat only by means of convection and to enter the dome after the cavity in order to cool the hot gas before it would reach the turbine.
Secondly the fuel inlet was shifted rearward and the outlet size was expanded, both to increase the residence time. The final model of the CTC is shown in figure 4.7. The fuel entered parallel to the cavity surface in order to not to disturb the recirculation zone. The secondary flow was divided in two parts. The first part entered with the fuel to provide enough air for CO to oxidise. The other half was placed at the end of the cavity in order to also protect the liner as that part came directly into contact with the flame.

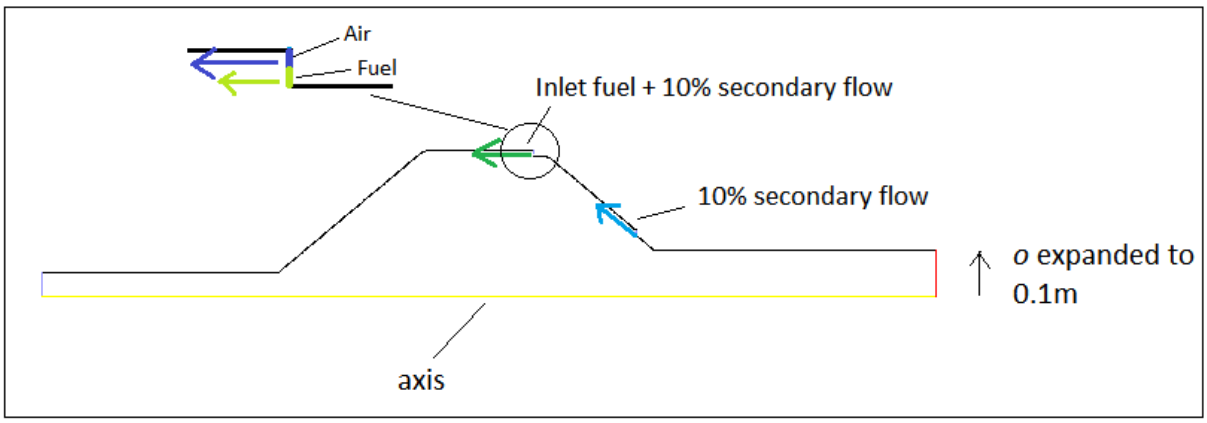

Figure 4.7 Final model for the CTC

The main input and output data are shown in table 4.5. The CO emission was reduced by a factor of 4 compared to case 12 with the initial concept and the NO_X emissions reduced by a factor of 2. The same held for case 13 with regard to CO but the NO_X emissions were compromised and have more than doubled. However this high equivalence ratio was unpractical as use was made from the H_2 combustion exhaust already operating at equivalence ratio of 0.3, which meant double the normal amount of fuel consumption at take-off. In the AHEAD project the equivalence ratio was 0.14 at take-off. Using this condition led to a drastic reduction both in CO and NO_X emissions (case 13pAT10), because of the sufficient amount of air and low peak temperature.

Table 4.5 Some of the important quantities predicted at the outlet of the final geometry. Changed input variables are printed bold.

Case	*Air state*	T_i *[K]*	*φ*	*TIT [K]*	T_{max} *[K]*	*CO [ppm]*	NO_X *[ppm]*
12p	Fresh	1000	0.3	1616.7	2529	549	348
13p	**Vitiated**	1000	0.43	1578.6	2139	615	64
*13pAT10**	Vitiated	1000	**0.14**	1197.1	1675	175	0.5

*New case definition for the inlet conditions adopted from the AHEAD project. The small case letter behind the first two digits define the geometry type, A is short for AHEAD, afterwards followed either by T or C indicating Take-Off or Cruise condition respectively and finally the last two digits indicate the inlet temperature x 100 K.

Looking at figure 4.8, the radical pool in the flame region was considerably less concentrated with the vitiated air cases. Case 13p showed a less distributed flame than case 12p and this was mainly due to the higher oxygen concentration provided by the secondary air, leaving more oxygen to be consumed in the upstream part of the cavity, whereas in case 13p the oxygen was completely consumed. Case 13pAT10 had a completely different flame structure since more excess air was provided and enough oxygen remained inside the entire liner. The EDC model could finally show its ability to predict ignition delay and also the less sharp temperature increase due to the very low oxygen concentration in the region of the fuel inlet (Figure 4.9) where the maximum molar fraction was about 0.11. The fuel mixture was entrained by the vortex which was focused more downstream of the cavity. Due to the acceleration of the flow at the reaction zone and the low momentum flow in the upstream part of the cavity the separation zone in the upstream corner was enlarged into a second clockwise-rotating vortex. This secondary vortex was isolated from the air inlet which led to an even further decrease in O_2 concentration and rise in temperature (though it must not be forgotten that some of the heat would be transferred outside the liner). This caused the less evenly distributed temperature upstream and downstream of the cavity. The vortex created an ideal recipe for FC.

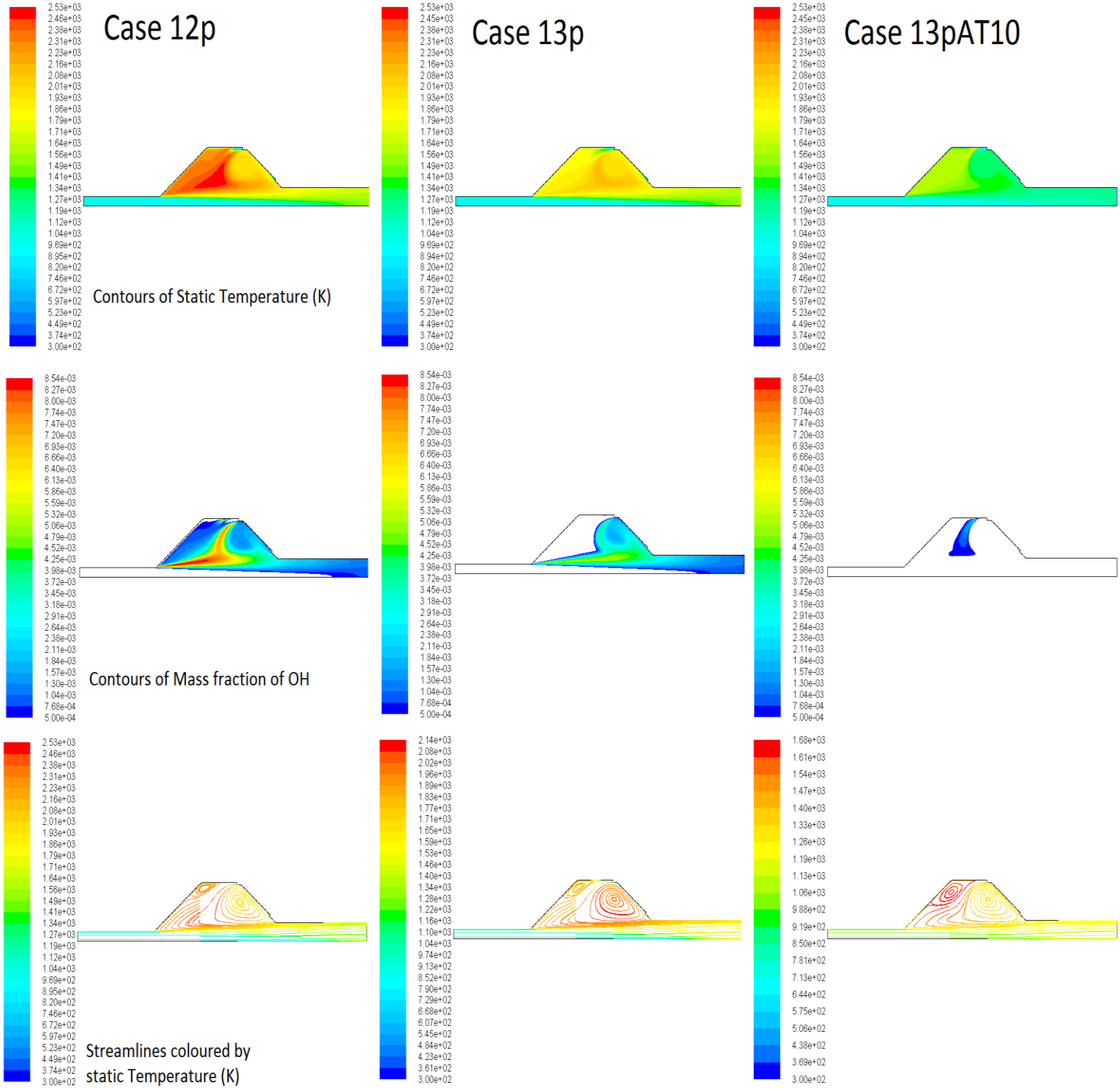

Figure 4.8 Contour plots of Static temperature(top), OH mass fraction (centre) and streamline patterns coloured by temperate (bottom) for the cases 12p 13p and 13pAT10 (geometry is off scale).

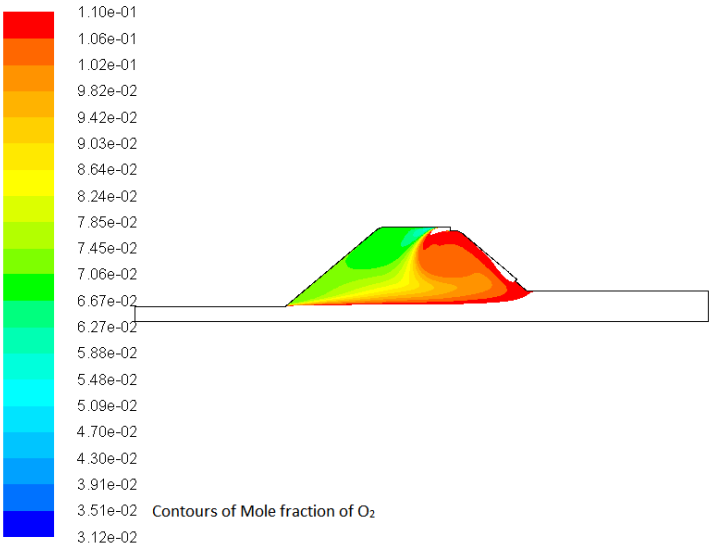

Figure 4.9 Contour plot of the Mole fraction of O_2 (case 13pAT10)

4.2.3 Effect of Inlet Temperature, Recirculation Ratio and Equivalence Ratio

Starting from case 13pAT10 the inlet temperature was varied up to 1200 K, a temperature comparable to the AHEAD's hybrid engine. Also the equivalence ratios during take-off and cruise were adopted from this engine. Finally the inlet size was varied to change the recirculation ratio and was repeated with constant inlet mass flow rate and constant inlet velocity. The results are shown in figure 4.10. Figures 4.10a and 4.10b show the familiar effect of increased temperature and equivalence ratio. Both parameters caused higher reaction rates, improving the oxidation of CO. However they also caused higher peak temperatures which led to an exponential growth of mainly thermal NO_X formation.
Although varying inlet size would change K_V, the inlet speed would also be different. Allowing this caused the CO formation to rise (figure 4.10c). This might probably be due to the effect of lower residence time and higher heat dissipation caused by the faster jet; both effects that hinder the oxidation of CO. If the inlet velocity was remained constant (by adjusting the mass flow rate instead) there was a negligible effect of K_V on CO emissions. The NO_X formation however did depend on K_V regardless of the inlet velocity. This was primarily due the effect of higher peak temperatures associated with lower K_V.

To verify the reaction mechanism, a calculation was run with one of the cases using the full GRI mechanism. The output values are shown in table 4.6. The drm19 mechanism achieved comparable data as the GRI 3.0. However, when the NO_X was predicted without the post-processor its formation reduced by a factor 2, but still in the same order of magnitude.

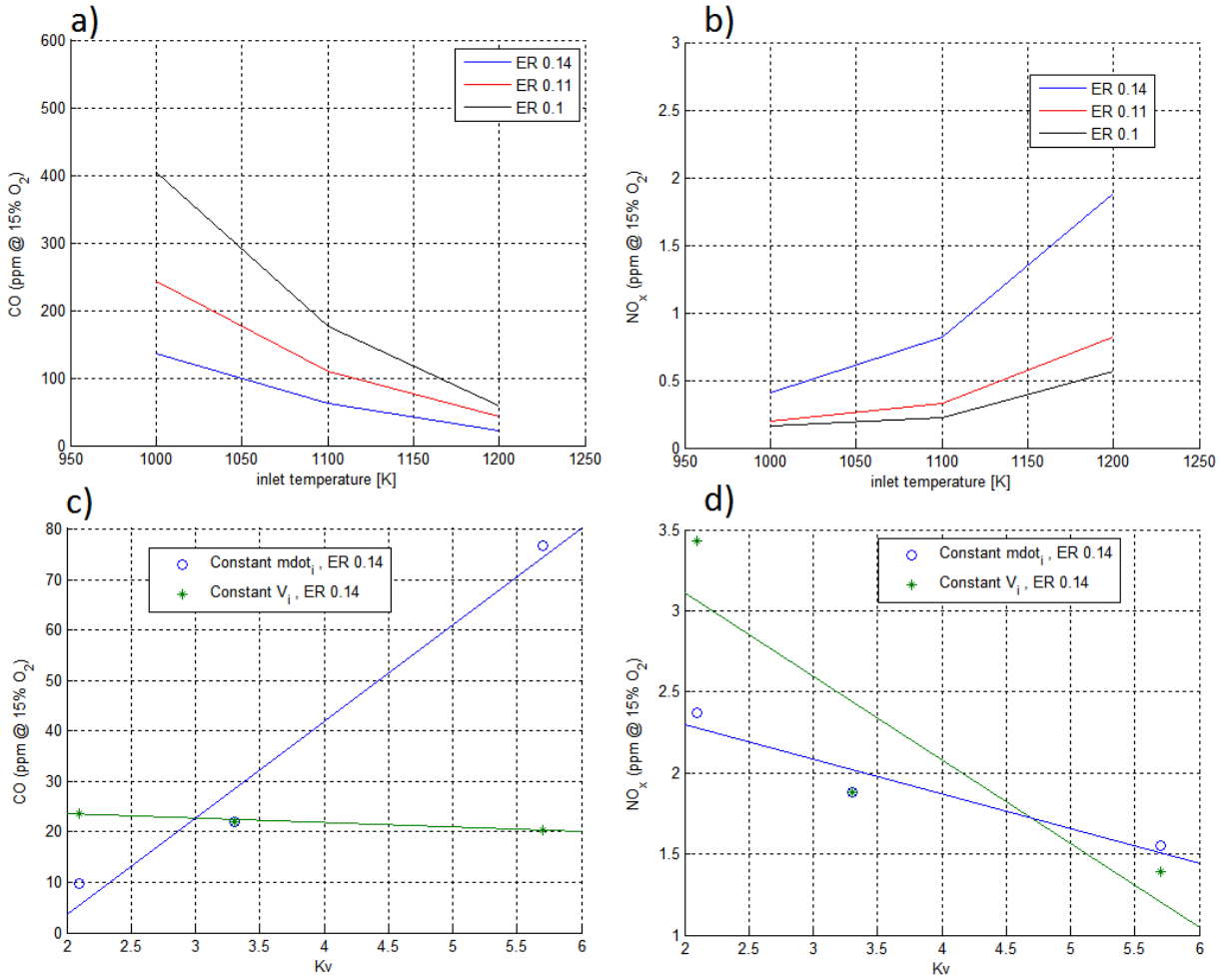

Figure 4.10 NO_X and CO emissions as function of K_V and equivalence ratio ER.

Table 4.6 Comparison of the reaction mechanisms drm19 and GRI 3.0 applied on case 13pAT12.

Case	***Reaction mechanism***	***T_i [K]***	***TIT [K]***	***T_{max} [K]***	***CO [ppm]***	***NO_X [ppm] with post-processor***	**NO_X [ppm] without post-processor**
13pAT12	DRM19	1200	1382	1834	27	2.3	
13pAT12	GRI 3.0	1200	1384	1843	29	2.7	1.05

In order to be able to answer the main objective question, whether it is possible to apply FC to an aero engine, the geometry had to be tested with an ATC. Although simulations have shown that the CTC could achieve very low pollutant emissions, the main downside was the fact that with this configuration the combustor also had a much low power density than the ATC.

With equation 4.1, the power density *PD* can be calculated

$$PD = \frac{\dot{m}\bar{c}_p(T_o - T_i)}{V_{comb}} \tag{4.1}$$

Where $\bar{c}_p$ denotes the average specific heat capacity between the inlet and outlet and V_{comb} the combustor volume. For the final model (case13pAT12) it was shown that the ATC had a power density six times of that of an CTC with the same inlet velocity, making it much more attractive to aero engine manufacturers. However, since a CTC had a much higher K_V than a ATC, its inlet size could increase to allow more mass flow to enter at the same speed. Hence there is a possibility to increase its power density, but may reduce its benefits in terms of NO_X emissions.

4.3 Annular Type Combustor

The final model in the previous section was great in achieving low pollutant emissions in a CTC but when applied to a ATC it did not perform as good; the CO emissions increased by almost twentyfold (nearly 500 ppm). Due to the area ratio of the ATC being 6 times as small as with the CTC the velocity of the recirculated flow was nearly 6 times as high (from 24m/s to 140 m/s), which led to high heat dissipation and a residence time 5 times as short (see figure 4.11). Also, since higher momentum is achieved in the recirculated flow no separation occurred at the cavity corner which led to the disappearance of the stabilising secondary vortex. The resulting delayed ignition is clearly seen in figure 4.12. In terms of NO_X formation the low residence time was beneficial, hence was hardly affected (5 ppm).

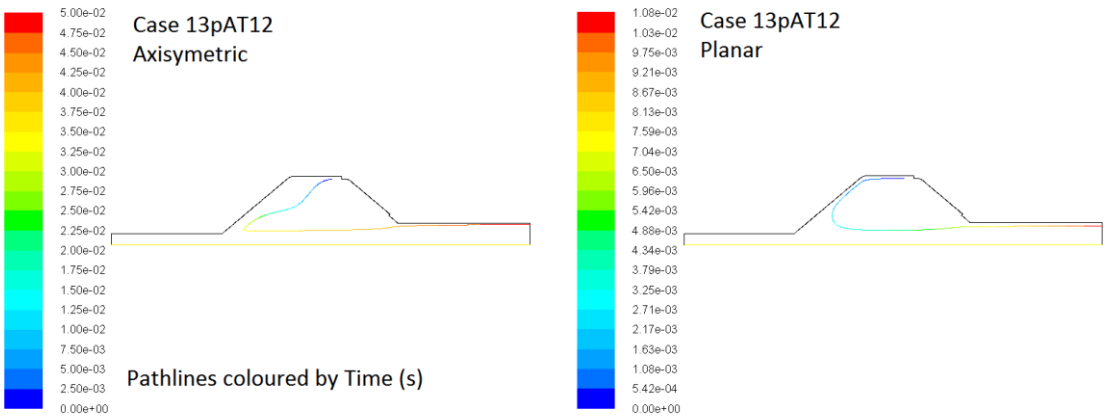

Figure 4.11 Path line from the fuel inlet coloured by time showing the residence time.

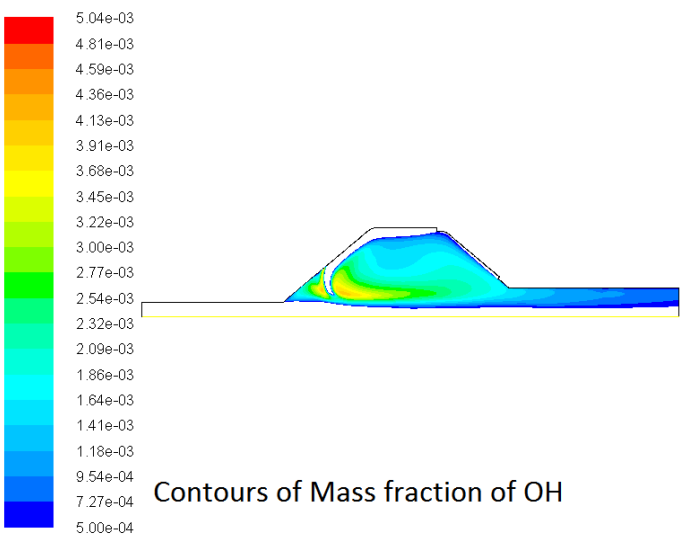

Figure 4.12 Contours of the OH mole fraction in case 3pAT12

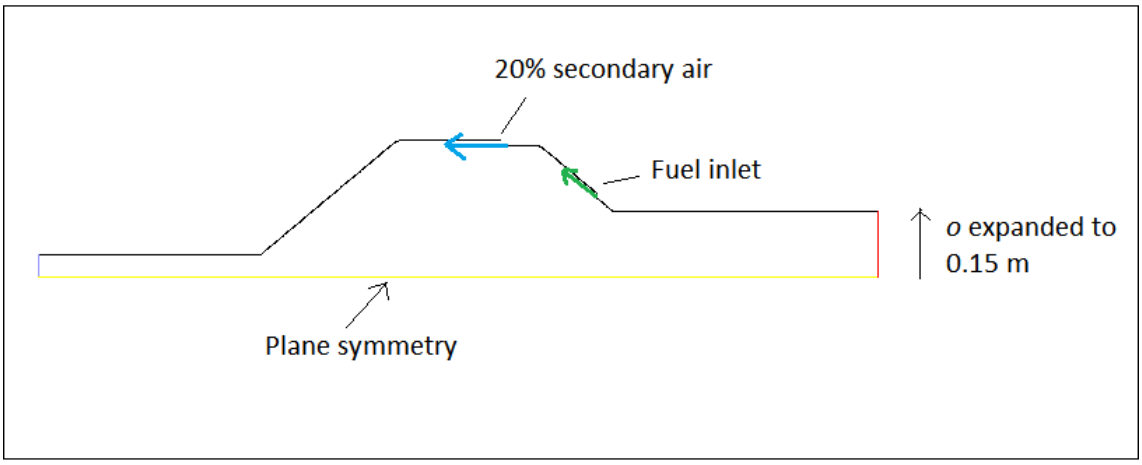

Figure 4.13 Final CTC model adapted to the ATC

A solution strategy which would help increase the residence time was to expand the outlet size even more and to switch the fuel inlet with the secondary flow inlet at the end of the cavity (case 3rAT12), as shown in figure 4.13. Ignition was close to the fuel inlet. This reduced the CO emission by more than half but the NO_X formation increased dramatically to 65 ppm and was caused by the very high peak temperature. It was also attempted to reduce the inlet size (NB, resulting inlet velocity of 330 m/s) in order to increase K_V: case 3sAT12. The NO_X formation dropped to 9.7 ppm, but CO emission had increased to 298 ppm. A Comparison of some contour plots is shown in figure 4.14.

Although the oxygen concentration was less in the cavity with inlet size of 0.05m, the dissociation due to the higher temperature led to more formation of the radicals O and OH. With the smaller inlet size the ignition was delayed but this was not due to higher K_V. The reason why the temperature was lower and O_2 higher with higher recirculation ratio was

more clear when looking at the flow vectors (figure 4.15). The difference in inlet and outlet size was too high for the flow to reattach at the outlet corner for case 3sAT12 and was postponed to after the cavity, leading to more entrainment of the colder primary jet by the recirculation zone. This was the cause of the reduction in both reaction rate and peak temperature, not because of increased K_V.

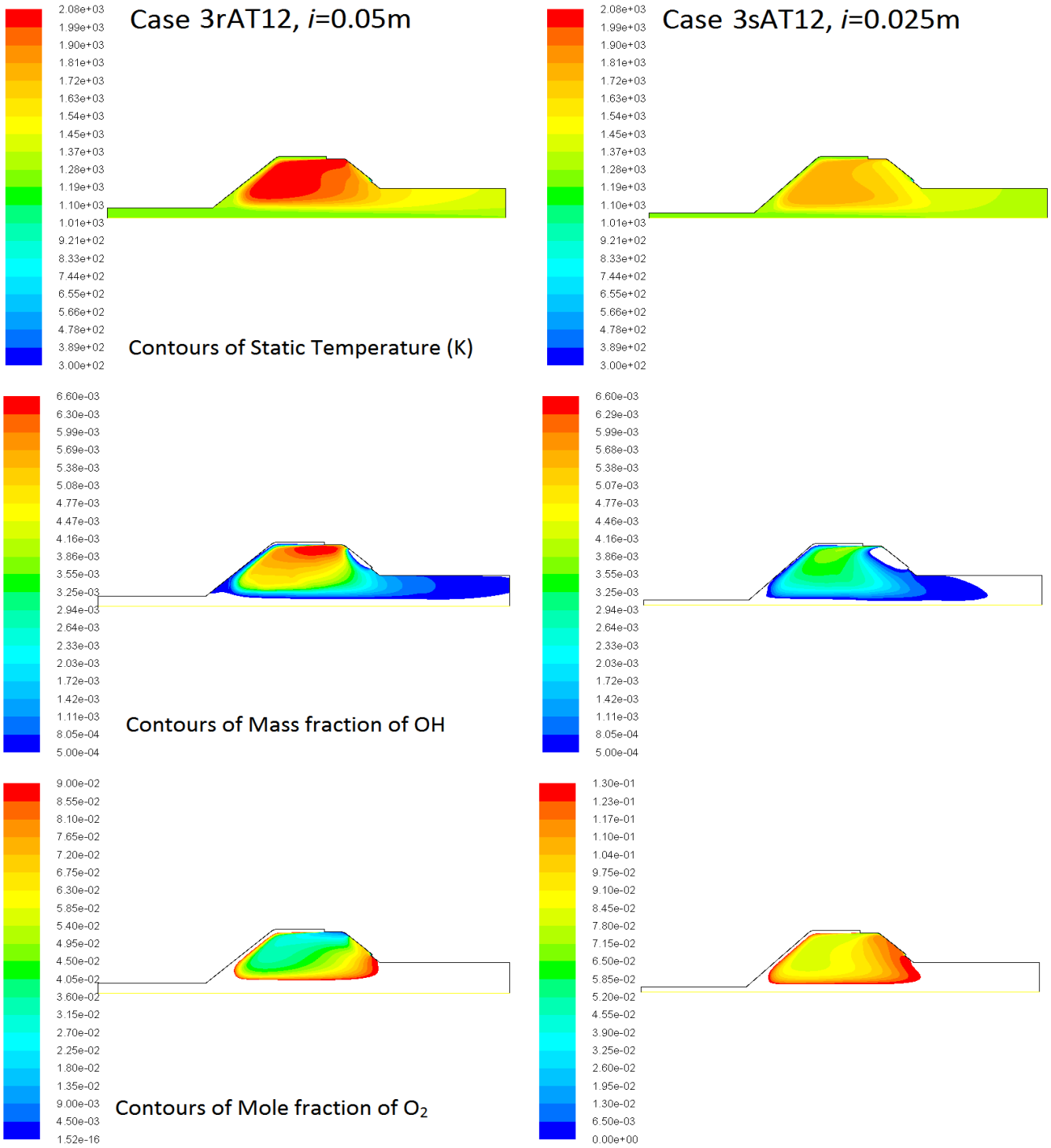

Figure 4.14 Contour plots of Static temperature (top), OH mass fraction (centre) and O_2 molar fraction (bottom) of the cases 3rAT12 and 3sAT12.

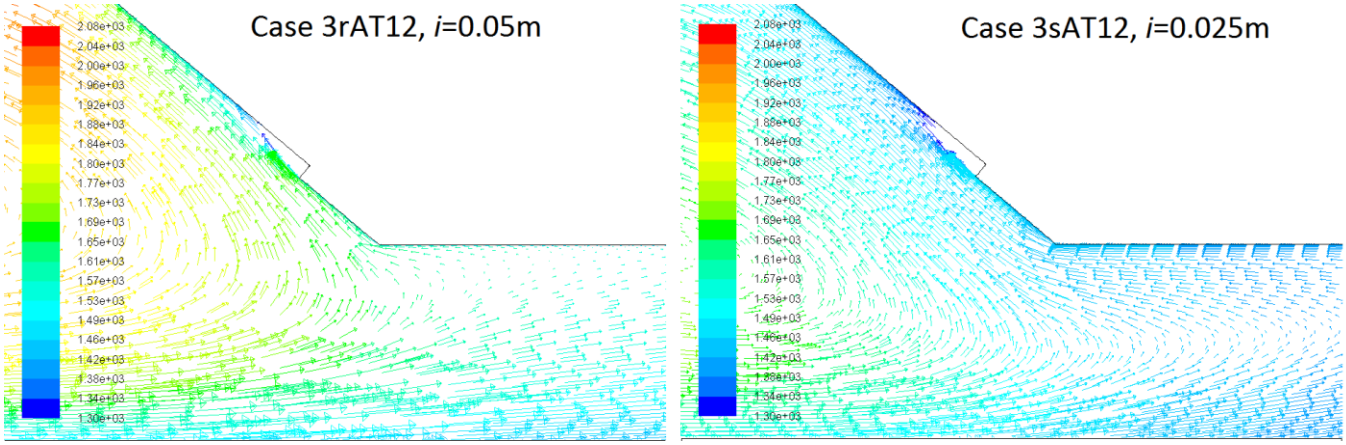

Figure 4.15 Vector plots coloured by Static Temperature of the cases 3rAT12 and 3sAT12.

Under cruise condition (3rAC12 and 3sAC12) the NO_X emissions reduced significantly in both cases due to lower peak temperatures. The CO emissions also dropped for case 3rAC12 which was counter intuitive. This was probably caused due to the fact that CO was mainly formed near the fuel inlet at take-off but at cruise there was both an ignition delay and less fuel injection leading to a less fuel-rich formation. A summary of the important data is given in table 4.7 .

The ATC was finally used to simulate actual flight conditions by also pressurising the inlet air (cases 4rAT12 and 4rAC12). This led to an improved reaction rate and the CO emissions were further reduced to below 100 ppm. Although the NO_X emission reduced by an order of magnitude at take-off (4.4 ppm), it nearly doubled at cruise. The reduction of NO_X seemed counter intuitive. Especially NO formation via the N_2O path, which involves 3rd body reactions, is known to be favoured with increased pressure. The model showed that the consumption rate of NO was much higher at take-off as compared to cruise (which was at less elevated pressure). The reason of this opposing behaviour of NO_X formation was unknown and needs to be further studied.

Except for the cases where *i*=0.025m which led to a pressure drop of 6%, in all other cases the loss was less than 3% which was within the limitation of an aero engine.

Table 4.7 Summary of some important input and output quantities of the cases for the ATC.

Case	***T_i [K]***	***φ***	***Pressure [bar]***	***$\dot{m}_i$ [kg/s]***	***TIT [K]***	***T_{max} [K]***	***CO [ppm]***	***NO_X [ppm]***	***dp/p***
3pAT12	1200	0.14	1.01325	1.15	1384	1840	491	5.0	0.023
3rAT12	1200	0.14	1.01325	1.15	1385	2075	207	65.0	0.027
3sAT12	1200	0.14	1.01325	1.15	1352	1800	298	9.7	0.061
3rAC12	1200	**0.1**	1.01325	1.15	1333	1891	134	13.5	0.027
3sAC12	1200	0.1	1.01325	1.15	1309	1604	576	0.2	0.059
4rAT12	1200	0.14	**12**	13.79	1392	2268	80	4.4	0.027
4rAC12	1200	0.1	**4.9**	5.517	1337	1995	96	20.0	0.027

5

Conclusions

This thesis has presented an attempt to design a conceptual flameless combustor using detailed numerical analysis. The challenge of implementing FC into an aero engine was well addressed and the design limits were clear. Due to time restriction and unclear design direction some simplifications were necessary, such as 2D simulation, but were justified and still expected to achieve realistic results qualitatively.

During validation of the cold flow the RANS-based turbulence models have shown to under predict the recirculation ratio except for the most upstream region. Of all the tested turbulence models (although $K_{v\text{-}max}$ was under predicted by 20-30%) the k-ε Realizable model performed best overall and showed good agreement regarding the reattachment distance which was helpful in understanding the reacting flow behaviour in the later stage. Also the trend of K_V in relation with channel-to-inlet area ratio was similar to the measurements which was important to determine the sizes of the concept since K_V has shown to heavily depend on chamber-to-inlet area ratio A/a ($K_V \propto 0.09\ A/a$ for a planar model and $K_V \propto 0.04\ A/a$ for a cylindrical model). The DES model showed difficulty in capturing the weak flow instability near the separation point and failed to reproduce the velocity profiles almost in the entire domain. The result of the ELES model however showed comparable results to the RANS k-ε Realizable model. Although it must be admitted that the grid resolution of three million cells was still very coarse for LES standard which still led to a runtime of two weeks while RANS only required 3 hours (even a few minutes when in 2D).

The recirculation ratio was not influenced by the air injection speed as the circulation of the vortices changed proportionally. Adding a cavity increased $K_{V\text{-}max}$ with nearly 30%, however adjusting the cavity shape had a minor effect and was only beneficial in the reduction of pressure losses down to 1.8%. With the combination of achieving the highest area ratio possible in an aero engine and adding a cavity, the ATC could achieve a K_V value of up to 1.3 whereas a CTC reached nearly 3. This excluded the under estimation of 20-30%. It was shown that combustion did not globally alter the structure of the vortex but rather had an enhancing effect in its circulation. However due to the high temperature in the cavity that led to low density, $K_{V\text{-}max}$ reduced by a factor of two.

The EDC model was able to show with the detailed reaction mechanism that when the O_2 concentration reduced it had the ability to predict ignition delay, lower temperature rise and expansion of the reaction zone. The NO formation via the intermediate N_2O should not be

excluded in the prediction as the post-processor has shown that it played a major part in the total formation of NO, up to 50%. The reduced reaction mechanism was verified with the full GRI mechanism and showed comparable data.

Even with K_V of almost 3 in the CTC, the NO_X emissions were very high when the working fluid was fresh air. Only with vitiated air could it reduce to ultra-low levels. When fixing the geometry, the equivalence ratio and inlet temperature showed the familiar effect on the emissions. Both parameters cause higher reaction rates when increased, improving the oxidation of CO. However they also cause higher peak temperatures leading to an exponential growth of mainly thermal NO_X formation. There was a negligible effect of K_V on the CO emissions. The NO_X formation however reduced with increasing K_V. This is primarily due the resulting higher peak temperatures. The CTC was able to emit less than 50 ppm of CO and less than 2 ppm of NO_X both at cruise and take-off condition.

The main downside of the CTC was that it had a power density six times as low as that of the ATC in this configuration. The amount of CTC's needed in this configuration would not fit in an aero engine. The ATC however did not perform as good in terms of CO emissions that increased by an order of magnitude. The much lower area ratio of an ATC induced very high rotational speed of the vortices leading to a fivefold decrease in residence time. This gave more difficulty in the modifying the combustor and needs to be given more attention. By shifting the fuel inlet to the rear side of the cavity, the CO emissions could reduce to below 200 ppm. A few further modification attempts in the remaining time were not more successful. The increase of K_V by making the inlet size smaller showed a substantial increase in CO and reduction in NO_X but for different reasons than in a CTC. The reduction of inlet size altered the cavity flow due to delayed reattachment causing more of the colder primary flow to be entrained in the recirculation zone, lowering both the reaction rate and peak temperature, even though O_2 concentration increased.

What was clear in the design of the CTC and ATC is that the threshold values of K_V given in the literature were merely an indication to pursue the lowest O_2 concentration at the point of ignition. To achieve this low concentration required good control of the flow and the right positioning of the fuel inlet so that it remained in a zone were the O_2 molar fraction is around 0.1 max (which is mostly far upstream). On the other side sufficient O_2 concentration, residence time, and high temperature should be arranged for the CO to oxidise. This is especially challenging in an ATC, though the vitiated air gave more design freedom and was necessary since K_V will always be lower than 1 with this configuration. The K_V is certainly necessary in achieving FC but not a sufficient criterion. As the results were only given by one combustion model, the values should only be regarded in qualitative sense although they've encouraged further verification.

6

Recommendations

So far the first simulation results with the 2D model were promising and showed the feasibility to apply FC in a secondary aero engine combustor. Off course this can never be certain without any verification and validation. Therefore the following steps are recommended.

First it is necessary to compare the EDC model with other detailed and finite-rate chemistry models to see whether they achieve comparable results in the same order of magnitude. Two other promising models in ANSYS Fluent are the Composition Probability Density Function Transport method and the more simplified Flamelet Generated Manifold which is a partially premixed combustion model. Both of them have been applied many times for modelling FC in furnaces.

The effect of radiative heat transfer to the annulus has been neglected and should be incorporated. Heat transfer to the annulus might help reduce pollutant emissions even further. It is predicted that the peak temperature will reduce to further avoid NO_X formation and the warmed up secondary flow will improve CO consumption near the cavity walls.
Also a more detailed sensitivity analysis with pressure is required to better understand its effect on pollutant formation.

An annular shaped primary air inlet in the ATC is structurally challenging. A next step would be to generate a slice of a full 3D model with the annular jet being split up in multiple circular jets which is a more realistic configuration. This will include the complex interaction of the jets and also the connection of the cavities' recirculation zones in between the jets. The additional flow complexity might cause a difference in the formation of the pollutants and the discrepancies need to be quantified.

The pdf method of the turbulence-chemistry interaction model in the NO_X post processor incorporates fluctuations of composition and temperature in the time averaged field. However it would be good to verify this in a deterministic approach by using the ELES model to actually predict hot spots that usually are the main sources of NO_X formation.

After all the mentioned steps have been gone through, it is recommended to validate the predictions with experiments.

7

Bibliography

[1] Mattingly, J.D., Heiser, W.H., and Pratt, D.T, "Aircraft Engine Design", American Institute of Aeronautics and Astronautics, Inc., Reston, Virginia, 2002.

[2] Purdue School of Aeronautics and Astronautics, "Burner (Combustor)." [Online]. Available: https://engineering.purdue.edu/~propulsi/propulsion/jets/basics/burner.html [Accessed: 20 July 2015], 2015.

[3] Magnussen, B.F., "On the structure of turbulence and a generalized eddy dissipation concept for chemical reaction in turbulent flow", 19th American Institute of Aeronautics and Astronautics, aerospace science meeting, St. Louis, Missouri, 1981.

[4] Roekaerts, D., and Peeters, T. , Lecture notes "Turbulent Reacting Flows", section heat transfer, faculty of applied physics, Delft University of Technology, Delft, 1997.

[5] Ruijgrok, G.J.J., and van Paassen, D.M., "Elements of Aircraft Pollution", Delft University Press, Delft, 2005.

[6] Lefebvre, A.H., and Ballal, D.R., "Gas Turbine Combustion, Alternative fuels and Emissions", third edition, Taylor & Francis Group, Boca Raton, Florida, 2010

[7] Tobacco, D., Innarella, C., Bruno, C., "Theoretical and Numerical Investigation on Flameless Combustion", Combustion Science and Technology 174:7, Taylor & Francis, London, 2002.

[8] Wulff, A., and Hournouziadis, J., "Technology review of aero-engine pollutant emissions", Journal of Aerospace Science and Technology 8, pp. 557-572, 1997.

[9] Wünning, J.A., and Wünning, J.G.,"Flameless Oxidation to reduce Thermal NO-formation", Progress in Energy and Combustion Science, Elsevier Science Ltd.,1997

[10] Tsuji, H., Gupta, A.K., Hasegawa, T., Katsuki, M., Kishimoto, K., Morita, M., "High Temperature Air Combustion, from Energy Conservation to Pollution Reduction", CRC Press, Boca Raton, Florida, 2003.

[11] Cavaliere, A., and de Joannon, M., "Mild Combustion", Progress in Energy and Combustion Science 30, Elsevier Ltd., 2004.

[12] Newby, J.N., “21 YEARS OF REAL-WORLD LOW NO_X INJECTION (“LNI”)”, AFRC 2013 Industrial Combustion Symposium, Fives North American Combustion Inc., Kauai, 2013

[13] Wünning, J.G., “FLOX® - Flameless Combustion”, Thermprocess Symposium, 2003.

[14] Gangoli Rao, A. and Levy, Y.,“ A New Combustion Methodology for Low Emission Gas Turbine Engines”, 8th HiTACG conference, 2010

[15] Levy, Y., Rao, A.G., and Sherbaum, V., ” Chemical Kinetic and Thermodynamics of Flameless Combustion Methodology for Gas Turbine Combustors”, American Institute of Aeronautics and Astronautics, Cincinnati, 2007.

[16] Guillou, E., Cornwell, M., and Gutmark, E., “Application of “Flameless” Combustion for Gas Turbine Engines”, American Institute of Aeronautics and Astronautics, 2009.

[17] Cornwell, M., Overman, N., and Gutmark, E., “Flameless Combustion Systems for Gas Turbine Engines”, US patent 20100287939A1, USA, 2010

[18] Levy, Y., Sherbaum, V., and Arfi, P., “Basic thermodynamics of FLOXCOM, the low-NOx gas turbines adiabatic combustor”, Applied Thermal Engineering 24, Elsevier Ltd., 2004.

[19] Flamme, M., “New combustion systems for gas turbines (NGT)”, Applied Thermal Engineering, Vol. 24, 2004.

[20] Sadanandan, R., Lückerath, R., Meier, W., Wahl, C., “Flame Characteristics and Emissions in Flameless Combustion Under Gas Turbine Relevant Conditions”, Journal of Propulsion and Power, Vol. 27, 2011.

[21] Ferziger, J.H., and Milovan, P., “Computational Methods for Fluid Dynamics”, third edition, Springer-Verlag, Berlin, 2002

[22] Parente, A., Galletti, C., Tognotti. L., ”A simplified approach for predicting NO formation in MILD combustion of CH4–H2 mixtures”, Proceedings of the Combustion Institute 33, Elsevier Ldt, 2010.

[23] Shih, T.H., Liou, W.W., Shabbir, A., Yang, Z., and Zhu, J., "A New k-ε Eddy Viscosity Model for High Reynolds Number Turbulent Flows - Model Development and Validation", NASA, 1994.

[24] ANSYS FLUENT 14.0, “ANSYS FLUENT Theory Guide”, SAS IP Inc., 2011

[25] Vaz, D.C., “Towards the Application of Flameless Combustion to Micro Gas Turbines”, PhD thesis, Universidade Nova de Lisboa, Lisboa, 2007

[26] Christo, F.C., and Dally, B.B.," Modeling turbulent reacting jets issuing into a hot and diluted coflow", Combustion and Flame 142, Elsevier Ltd., 2005.

[27] Barths, H., Peters, N., Brehm, N., Mack, A., Pfitzner, M., and Smiljanowski, V., "Simulation of pollutant formation in a gas turbine combustor using unsteady flamelets", 27th Symposium on Combustion, The Combustion Institute, 1998

[28] Coelho, P.J., and Peters, N., "Numerical Simulation of a Mild Combustion Burner", Combustion and Flame 124:503–518, The Combustion Institute, Elsevier Ltd., 2001

[29] Magnussen B.F., and Hjertager, B.H.,"On Mathematical Modelling of Turbulent Combustion With Special Emphasis on Soot Formation and Combustion", The Norwegian Institute of Technology, 1976.

[30] Parente, A., Galletti, C. , Tognotti, L., "Effect of the combustion model and kinetic mechanism on the MILD combustion in an industrial burner fed with hydrogen enriched fuels", International Journal of Hydrogen energy 33, Elsevier Ltd., 2008

[31] Cryptome, "GE failures" [Online]. Available: http://cryptome.org/ge-failures.htm [Accessed: April 5th 2014], 2014.

[32] Gas turbine Simulation Program, "Downloads" [Online]. Available: http://www.gspteam.com/downloads [Accessed: April 5th 2014], 2014.

[33] Ruck, B. , Makiola, B. , "Flow separation over the step with inclined walls.", Near-Wall Turbulent Flows (R.M.C. So, C.G. Speziale, B.E. Launder, eds.), Elsevier, p. 999., 1993.

[34] Shur, M.L., Spalart, P.R., Strelets, M.Kh., Travin, A.K., "A hybrid RANS-LES approach with delayed-DES and wall-modelled LES capabilities.", International Journal of Heat and Fluid Flow Vol. 29, Elsevier, 2008

[35] Alstom, "GT24 and GT26 gas turbines" [Online]. Available: http://www.alstom.com/products-services/product-catalogue/power-generation/gas-power/gas-turbines/gt24-gt26-gas-turbines/ [Accessed: July 5th 2015], 2015.

[36] AHEAD - EU project, "Project description" [Online]. Available: http://www.ahead-euproject.eu/project-description/ [Accessed: March 8th 2015], 2015.

[37] Kazakov, A., Frenklach, M., GRI-Mech, "Reduced Reaction Sets based on GRI-Mech 1.2" [Online]. Available: http://combustion.berkeley.edu/drm/ [Accessed: February 25th 2015], 2015.

Appendix A.

MATLAB script to determine K_V

Basic script

```
clear all
close all
clc

tic
%names of the data folders without the last digits that represent the
distances in X-direction
datagroup1=     'H30TAV_Reac_case13pAT12_NOx_L40i5o10a50_data';
datagroup2 =    'H30TAV_Reac_case13pAT12_NOx_L40i4o10a50_data';
datagroup3 =    'H30TAV_Reac_case13pAT12_NOx_L40i6o10a50_data';


%axial distances of the vertical rakes to extract data(in millimetres)
distances60   = [0, 25, 50, 75, 100, 125, 150, 175, 200, 225, 250, 275,
300, 350, 400, 450, 500, 550];
distances40   = [0, 25, 50, 75, 100, 125, 150, 175, 200, 225, 250, 275,
300, 350];
%distances30 = [0, 25, 50, 75, 100, 125, 150, 175, 200, 225, 250, 275];

%Call function GetVxKv to extract Vx and calculate Kv
[Vx1,y1,x1, Kv1] = GetVxKv(distances40,datagroup1);
[Vx2,y2,x2, Kv2] = GetVxKv(distances40,datagroup2);
[Vx3,y3,x3, Kv3] = GetVxKv(distances40,datagroup3);


%convert x-distance to metres
x40=distances40/1000;
x60=distances60/1000;

%interpolate Kv
x40_interp=0:0.005:(max(x40));
x60_interp=0:0.005:(max(x60));

Kv1_interp=interp1(x40,Kv1,x40_interp,'spline');
Kv2_interp=interp1(x40,Kv2,x40_interp,'spline');
Kv3_interp=interp1(x40,Kv3,x40_interp,'spline');

%determine Kv_Max
KvMax_1=Kv1_interp((Kv1_interp==max(Kv1_interp(:))));
KvMax_2=Kv2_interp((Kv2_interp==max(Kv2_interp(:))));
KvMax_3=Kv3_interp((Kv3_interp==max(Kv3_interp(:))));
```

Function that returns V_X and K_V.

```
function [Vx,y,x,Kv_sim] = GetVxKv(X, datagroup)


for i=1:length(X)

dataname=strcat(datagroup,num2str(X(i)));

simulation  = importdata(dataname,' ',1);  %import data files of all
prompted X-locations


%calculate inlet properties (x/H = 0)

dataname0     = strcat(datagroup,num2str(X(1)));
simulation_X0 = importdata(dataname0,' ',1);     %data file at inlet (X=0)

Vx_inlet0  =  simulation_X0.data(:,5);  %velocities in X-direction at inlet
Y_inlet0   =  simulation_X0.data(:,3);  %Y-locations at inlet
rho_inlet0 =  simulation_X0.data(:,4);  %densities at inlet
Y_dist_inlet0_iter(1) = 0;              %Y-distance between 2 data points
at inlet

    for k=2:length(Y_inlet0)  %Y-distance and data at the wall is neglected

            Y_dist_inlet0_iter(k) = abs(Y_inlet0(k)-Y_inlet0(k-1));
    end

Y_dist_inlet0 = Y_dist_inlet0_iter';    %transpose of Y_dist_inlet0_iter


Vx{:,i}  = simulation.data(:,5);        %velocity in X-direction
rho{:,i} = simulation.data(:,4);        %density
y{:,i}   = simulation.data(:,3);        %location in Y-direction
x{:,i}   = simulation.data(:,2);        %location in X-direction


%calculate the rest

[Vx_neg_i,Vx_neg_j] = find(Vx{1,i}<0);    %if result is an empty double, it
                                          %means Vx-neg doesn't exist

V_neg   = Vx{i}(Vx{i}<0);          %velocity in negative X-direction
Y_neg   = y{1,i}(Vx_neg_i);        %to find y-position index to the
                                   %corresponding negative Vx index

rho_neg = rho{1,i}(Vx_neg_i);      %to find density index to the
                                   %corresponding negative Vx index

V_neg_collection{i}   = V_neg;    %collect all negative Vx
Y_neg_collection{i}   = Y_neg;    %idem corresponding y-location
rho_neg_collection{i} = rho_neg;  %idem corresponding density

Y_dist_neg = zeros(length(V_neg),1); %Y-distance between two data points
```

```
%this if-statement assigns a Y-distance for the first data point

if isempty(Vx_neg_i)==0     %to check if V_neg_i is empty. 0= false
        if Vx_neg_i(1)  == 1;
           Vx_neg_i(1)  = 2;
           Y_dist_neg(1)=(abs(y{1,i}(Vx_neg_i(2))-y{1,i}(Vx_neg_i(1))))

           Y_dist_neg(2:length(V_neg)) =
                               (abs(y{1,i}(Vx_neg_i(2:length(V_neg)))...
                                   -y{1,i}(Vx_neg_i(2:length(V_neg))-1))) ;
        else
         Y_dist_neg=(abs(y{1,i}(Vx_neg_i)-y{1,i}(Vx_neg_i-1)));
        end
    else
        Y_dist_neg=(abs(y{1,i}(Vx_neg_i)-y{1,i}(Vx_neg_i-1)));
    end


Y_dist_neg_collection{i}=Y_dist_neg;


%calculate Kv

Kv_sim(i)=abs(sum(V_neg_collection{i}.*Y_dist_neg_collection{i}.*rho_neg_co
llection{i})...
              /(sum(Vx_inlet0 .* rho_inlet0 .* Y_dist_inlet0) / 1));

%in case geometry is axisymmetric

%Kv_sim{i}=abs(sum(V_neg_collection{i}.*Y_dist_neg_collection{i}.*rho_neg_c
ollection{i}.*Y_neg_collection{i}))... %V*d*rho*(2*pi*r)
%             /(sum(Vx_inlet0 .* rho_inlet0 .* Y_dist_inlet0 .* Y_inlet0));

end
```

Appendix B.

Design Modifications and Output Data

This section gives a summary of the geometry modifications followed by the resulting simulation data.

Geometry cases

a)

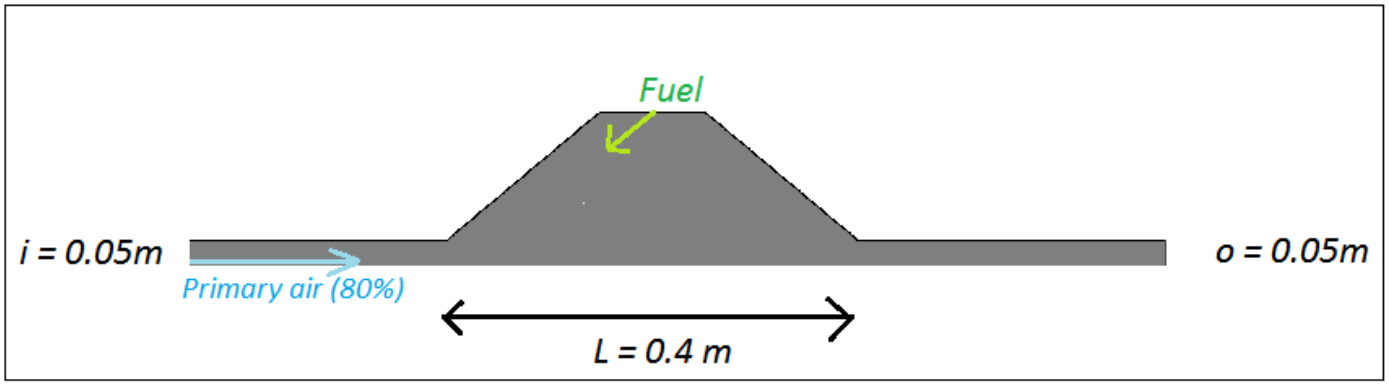

b)

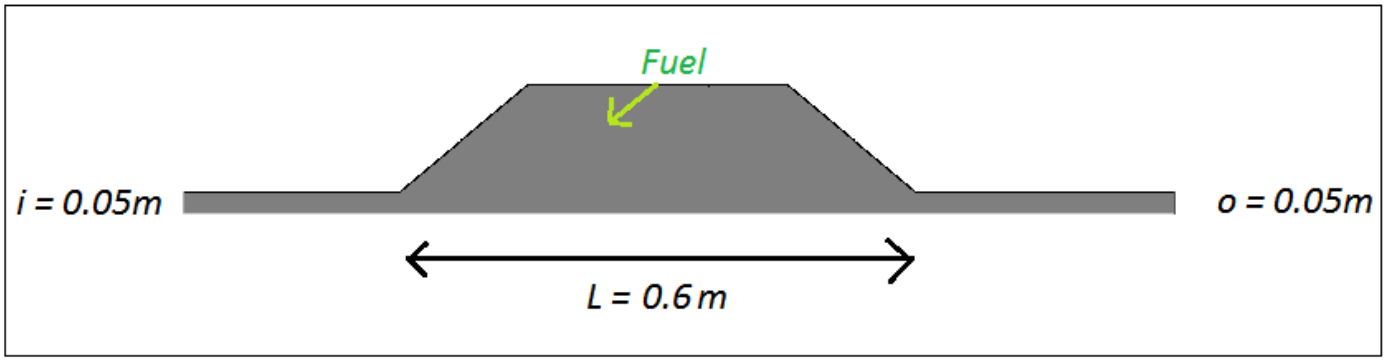

c)

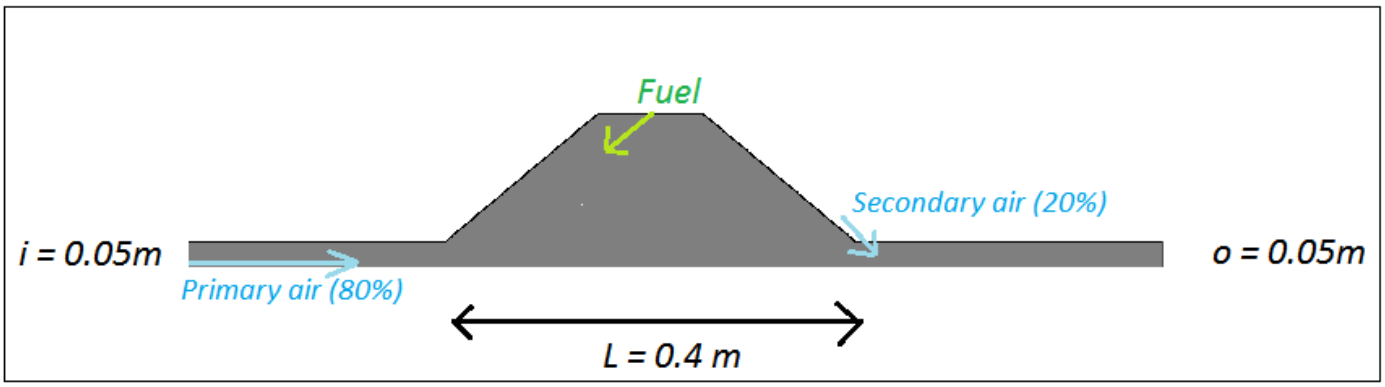
Fuel
Secondary air (20%)
i = 0.05m
o = 0.05m
Primary air (80%)
L = 0.4 m

d)

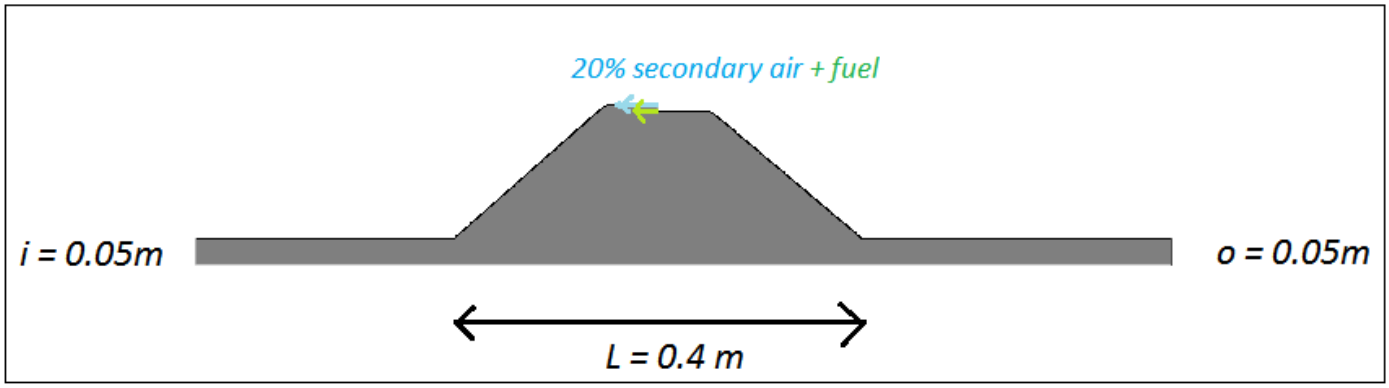
20% secondary air + fuel
i = 0.05m
o = 0.05m
L = 0.4 m

d2)

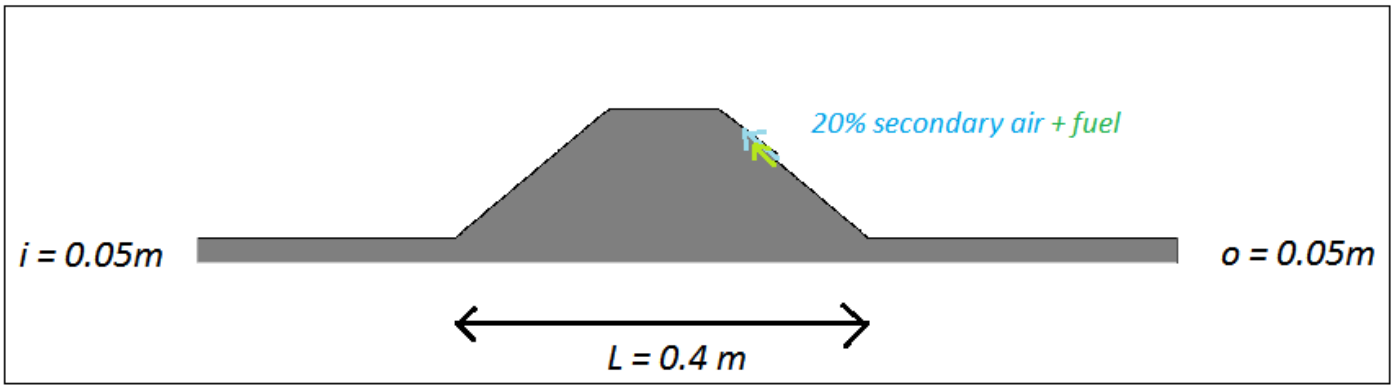
20% secondary air + fuel
i = 0.05m
o = 0.05m
L = 0.4 m

e)

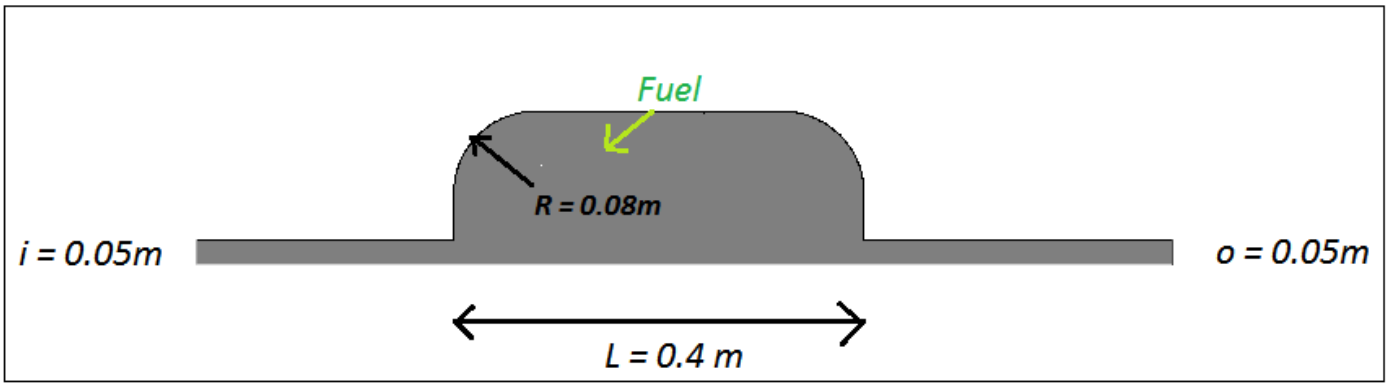
Fuel
R = 0.08m
i = 0.05m
o = 0.05m
L = 0.4 m

f)

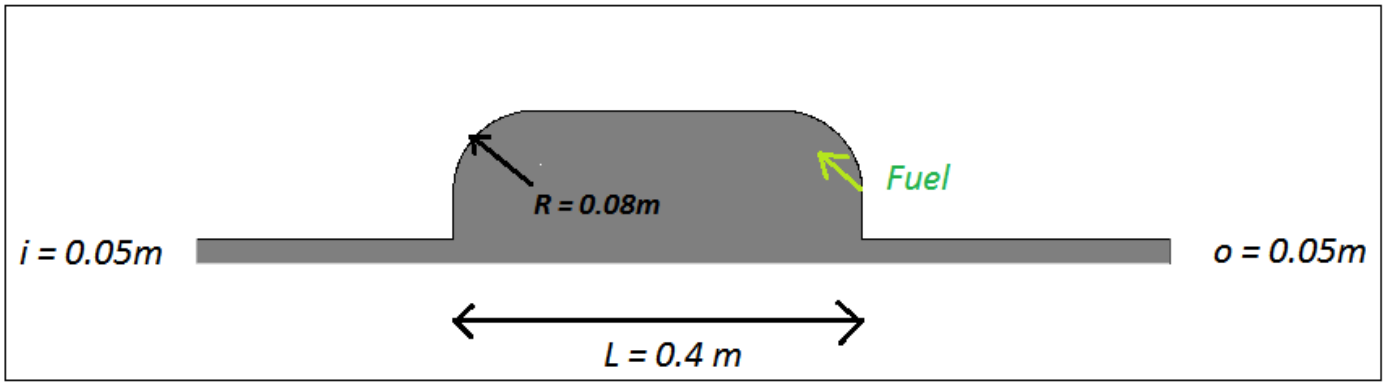
R = 0.08m
Fuel
i = 0.05m
o = 0.05m
L = 0.4 m

g)

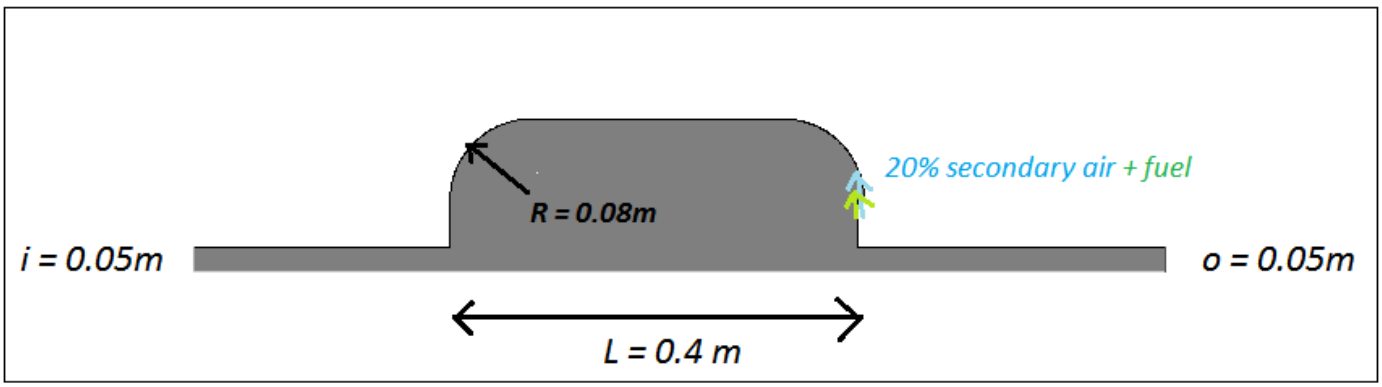
20% secondary air + fuel
R = 0.08m
i = 0.05m
o = 0.05m
L = 0.4 m

h)

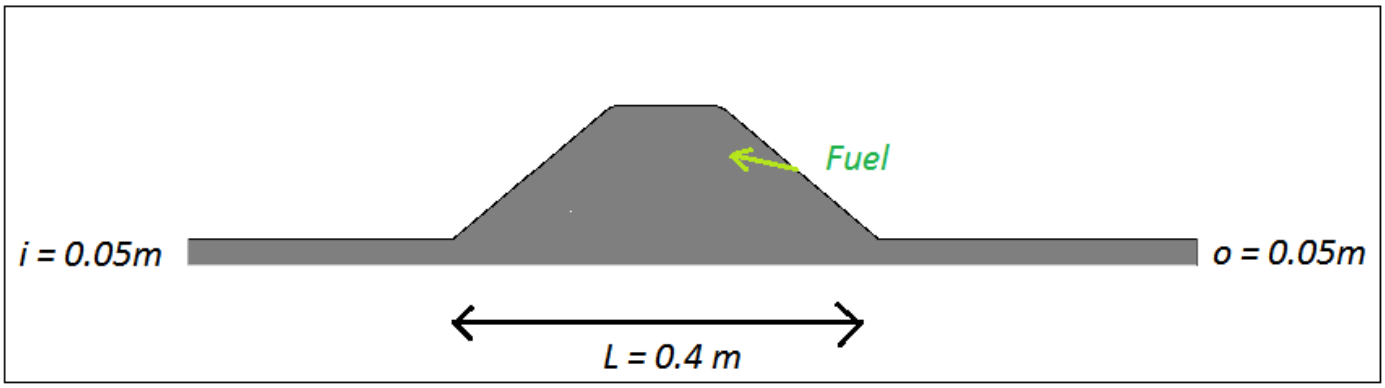
Fuel
i = 0.05m
o = 0.05m
L = 0.4 m

i)

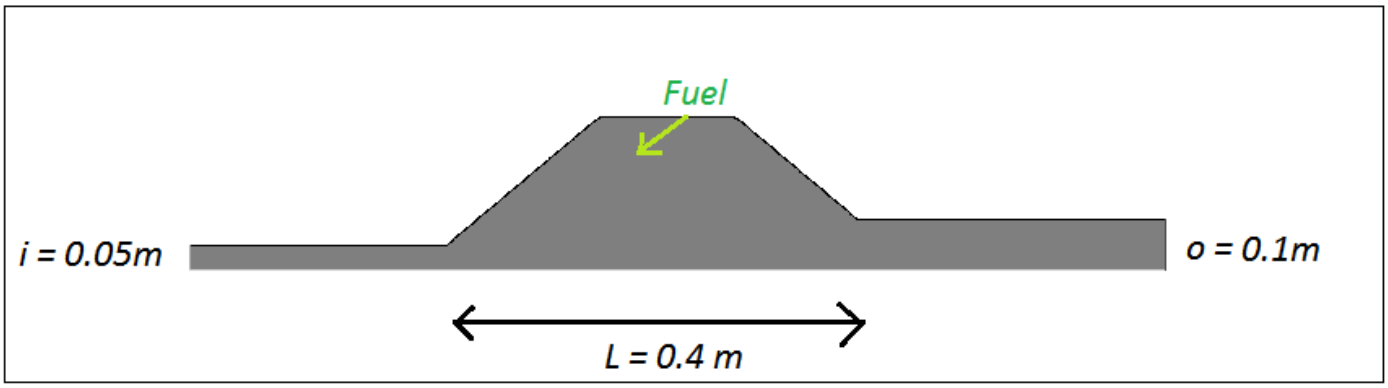
Fuel
i = 0.05m
o = 0.1m
L = 0.4 m

j)

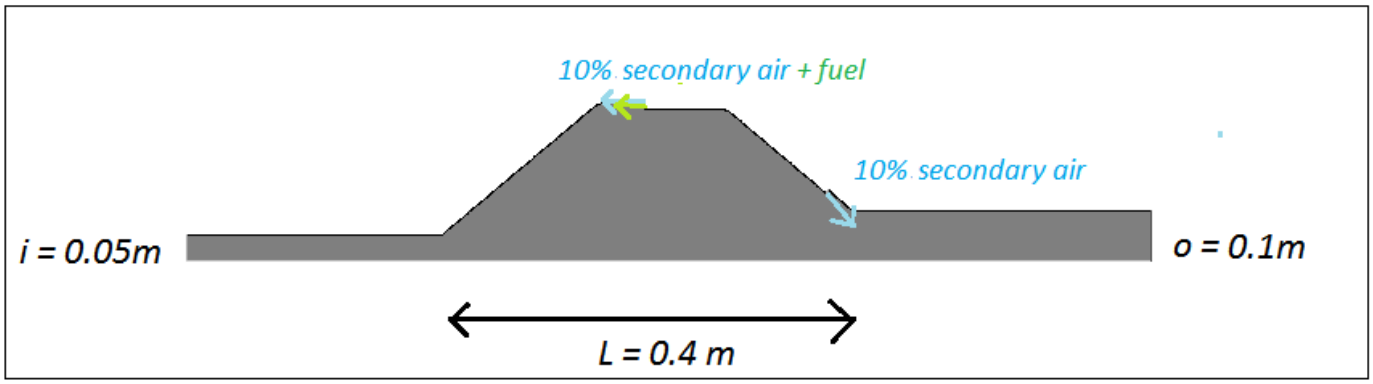
10% secondary air + fuel
10% secondary air
i = 0.05m
o = 0.1m
L = 0.4 m

k)

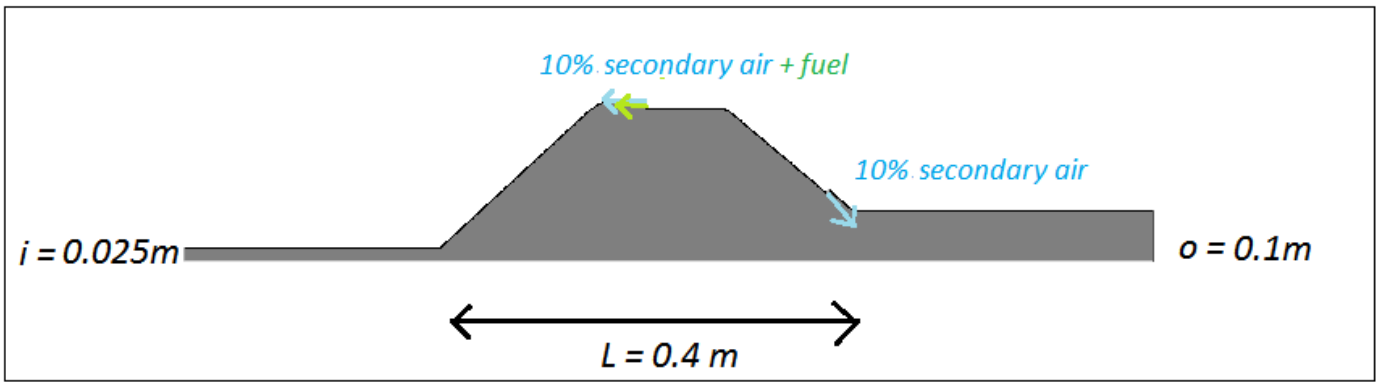
10% secondary air + fuel
10% secondary air
i = 0.025m
o = 0.1m
L = 0.4 m

l)

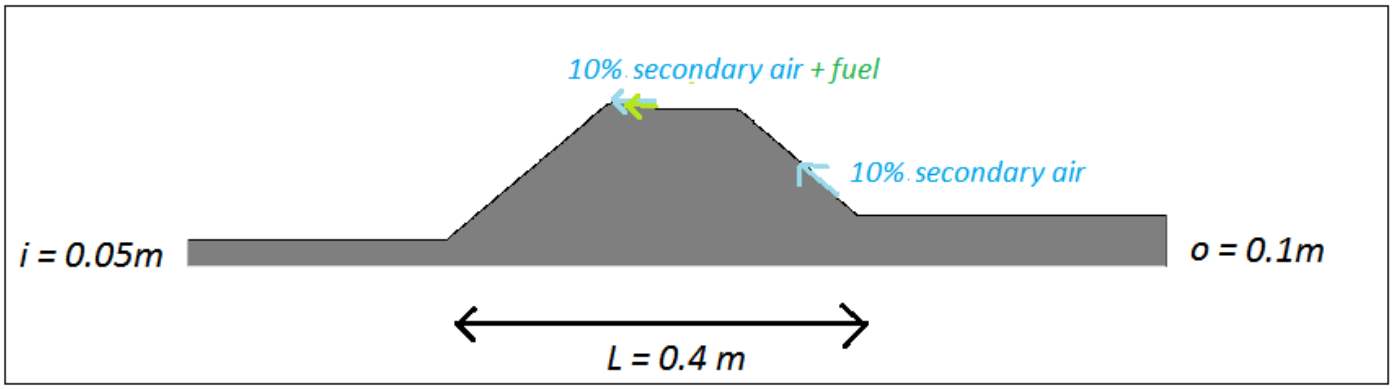
10% secondary air + fuel
10% secondary air
i = 0.05m
o = 0.1m
L = 0.4 m

m)

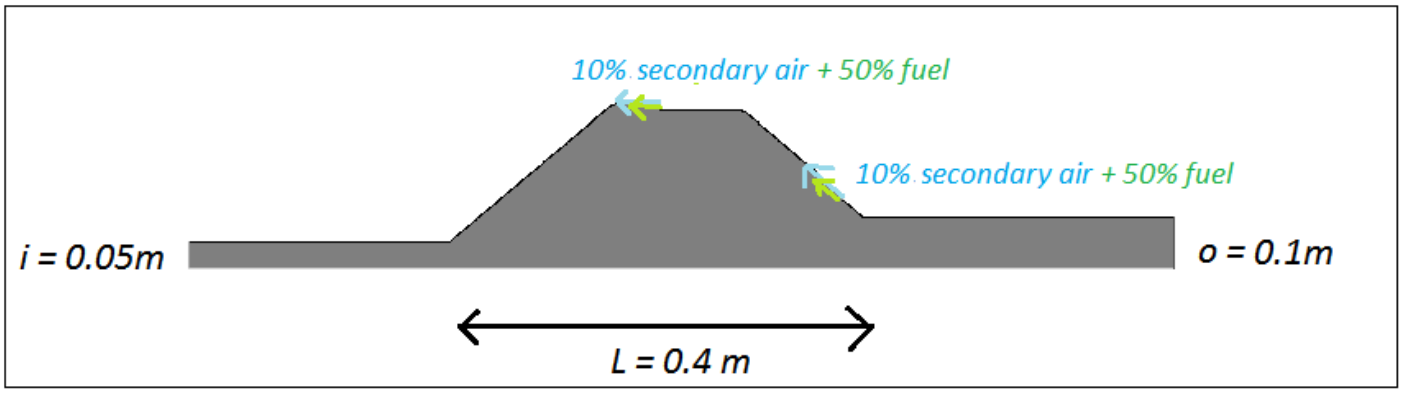
10% secondary air + 50% fuel
10% secondary air + 50% fuel
i = 0.05m
o = 0.1m
L = 0.4 m

n)

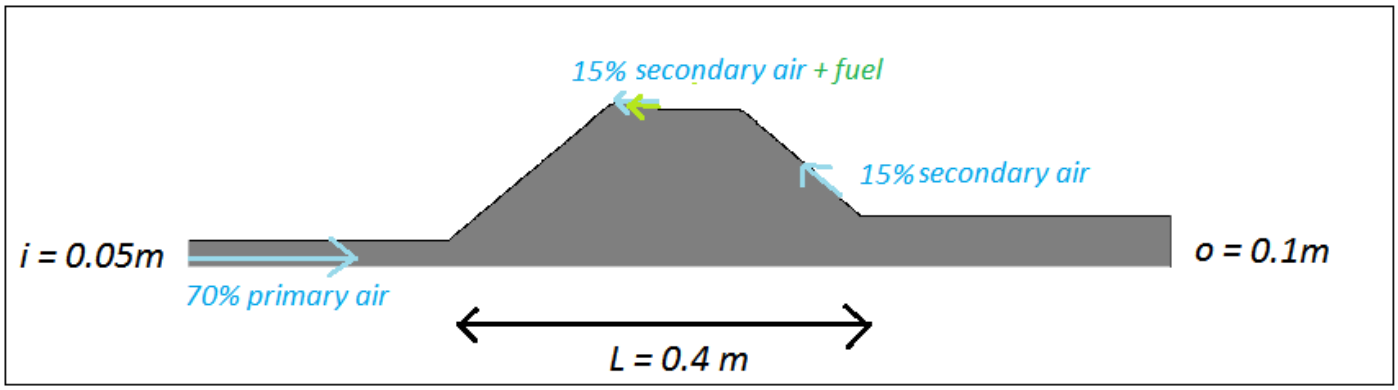
15% secondary air + fuel
15% secondary air
i = 0.05m
o = 0.1m
70% primary air
L = 0.4 m

o)

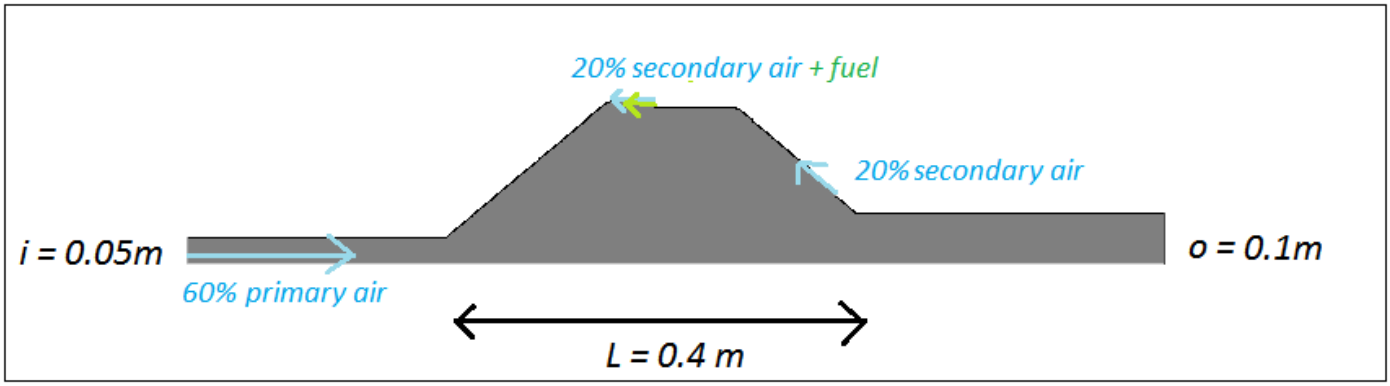
20% secondary air + fuel
20% secondary air
i = 0.05m
o = 0.1m
60% primary air
L = 0.4 m

p)

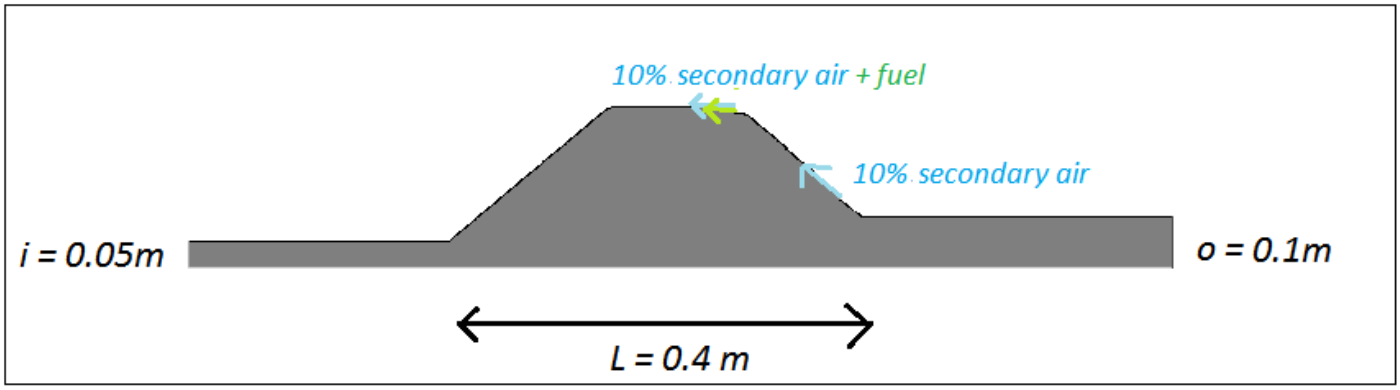
10% secondary air + fuel
10% secondary air
i = 0.05m
o = 0.1m
L = 0.4 m

p2)

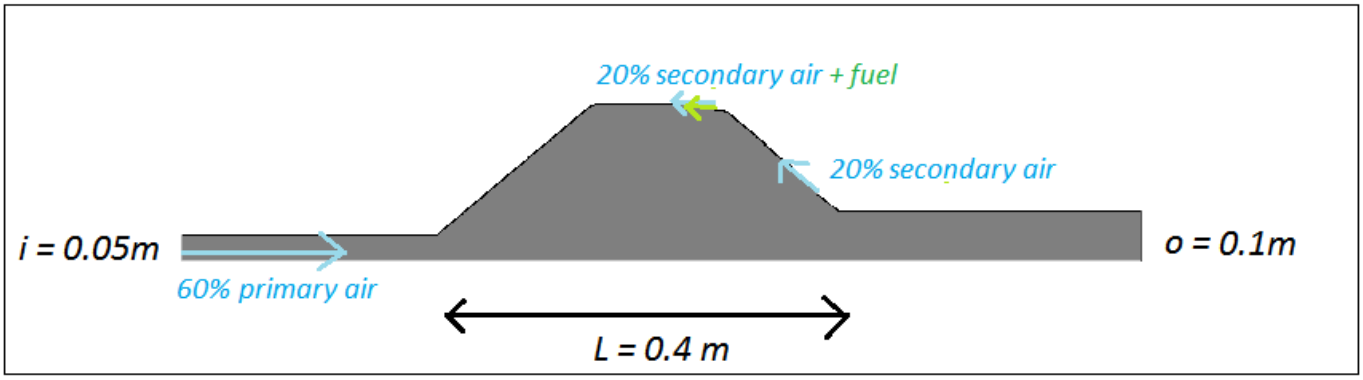
20% secondary air + fuel
20% secondary air
i = 0.05m
o = 0.1m
60% primary air
L = 0.4 m

p3)

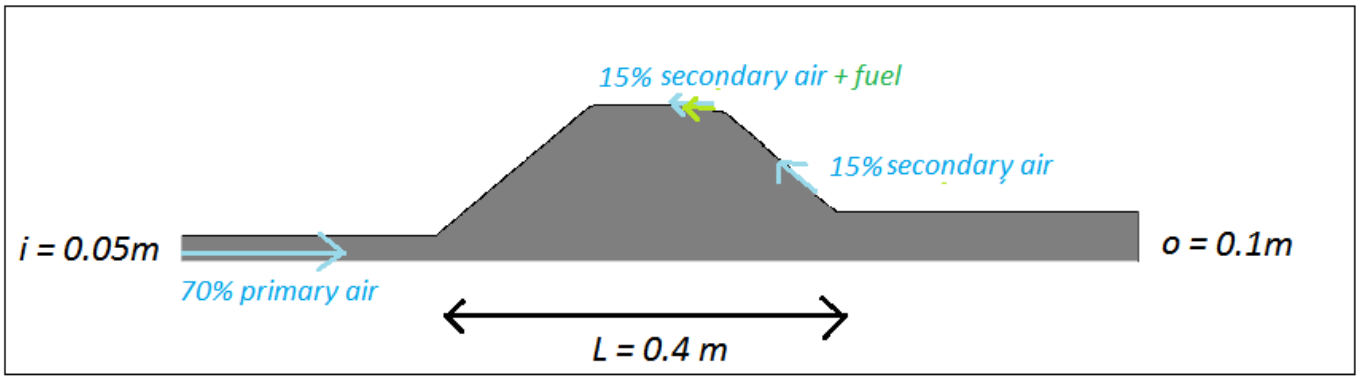
15% secondary air + fuel
15% secondary air
i = 0.05m
o = 0.1m
70% primary air
L = 0.4 m

q)

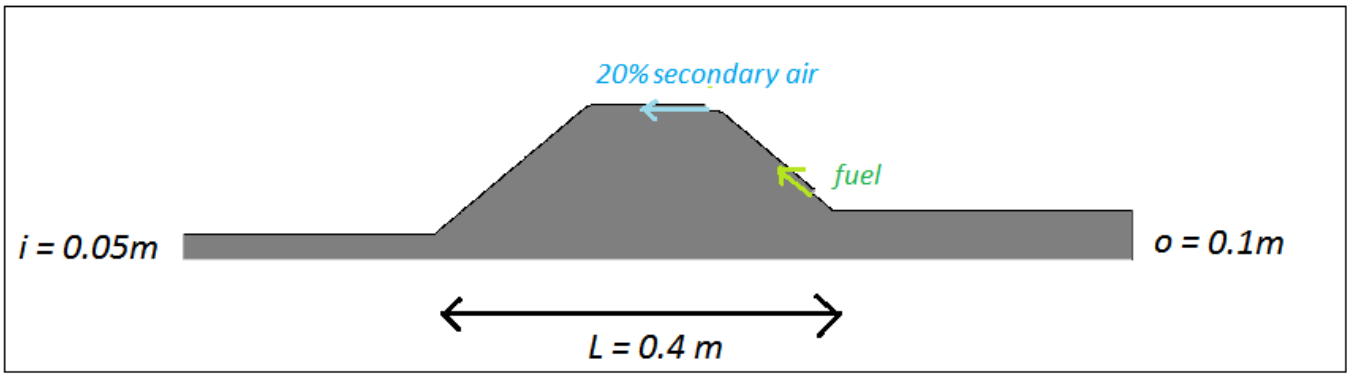
20% secondary air
fuel
i = 0.05m
o = 0.1m
L = 0.4 m

r)

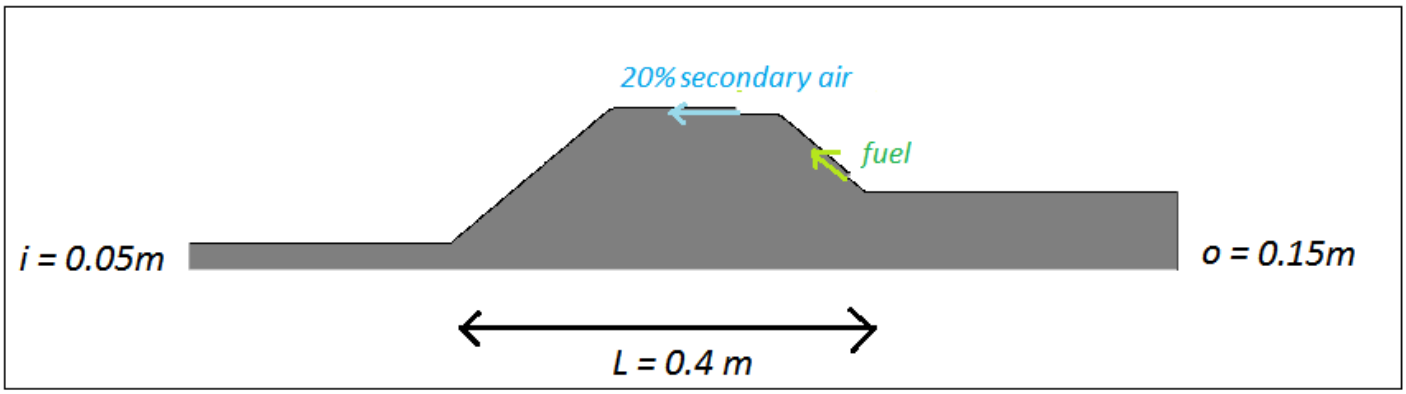
20% secondary air
fuel
i = 0.05m
o = 0.15m
L = 0.4 m

s)

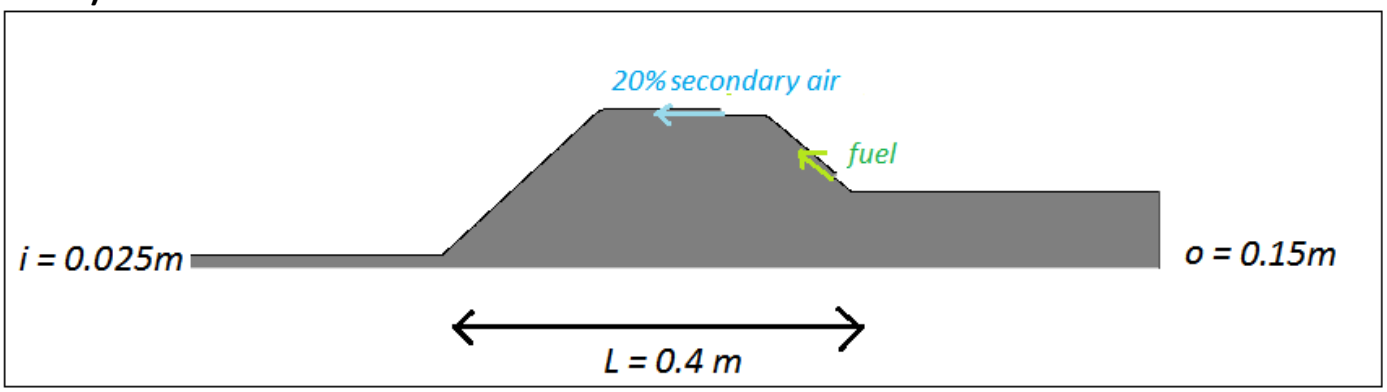
20% secondary air
fuel
i = 0.025m
o = 0.15m
L = 0.4 m

Simulation Data

Case	Type	Ti	air state	φ	mdot air primary	THG**	TIT	CO (ppm)	NOx (ppm)	NOx+NO (N2O)*	Description in key words
13a	Can	1000	vitiated	0.3	0.0736	1697	1557.6	2335	26	37.5	
13b	Can	1000	vitiated	0.3	0.0736	1713	1570.4	1215	287	394	L60
13c	Can	1000	vitiated	0.3	0.0736		1640	2471			Dilution at cavity outlet (1400K)
13d	Can	1000	vitiated	0.3	0.0736		1575	1475	87		Dilution, fuel middle
13d2	Can	1000	vitiated	0.3	0.0736		1590	1515	73		Dilution, fuel near outlet
13e	Can	1000	vitiated	0.3	0.0736	1698	1558.4	3117	31		Fillet R8
13f	Can	1000	vitiated	0.3	0.0736	1684	1547.2	2689			Fillet R8, fuel near outlet
13g	Can	1000	vitiated	0.3	0.0736		1569	1509			Fillet R8, fuel near outlet/ dilution
13h	Can	1000	vitiated	0.3	0.0736	1712	1569.6	2610	25		fuel at backside
13i	Can	1000	vitiated	0.3	0.0736	1705	1564	1257	87		i5o10
13j	Can	1000	vitiated	0.3	0.0736		1581	716	88		i5o10 dilution
13k	Can	1000	vitiated	0.3	0.0736		1616	741	61		i2.5o10 dilution
13l	Can	1000	vitiated	0.3	0.0736		1567	532		52	i5o10 dilution reverse
13m	Can	1000	vitiated	0.3	0.0736		1576	572	108	125	i5o10 fuel staging and dilution
13n	Can	1000	vitiated	0.3	**0.0644**		1588	465		41	i5o10 dilution reverse, Primary-70%
13o	Can	1000	vitiated	0.3	**0.0552**		1588	327		61	i5o10 dilution reverse, P-60%
13p	Can	1000	vitiated	0.3	0.0736		1585	614		23	i5o10 dilution reverse, fuel aft
12p	Can	1000	Fresh Air	0.3	0.0736		1607	503		345	i5o10 dilution reverse, fuel aft
13p2	Can	1000	vitiated	0.3	**0.0552**		1597	253		191	i5o10 dilution reverse, fuel aft P-60%
13p3	Can	1000	vitiated	0.3	**0.0644**		1588	445		151	i5o10 dilution reverse, fuel aft P-70%
13pAT12	Can	1200	vitiated	**0.14**	0.0736		1382	27		2.3	AHEAD, Take-Off
13pAC12	Can	1200	vitiated	**0.1**	0.0736		1333	72		0.7	AHEAD, Cruise
3pAT12	**Planar**	1200	vitiated	0.14	1.1495		1384	491		5	
3qAT12	**Planar**	1200	vitiated	0.14	1.1495		1353	287		12	i2.5o10 dilution reverse, fuel near outlet
3rAT12	**Planar**	1200	vitiated	0.14	1.1495		1385	207		65	i5o15 dilution reverse, fuel near outlet
3sAT12	**Planar**	1200	vitiated	0.14	1.1495		1352	298		9.7	i2.5o15 dilution reverse, fuel near outlet
3sAT12	**Planar**	1200	Fresh Air	0.14	1.1495		1363	335		33	

*NO (N2O) implies that the NO formation path via the intermediate N_2O was included.

**THG (Hot Gas Temperature) is the calculated liner outlet temperature when no secondary air was injected.
For these cases, the TIT was estimated.